

# Arbeitsbericht NAB 13-94

**Hydraulic conductance of the EDZ  
around underground structures of a  
geological repository for radioactive  
waste – A sensitivity study for the  
candidate host rocks in the proposed  
siting regions in Northern Switzerland**

March 2014

A. Alcolea, U. Kuhlmann (TK Consult AG),  
G.W. Lanyon (Fracture Systems Ltd.),  
P. Marschall (Nagra)

Nationale Genossenschaft  
für die Lagerung  
radioaktiver Abfälle

Hardstrasse 73  
CH-5430 Wettingen  
Telefon 056-437 11 11

[www.nagra.ch](http://www.nagra.ch)



# Arbeitsbericht NAB 13-94

**Hydraulic conductance of the EDZ  
around underground structures of a  
geological repository for radioactive  
waste – A sensitivity study for the  
candidate host rocks in the proposed  
siting regions in Northern Switzerland**

March 2014

A. Alcolea, U. Kuhlmann (TK Consult AG),  
G.W. Lanyon (Fracture Systems Ltd.),  
P. Marschall (Nagra)

**KEYWORDS**

Opalinus Clay, SF/HLW, L/ILW, shaft, seal section,  
numerical simulation; EDZ; fracture network, hydraulic  
conductivity, self-sealing

**Nationale Genossenschaft  
für die Lagerung  
radioaktiver Abfälle**

Hardstrasse 73  
CH-5430 Wettingen  
Telefon 056-437 11 11

[www.nagra.ch](http://www.nagra.ch)

Nagra Working Reports concern work in progress that may have had limited review. They are intended to provide rapid dissemination of information.

"Copyright © 2014 by Nagra, Wettingen (Switzerland) / All rights reserved.

All parts of this work are protected by copyright. Any utilisation outwith the remit of the copyright law is unlawful and liable to prosecution. This applies in particular to translations, storage and processing in electronic systems and programs, microfilms, reproductions, etc."

## Zusammenfassung

Beim Bau und Betrieb eines geologischen Tiefenlagers entwickelt sich im Umfeld der Untertagebauwerke eine Auflockerungszone, die nach Lagerverschluss einen möglichen Freisetzungspfad für Radionuklide darstellt und somit im Rahmen der Langzeit-Sicherheitsanalysen zu berücksichtigen ist. Die Wirksamkeit dieses Freisetzungspfads hängt von der Form und der räumlichen Erstreckung der Auflockerungszone ab und von der Art der Gebirgsauflockerung. In überkonsolidierten Tonformationen zeigen sowohl empirische Befunde als auch experimentelle Untersuchungen ausnahmslos, dass die Auflockerungszone aus diskreten, exkavationsbedingten Trennflächensystemen besteht.

Im Rahmen einer rissmechanischen Modellierstudie wurden für ein geologisches Tiefenlager im Opalinuston Sensitivitätsanalysen zur Entstehung und Entwicklung der Auflockerungszone im Umfeld der Untertagebauwerke durchgeführt (Geomechanica 2013). In der Studie wurde der Einfluss der Lagertiefe, der Gebirgsspannung, der Gesteinsfestigkeit und des Tunnelausbaus auf die Form und Ausdehnung der Auflockerungszone untersucht. Die berechneten Rissbilder liefern die Grundlage für die quantitative Abschätzung der hydraulischen Bedeutung der Auflockerungszone. Im vorliegenden Bericht wurde ein Modellansatz entwickelt und erprobt, mit dem anhand der simulierten Rissbilder die Entwicklung der hydraulischen Eigenschaften der Auflockerungszone nach Lagerverschluss modelliert werden kann. Neben der realitätsnahen Darstellung der Rissmuster werden mit dem Modellansatz auch die vielfältigen hydro-mechanischen Phänomene und Prozesse nachgebildet, die im Zusammenhang mit der Entstehung und Entwicklung der Auflockerungszone beobachtet werden. Insbesondere wurden die Selbstabdichtung der exkavationsbedingten Trennflächen und das Quellverhalten des intakten Gebirges durch vereinfachte rissmechanische bzw. geomechanische Prozessmodelle implementiert. Der entwickelte Modellansatz wurde anhand von empirischen Befunden und experimentellen Untersuchungen aus dem Felslabor Mont Terri überprüft, wobei sich im Rahmen der verfügbaren Datenbasis eine gute Übereinstimmung zwischen den Ergebnissen der Modellierungen und den in situ Beobachtungen ergab.

Die von Geomechanica (2013) gelieferten Rissbilder zur Auflockerungszone im Umfeld eines geologische Tiefenlagers im Opalinuston wurden mit dem entwickelten Modellansatz analysiert und die hydraulische Bedeutung der Auflockerungszone wurde quantitativ abgeschätzt. Die Ergebnisse lassen sich wie folgt zusammenfassen:

- Durch die Aufsättigung der verfüllten Untertagebauwerke dichten sich die exkavationsbedingten Trennflächensysteme im Gebirge weitgehend ab, so dass die hydraulische Wirksamkeit der Auflockerungszone drastisch sinkt. Im Opalinuston ist der hydraulisch wirksame (äussere) Radius der Auflockerungszone nach erfolgter Aufsättigung kleiner als 2 Tunneldurchmesser.
- Eine signifikante Erhöhung der hydraulischen Durchlässigkeit gegenüber dem intakten Wirtgestein ist nur in einer Zone von ca. einem halben Tunneldurchmesser zu erwarten. In dieser Zone kann die hydraulische Durchlässigkeit gegenüber dem intakten Wirtgestein um bis zu einer Grössenordnung erhöht sein, während die Porosität maximal um 20% erhöht wird.



## Table of Contents

Zusammenfassung.....	I
Table of Contents .....	III
List of Tables.....	V
List of Figures .....	VI
<b>1 Introduction .....</b>	<b>1</b>
1.1 Background and motivation.....	1
1.2 Scope and objectives.....	1
1.3 Report organization .....	2
<b>2 Fundamentals .....</b>	<b>3</b>
2.1 Porewater flow in the EDZ – state of knowledge.....	3
2.2 Conceptualisation of porewater flow in Opalinus Clay.....	8
2.2.1 Geological setting and basic rock characteristics .....	8
2.2.2 Permeability of the intact rock matrix .....	10
2.2.3 Transmissivity of tectonic fractures.....	14
2.2.4 Self-sealing of fractures.....	16
2.2.5 A conceptual framework for EDZ fracture closure in Opalinus Clay .....	20
2.3 Previous EDZ Abstractions for Safety Assessment.....	21
<b>3 EDZ model abstraction for Safety Assessment - Methodology .....</b>	<b>25</b>
3.1 Expectations and model requirements .....	25
3.2 Model implementation – General workflow.....	26
3.3 Discrete fracture network representation of the EDZ.....	28
3.3.1 Basic input .....	28
3.3.2 Pre-processing of data.....	29
3.4 Equivalent continuum model of the EDZ.....	33
3.4.1 Mesh generation .....	33
3.4.2 Upscaling procedure: Equivalent continuum parameters .....	35
3.4.3 Initial equivalent continuum parameters.....	36
3.4.4 Resaturation of the system: Temporal evolution of equivalent continuum parameters.....	38
3.4.5 Abstraction of the EDZ.....	44
<b>4 Hydraulic properties of the EDZ – A sensitivity analysis .....</b>	<b>49</b>
4.1 Overview of considered FEMDEM simulations .....	49
4.2 The SF/HLW near-field (HAA models) .....	51
4.2.1 Model simulations and overall observations .....	53
4.2.2 Sensitivity analysis .....	58
4.3 The EDZ around seal sections and shafts .....	64

4.3.1	Model simulations and overall observations .....	65
4.3.2	Sensitivity analysis .....	73
4.4	EDZ under re-compaction conditions.....	77
4.4.1	HAA-Rec models.....	77
4.4.2	Shaft_Rec models .....	82
4.5	Transient behavior under resaturation conditions.....	88
4.6	Evaluation of the results of the sensitivity analyses .....	90
4.6.1	HAA-models (SF/HLW emplacement tunnel) .....	91
4.6.2	Shaft models .....	94
4.7	Envisaged extensions of the approach.....	96
<b>5</b>	<b>Summary and conclusions .....</b>	<b>97</b>
<b>6</b>	<b>References.....</b>	<b>99</b>
<b>Appendices:</b>		
<b>A</b>	<b>Description of output files in the digital appendix.....</b>	<b>A-1</b>
<b>B</b>	<b>Two-phase scoping calculations on de- and resaturation of EDZ and buffer.....</b>	<b>B-1</b>

## List of Tables

Tab. 2-1:	Reference values for the gas-related parameters of the undisturbed Opalinus Clay for a shallow/deep repository in Northern Switzerland (RV – reference value; AV – alternative value).....	14
Tab. 3-1:	Basic description of the HAA-01 FEMDEM, used to show the workflow. ....	28
Tab. 3-2:	Zones of the model and deterministic values for hydraulic properties used in this study.....	34
Tab. 4-1:	Summary of HAA model simulations (from Geomechanica 2013). ....	52
Tab. 4-2:	Geometric and hydraulic properties defining the input HAA FEMDEM simulations. Columns 3 to 7 are average values. Thick horizontal lines split the sub-groups in Table 4-1. Results under re-compaction conditions are presented separately in Chapter 4.6. ....	53
Tab. 4-3:	Summary of Shaft model simulations (from Geomechanica 2013). Note that models Shaft-01 and Shaft-02 do not contain fractures and are not considered in this analysis. ....	65
Tab. 4-4:	Geometric and hydraulic properties defining the input Shaft FEMDEM simulations. Columns 3 to 7 are average values. Horizontal lines split the sub-groups in Table 4-3. Results under re-compaction conditions are presented separately in Chapter 4.6. ....	66
Tab. 4-5:	Geometric and hydraulic properties defining the input HAA FEMDEM simulations. Columns 3 to 7 are average values. FEMDEM parameters are reported in Table 4-1. ....	77
Tab. 4-6:	Geometric and hydraulic properties defining the input HAA FEMDEM simulations. Columns 3 to 7 are average values. FEMDEM parameters are reported in Table 4-3. ....	83

## List of Figures

Fig. 2-1:	Excavation induced damage zones in Opalinus Clay: (a) Spalling process leading to an EDZ in the Mont Terri URL (Nagra 2002); (b) bedding related failure in the EDZ of a small borehole (Blümling et al. 2007); (c) interaction of stress controlled EDZ fractures with tectonic structures (Marschall et al. 2006).....	4
Fig. 2-2:	Induced fracturing in the east walls in the EZ-B Niche entrance (Yong 2007).....	5
Fig. 2-3:	Coalescence of extension and shear fractures to form a network of composite fracture planes observed in the sidewall of the Reconnaissance Gallery at Mont Terri (modified from Thury and Bossart 1999; see also Appendix 4 in Bock et al. 2010).....	5
Fig. 2-4:	Fracture counts in 0.5 m borehole intervals from around the EZ-B Niche and previous sub-parallel excavations (from Yong 2007).....	6
Fig. 2-5:	In situ permeability measurements conducted in Mont Terri experimental drift (from Bossart and Thury 2008).....	7
Fig. 2-6:	Depth dependency of porosity measured in Opalinus Clay core samples recovered from different depths (after Senger et al. 2013).....	9
Fig. 2-7:	Volumetric deformation behaviour of Opalinus Clay: normal consolidation and rebound/ reconsolidation in response to changes of mean effective stress (from Nagra 2004).....	10
Fig. 2-8:	Depth dependency of porosity (left) and hydraulic conductivity (right) derived from tests on Opalinus Clay core samples under different effective stresses (from Senger et al. 2013). Light colors denote core samples with clay content below 40% (or carbonates content above 25% when clay content was not available). .....	11
Fig. 2-9:	Correlation between hydraulic conductivity and porosity measured under different effective stresses in Opalinus Clay core samples, from Ferrari et al. (2013) and Romero & Gomez (2013).....	12
Fig. 2-10:	Comparison of the hydraulic conductivity indicators after Kozeny-Carman (K-C) and Yang&Aplin (Y&A) with the available measurements in Opalinus Clay core samples: (a) clay content versus hydraulic conductivity and (b) porosity versus hydraulic conductivity (assumed clay content: 40 and 80%, respectively).....	13
Fig. 2-11:	Dependency between fracture aperture and normal effective stress after Bandis et al. (1983). The fracture will close when the effective stress increases.....	15
Fig. 2-12:	Self-sealing of fractures in Opalinus Clay as part of the GS-experiment at Mont Terri (from Nagra 2004): (a) experimental set-up and (b) dependency between interval transmissivity and normal effective stress ( $\sigma_n - p_i$ ). Hydraulic tests were conducted using different interval pressures $p_i$ . Normal stress $\sigma_n$ was derived from the shut-in pressure during hydrofracturing (~ 4.3 MPa). .....	16

Fig. 2-13:	Long-term changes in EDZ transmissivity in an open tunnel section at the Mont Terri Rock Laboratory (after Nagra 2004): (a) sketch of the experimental set-up and (b) long-term monitoring of EDZ transmissivity. Initially, the EDZ was saturated for a period of 800 days (blue dots) and EDZ transmissivity was monitored periodically. Afterwards, a load plate was installed (1 - 5 MPa) and the transmissivity measurements were repeated. ....	18
Fig. 2-14:	Sample core from EZ-A boreholes: a) core showing wet zone along fracture; b) self-sealing feature showing fluorescein dye from previous injection tests. ....	18
Fig. 2-15:	The HG-A experiment in the Mont Terri URL (Marschall et al. 2013): experimental layout (top) and microtunnel instrumentation (bottom). ....	19
Fig. 2-16:	Sealing index for HG-A experiment showing reduction in ability to inject water into the Test Section due to reduction in EDZ conductance. At the end of the observation period, the effective hydraulic conductivity of an equivalent radial EDZ with a cross-sectional area of 1 m <sup>2</sup> is around 2E-12 m/s. ....	20
Fig. 2-17:	A conceptual framework for EDZ fracture closure in Opalinus Clay, covering the key phenomena and features from the early post excavation phase until static formation pressure recovery. ....	21
Fig. 2-18:	Nagra's EDZ conceptualisation (Lanyon 2011): The reference case is shown, although the assessment included "what-if" scenarios with higher EDZ hydraulic conductivity or the absence of EDZ (for gas studies). ....	21
Fig. 2-19:	Components of the EDZ converter: input (definition of parameters / experts), hardwired EDZ abstraction procedure and output for end users (from Lanyon & Senger 2011). ....	22
Fig. 2-20:	DFN (upper) and EPM (lower) models of the EDZ along a 400 m tunnel in Opalinus Clay (from Lanyon & Senger 2011). ....	23
Fig. 2-21:	Simulated response to gas injection: left: pressure; right: gas flow for equivalent heterogeneous CPM model and simplified single-shell effective property model. ....	23
Fig. 2-22:	EDZ model for tunnel in COX from Hawkins et al. (2011): a) distribution of axial permeability in heterogeneous CPM model; b) gas flow for equivalent heterogeneous CPM model and simplified single-shell effective property model. ....	24
Fig. 3-1:	Concept of the EDZ abstraction process for a circular tunnel (diameter 2.8 m): representative fracture patterns are simulated for relevant repository configurations with a discrete element model. The discrete fracture patterns are converted in heterogeneous porosity and conductivity distributions. In a final abstraction process, the heterogeneous porosity / conductivity distributions are converted in a shell defined by a radius $r_{EDZ}=r_{tunnel}+d_{EDZ}$ and homogeneous porosity / conductivity. ....	26
Fig. 3-2:	Basic features and steps of the modeling strategy: (a) FEMDEM as input data set; (b) radial grid over which geometric properties of the FEMDEM are mapped, (c) debugging statistics of the FEMDEM, (d) mapping of hydraulic properties (total porosity in this case), (e) transient simulation of the resaturation of the system (in the figure, temporal evolution of number of closed fractures), (f) early and late time abstractions of the EDZ. ....	27

Fig. 3-3:	Fracture failure modes.....	29
Fig. 3-4:	Basic notation for the 4-nodes polygon defining a fracture. On the right, extreme case of fractures with zero aperture.....	29
Fig. 3-5:	Histograms of fracture parameters.....	30
Fig. 3-6:	Geometric definition of the input FEMDEM.....	31
Fig. 3-7:	Hydraulic definition of the input FEMDEM. Panels (a) and (b) report on initial and irreducible fracture apertures (early and late times, respectively). Panels (c) and (d) report on initial and irreducible fracture transmissivities. Panel (e) displays the number of fractures at trace lines at inclinations 0, 45 and 90° (counterclockwise from x axis). Dashed black lines depict the extension of the buffer zone.....	32
Fig. 3-8:	Three zoom levels of the finite element mesh adopted in this work. From left to right: (a) overall mesh, with radius 100 m; (b) zoom at the zone of interest encompassing the EDZ; (c) zoom at the closest vicinity of the canister. The red lines encompass the input DFN (radius ~ 6-8 m in this case) and the liner. The inner circle represents the canister, with radius 0.5 m, assumed to be impervious.....	34
Fig. 3-9:	Model zonation. From left to right: (a) Global domain. The intact OPA (light blue) predominates; (b) zoom at the scale of the EDZ (radius ~ 6-8 m). In this area, a vast majority of cells are intersected by fractures (in yellow); (c) zoom at the scale of the gallery. Although some fractures intersect the wall-rock cells (blue color), these are not taken into account in the calculations because the wall-rock contact is attributed with deterministic properties (Table 3-2) regardless of the fracturation intensity. Fracture traces are highlighted in white. The central grey circle is a hole depicting the canister (r = 0.5 m), assumed impervious.....	35
Fig. 3-10:	Mapped distributions of: (a) initial fracture porosity, (b) initial matrix porosity and (c) total initial porosity. Fracture traces are depicted by shaded black lines in panel (b).....	37
Fig. 3-11:	Mapped distributions of: (a) initial fracture hydraulic conductivity, (b) initial matrix hydraulic conductivity and (c) cell conductivity in the axial direction. Fracture traces are depicted by red lines in panel (b). Dark grey color in panel (a) depicts elements not intersected by fractures. log <sub>10</sub> distributions are plotted for clarity.....	37
Fig. 3-12:	Fracture aperture vs. overpressure (with respect to atmospheric) for different values of the exponent $\alpha$ defining the modified Barton-Bandis' model in Equation 3-11.....	39
Fig. 3-13:	A few snapshots of the temporal evolution of pressure.....	41
Fig. 3-14:	Mean pressure as a function of time for different values of the $\alpha$ -values defining the rate of fracture closure.....	42
Fig. 3-15:	Temporal evolution of axial (total) hydraulic conductivity. For clarity, log <sub>10</sub> distributions are displayed.....	43
Fig. 3-16:	Number of closed fractures as a function of time.....	43

Fig. 3-17:	Spatial distribution of specific axial fluxes. Left panel: fluxes across fractures only (i.e., the axial conductivity of the matrix is removed in the calculations). Right panel: total fluxes, including matrix hydraulic conductivity. The pink insets depict the buffer zone. The gap at radial distance between 7.5 and 8 m, corresponds to a disconnected fracture zone as shown in Fig. 3-11. ....	45
Fig. 3-18:	Spatial distribution of integrated fracture matrix and total porosity at early (left panel) and late times. Note that total porosity is assumed to be constant in time. The pink insets depict the buffer zone. ....	46
Fig. 3-19:	Fracture density (number of fractures per unit ring area) vs. radial distance. The extension of the EDZ is approximately 6 m. ....	47
Fig. 3-20:	Abstracted EDZ model, based on simulation case HAA-01. Radial distribution of equivalent hydraulic conductivity and porosity of the HAA-near-field components (cansiter, bentonite buffer, liner, EDZ, host rock). $K$ and $K_r$ denote hydraulic conductivity at early and late times, respectively. ....	47
Fig. 3-21:	Temporal evolution of equivalent hydraulic conductivity of the EDZ (left) and of axial flow rate across the abstracted EDZ (right). ....	48
Fig. 3-22:	Spatial distribution of axial fluxes at selected stages of resaturation. Note that the two end-member calculations at $t = 0$ and $t = 27'160$ years are reported also in Figure 3-17. ....	48
Fig. 4-1:	Undeformed geometry of the HAA (left) and Shaft models (right) used in this study. Modified from Geomechanica (2013). ....	50
Fig. 4-2:	Spatial distribution of equivalent fracture density (number of fractures on a ring of elements standardized by the ring area) of HAA models. The pink inset depicts the buffer zone. ....	54
Fig. 4-3:	Spatial distribution of total equivalent specific axial fluxes of HAA models. The pink inset depicts the buffer zone. On the left, early time behavior, after excavation and emplacement. On the right, late time behavior, after full resaturation of the system (i.e., assuming that all fractures are closed). ....	55
Fig. 4-4:	Spatial distribution of fracture porosity of HAA models. The pink inset depicts the buffer zone. On the left, early time behavior, after excavation and emplacement. On the right, late time behavior, after full resaturation of the system (i.e., when all fractures are closed). ....	56
Fig. 4-5:	Spatial distribution of matrix porosity of HAA models. The pink inset depicts the buffer zone. On the left, early time behavior, after excavation and emplacement. On the right, late time behavior, after full resaturation of the system (i.e., assuming that all fractures are closed). Note that matrix porosity represents total porosity at late times. ....	57
Fig. 4-6:	Equivalent radius of the EDZ abstraction of HAA models, defined as the radial distance at which fracture density drops to 10 fractures/m <sup>2</sup> . Textboxes and vertical dashed lines depict the different groups of simulations in Table 4-2. ....	57
Fig. 4-7:	Early and late time total equivalent specific fluxes of the abstracted HAA models. ....	58
Fig. 4-8:	Total equivalent porosity of the abstracted HAA models. ....	58

Fig. 4-9:	Fracture density depending on in situ stress conditions and core softening ratio. HAA models.....	60
Fig. 4-10:	Total axial fluxes at early (left) and late times (right) depending on in situ stress conditions and core softening ratio. HAA models.....	61
Fig. 4-11:	Fracture density depending on strength parameters and elastic modulus of support. HAA models.....	61
Fig. 4-12:	Total axial fluxes at early (left) and late times (right) depending on strength parameters and elastic modulus of support. HAA models.....	62
Fig. 4-13:	Fracture density in the presence/absence of pre-existent faults. HAA models.....	63
Fig. 4-14:	Total axial fluxes at early (left) and late times (right) in the presence/absence of pre-existent faults. HAA models.....	64
Fig. 4-15:	Spatial distribution of equivalent fracture density (number of fractures on a ring of elements standardized by the ring area) of Shaft models. The pink inset depicts the buffer zone.....	67
Fig. 4-16:	Spatial distribution of total equivalent specific axial fluxes of Shaft models. The pink inset depicts the buffer zone. On the left, early time behavior, after excavation and emplacement. On the right, late time behavior, after full resaturation of the system (i.e., when all fractures are closed).....	68
Fig. 4-17:	Spatial distribution of fracture porosity of Shaft models. The pink inset depicts the buffer zone. On the left, early time behavior, after excavation and emplacement. On the right, late time behavior, after full resaturation of the system (i.e., assuming that all fractures are closed).....	69
Fig. 4-18:	Spatial distribution of matrix porosity of HAA models. The pink inset depicts the buffer zone. On the left, early time behavior, after excavation and emplacement. On the right, late time behavior, after full resaturation of the system (i.e., assuming that all fractures are closed). Note that matrix porosity represents total porosity at late times.....	70
Fig. 4-19:	Equivalent radius of the EDZ abstraction of Shaft models, defined as the radial distance at which fracture density drops to 100 fractures/m <sup>2</sup> . Textboxes and vertical dashed lines depict the different groups of simulations in Table 4.3. Simulations of EDZ under re-compaction conditions are presented separately in Chapter 4.6.....	71
Fig. 4-20:	Equivalent radius of the abstracted EDZ of shaft models vs. number of fractures defining the FEMDEM. In the inset, best fitting trend line and correlation coefficient.....	71
Fig. 4-21:	Early and late time total equivalent specific fluxes of the abstracted Shaft models.....	72
Fig. 4-22:	Equivalent total porosity of the abstracted EDZ for Shaft models.....	73
Fig. 4-23:	Fracture density depending on in situ stress conditions. Shaft models.....	74
Fig. 4-24:	Total axial fluxes at early (left) and late times (right) depending on in situ stress conditions. Shaft models.....	75
Fig. 4-25:	Fracture density depending on strength parameters. Shaft models.....	76
Fig. 4-26:	Total axial fluxes at early (left) and late times (right) depending on strength parameters. Shaft models.....	76

Fig. 4-27: Spatial distribution of equivalent fracture density (number of fractures on a ring of elements standardized by the ring area) of HAA-Rec models. The inset depicts the buffer zone. .... 78

Fig. 4-28: Spatial distribution of total equivalent specific axial fluxes of HAA-Rec models. The pink inset depicts the buffer zone. On the left, early time behavior, after excavation and emplacement. On the right, late time behavior, after full resaturation of the system (i.e., assuming that all fractures are closed). .... 79

Fig. 4-29: Spatial distribution of fracture porosity of HAA-Rec models. The inset depicts the buffer zone. On the left, early time behavior, after excavation and emplacement. On the right, late time behavior, after full resaturation of the system (i.e., when all fractures are closed). .... 80

Fig. 4-30: Spatial distribution of matrix porosity of HAA-Rec models. The inset depicts the buffer zone. On the left, early time behavior, after excavation and emplacement. On the right, late time behavior, after full resaturation of the system (i.e., assuming that all fractures are closed). Note that matrix porosity represents total porosity at late times. .... 81

Fig. 4-31: Equivalent radius of the EDZ abstraction of HAA-Rec models, defined as the radial distance at which fracture density drops to 10 fractures/m<sup>2</sup>. .... 81

Fig. 4-32: Early and late time total equivalent specific fluxes of the abstracted HAA-Rec models. .... 82

Fig. 4-33: Total equivalent porosity of the abstracted HAA-Rec models. .... 82

Fig. 4-34: Spatial distribution of equivalent fracture density (number of fractures on a ring of elements standardized by the ring area) of Shaft-Rec models. The inset depicts the buffer zone. .... 84

Fig. 4-35: Spatial distribution of total equivalent specific axial fluxes of Shaft-Rec models. The pink inset depicts the buffer zone. On the left, early time behavior, after excavation and emplacement. On the right, late time behavior, after full resaturation of the system (i.e., assuming that all fractures are closed). .... 85

Fig. 4-36: Spatial distribution of fracture porosity of Shaft-Rec models. The inset depicts the buffer zone. On the left, early time behavior, after excavation and emplacement. On the right, late time behavior, after full resaturation of the system (i.e., when all fractures are closed). .... 86

Fig. 4-37: Spatial distribution of matrix porosity of Shaft-Rec models. The inset depicts the buffer zone. On the left, early time behavior, after excavation and emplacement. On the right, late time behavior, after full resaturation of the system (i.e., assuming that all fractures are closed). Note that matrix porosity represents total porosity at late times. .... 87

Fig. 4-38: Equivalent radius of the EDZ abstraction of Shaft-Rec models, defined as the radial distance at which fracture density drops to 10 fractures/m<sup>2</sup>. .... 87

Fig. 4-39: Early and late time total equivalent specific fluxes of the abstracted Shaft-Rec models. .... 88

Fig. 4-40: Total equivalent porosity of the abstracted Shaft-Rec models. .... 88

Fig. 4-41: Number of closed fractures vs. resaturation time. HAA-01 to 03 models. .... 89

Fig. 4-42:	Spatial distribution of equivalent specific axial fluxes at selected times. HAA-01 to 03 models.....	90
Fig. 4-43:	Radial profiles of (a) effective porosity $\phi_{EDZ,HAA-i}(r)$ and (b) effective hydraulic conductivity $K_{EDZ,HAA-i}(r)$ of the 24 HAA simulations after recovery of static formation pressure (late times). ....	92
Fig. 4-44:	Relationship between equivalent EDZ radius and homogenized porosity (upper left) and hydraulic conductivity (upper right), representative for of the HAA tunnel configuration. ....	93
Fig. 4-45:	Radial profiles of effective porosity $\phi_{EDZ,Shaft-i}(r)$ and effective hydraulic conductivity $K_{EDZ,Shaft-i}(r)$ of 9 shaft simulations models after recovery of static formation pressure (late times).....	94
Fig. 4-46:	Relationship between equivalent EDZ radius and homogenized porosity (upper left) and hydraulic conductivity (upper right), representative for of the Shaft configuration. ....	95
Fig. A3.1:	Distribution of initial hydraulic conductivity. ....	A-1
Fig. A3.2:	Temporal evolution of fracture desaturation. ....	A-2
Fig. A3.3:	Temporal evolution of pressure in the bentonite during resaturation. ....	A-3

# 1 Introduction

## 1.1 Background and motivation

The selection of sites for repositories for the disposal of radioactive waste in Switzerland is defined in the Sectoral Plan for Deep Geological Repositories ("SGT", SFOE 2008). The Swiss disposal concept foresees separate repositories for low- and intermediate-level waste (L/ILW) and for high-level waste (HLW) – or, as a possibility, both of them together in a so-called combined repository. In stage 1 of the Sectoral Plan several potential geological siting areas for the disposal of L/ILW and several potential geological siting areas for the disposal of HLW were selected. It is the objective of Stage 2 to select at least two sites for each repository type, followed by the selection of a single site for each repository type and the preparation of the application for the general licence in Stage 3. As a decision basis for the second stage of the site-selection process, so-called provisional safety analyses are to be elaborated. Together with further documents on the geological basis and studies on construction feasibility, the provisional safety analyses provide input for the qualitative and quantitative comparison of long-term safety of the proposed repository configurations in the candidate siting regions.

In the context of the provisional safety analyses the authorities have requested a balanced evaluation of the impact of repository induced effects on the long-term safety of the repository for SF/HLW and L/ILW. The key effects addressed are the pH-plume associated with the cement backfill of the L/ILW caverns, the accumulation and release of repository gases, the heat emission of the HLW canisters and the excavation damaged zone (EDZ) around the backfilled underground structures. Emphasis is on the thermo-hydro-mechanical and chemical evolution of the near-field around the disposal systems after repository closure, taking into account the full range of the site-specific geological conditions and the corresponding repository configurations as described in Nagra (2010). The present study feeds in the assessment of the repository induced effects in that it evaluates the hydraulic significance of the EDZ created during repository construction for the considered geological boundary conditions and repository configurations. The hydraulic evaluations draw on mechanical fracture network simulations with a hybrid finite/discrete element method (FEMDEM), conducted as part of a comprehensive sensitivity study for a variety of SF/HLW and L/ILW repository configurations (Geomechanica 2013).

## 1.2 Scope and objectives

The EDZ around the backfilled underground structures of a geological repository represents a viable release path for radionuclides as well as a possible escape route for corrosion and degradation gases. The efficiency of this release path depends on the shape and extent of the EDZ. This study draws on a geomechanical sensitivity analysis, which has been conducted to assess the extent and the shape of the EDZ around the underground structures of a geological repository for radioactive waste (Geomechanica 2013). The geomechanical simulations provided discrete fracture networks of the EDZ around the disposal structures for a wide range of possible repository configurations in the Opalinus Clay of the candidate siting regions in Northern Switzerland.

The discrete fracture networks, derived from the geomechanical simulations, are used in this study to evaluate the hydraulic significance of the EDZ. A sequential modeling procedure is developed, aimed at converting the discrete fracture networks into hydraulic continuum models with heterogeneous porosity and hydraulic conductivity distributions. In a next step, the

complex shape of the EDZ is abstracted towards a simplified representation, amenable to be handled with conventional SA modelling tools. Specifically, the scope of this study comprises:

- The elaboration of a traceable workflow for the conversion of the FEMDEM discrete fracture networks in equivalent porous medium models, representing the hydraulic conductance of the EDZ around backfilled tunnels and seal sections.
- Development and testing of a hybrid process model of porewater flow in fractured claystone, accounting simultaneously for both fracture flow in the excavation induced fractures and porous medium flow in the intact rock matrix.
- Enhancement of the aforementioned model to include hydro-mechanical processes in a simplified manner, such as swelling of the rock matrix and fracture closure in response to variations of effective stress.
- Implementation of the hydro-mechanical process model in a hydraulic model of the EDZ, representing the EDZ as an equivalent porous medium with a stress-dependent hydraulic conductivity distribution.
- Simulation of the self-sealing process in the EDZ around the backfilled underground structures in response to pore pressure recovery and swelling pressures caused by resaturation of the bentonite buffer.
- Analysis of hydraulic conductance of the EDZ for a variety of repository situations.

The evaluation of hydraulic conductance of the EDZ is conducted for a selection of FEMDEM simulations, representing the following components of the repository system: (i) an SF/HLW emplacement tunnel, (ii) a horizontal repository seal section and (iii) a vertical shaft seal section.

### **1.3 Report organization**

Chapter 1 presents the background and motivation for the present study. The objectives are specified and the report organization is discussed.

Fundamentals and basic theory required for the modeling tasks are summarized in Chapter 2. This chapter includes a state of the art on porewater flow in the EDZ (Chapter 2.1), with particular emphasis on flow on Opalinus Clays (Chapter 2.2).

Chapter 3 presents the details of the modelling and abstraction strategies. To that end, an EDZ model is used to illustrate each step of the methodology.

Chapter 4 summarizes the achievements and provides the main conclusions of the study.

The report ends up with some concluding remarks and a few suggestions for further research on the modelling of the hydraulic behavior of the EDZ around galleries for nuclear waste disposal in Opalinus Clay.

Appendix A contains a description of the output files in the digital appendix.

Appendix B reports on complementary simulations of two-phase flow models mimicking gas and fluid migration through the EDZ and on unsaturated models of the near field of emplacement galleries.

## 2 Fundamentals

### 2.1 Porewater flow in the EDZ – state of knowledge

At the Cluster Conference "Impact of the Excavation disturbed or damaged zone (EDZ) on the performance of radioactive waste geological repositories" in Luxembourg in November 2003, a general definition of the excavation damaged zone was agreed by the scientific community (Tsang et al. 2005): "The Excavation damaged zone (EDZ) is a zone with significant irreversible processes and significant changes in flow and transport properties. These changes, for example, can include one or more orders of magnitude increase in flow permeability".

The creation and evolution of the EDZ in various host rock formations was the issue of international research activities within the NF-PRO Integrated Programme as part of the Sixth Framework Programme (2002-2006) of the European Community. In this context, a State-of-the-Art report was elaborated by Alheid et al. (2007), covering the key processes, phenomena and features of the EDZ evolution for a variety of host rock formations, including crystalline rock, rock salt, soft clays and indurated clays. The subsequent paragraphs summarise the essentials of contributions with focus on indurated clays.

Indurated clays such as the Opalinus Clay are characterized by a transient strength behaviour exhibiting ductile yielding and also brittle failure. Discrete fractures are quite common in such materials. However, detailed studies in indurated clays (Gautschi 2001) showed that such brittle structures do not form water conducting features as long as they are exposed to significant effective compressive stresses (e.g., at overburden depths more than 200 m in Opalinus Clay). Natural fracture zones in indurated clays, which were extensively tested in boreholes and in the Mont Terri Underground Rock Laboratory (URL) similarly do not show a significant increase of hydraulic conductivity compared to intact rocks (Nagra 2002). Correspondingly, excavation induced fracture zones may influence the design of a repository because of their lower strength but their long-term hydraulic conductance may be of limited importance.

Within the construction phase of a geological repository, the tunnels will be driven into the rock and the rock responds more or less immediately to the creation of the new free surfaces. Part of the deformation already happens as pre-deformation in front of the tunnel face (Martin 1997; Yong 2007) while deformation continues during excavation and even after the face advances beyond the point of observation due to the loss of the support function of the tunnel face. The EDZ, an area containing discrete excavation induced fractures and micro-fractures around tunnels is a common phenomenon for all rock types. The damage zone is controlled by the excavation technique and by the stress redistribution around the tunnel when the strength is exceeded in its vicinity. In indurated clays, rock deformation is complicated by distinct hydro-mechanical coupled processes. The hydro-mechanical coupling is a time-dependent process, which is governed by the low hydraulic conductivity of the rock. The geometry of the EDZ can become complex as it is controlled by:

- Stress tensor (mean stress and deviator stress)
- Geomechanical rock properties (stiffness, strength and anisotropy thereof)
- Tectonic and sedimentary inhomogeneity of the rock mass (fractures, lithofacies variabilities)
- Shape of the tunnel
- Tunnel support and ground interaction
- Drying or wetting of the rock due to ventilation or other operations

Most discrete features in the EDZ in indurated clays are caused directly by the short-term excavation-induced unloading (undrained elasto-plastic response) and are of extensional nature (Fig. 2-1a). For weaker rocks or under high deviatoric stresses these features may be replaced by shear failure. In the case of anisotropic rocks (e.g., bedded rocks, low-grade metamorphic rocks), an activation of the planes of weakness can be observed (Fig. 2-1b). This failure process can be of extensional or shear origin.

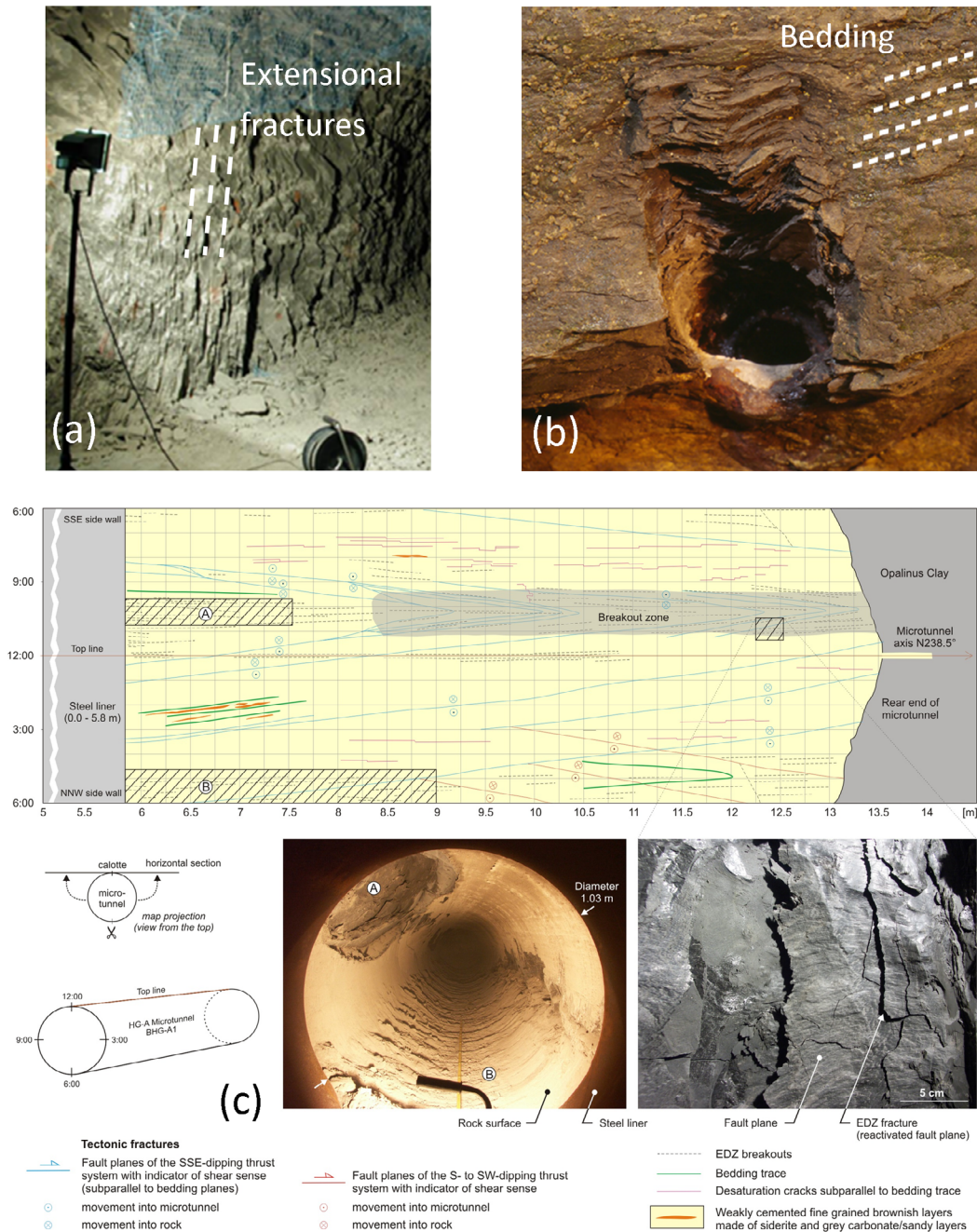


Fig. 2-1: Excavation induced damage zones in Opalinus Clay: (a) Spalling process leading to an EDZ in the Mont Terri URL (Nagra 2002); (b) bedding related failure in the EDZ of a small borehole (Blümling et al. 2007); (c) interaction of stress controlled EDZ fractures with tectonic structures (Marschall et al. 2006).

Abundant observations on EDZ fractures were made in boreholes, niches, tunnels and galleries of the Mont Terri URL (Figs. 2-2 and 2-3). Detailed studies on the spacing of the extensional fractures and their coalescence mechanisms with shear fractures to form composite fracture planes were carried out by Yong (2007).

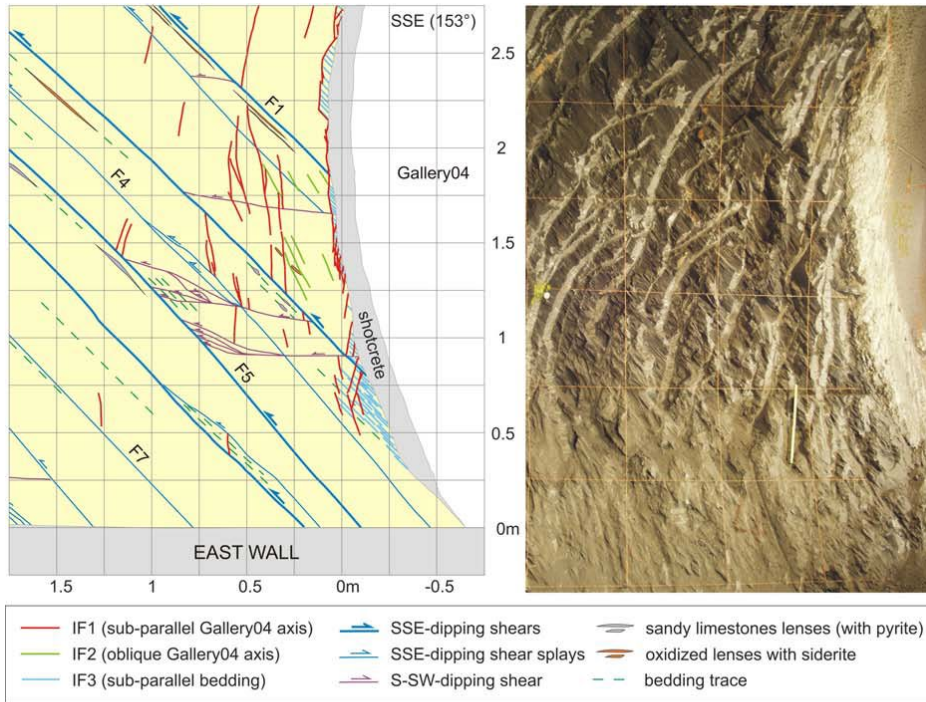


Fig. 2-2: Induced fracturing in the east walls in the EZ-B Niche entrance (Yong 2007).

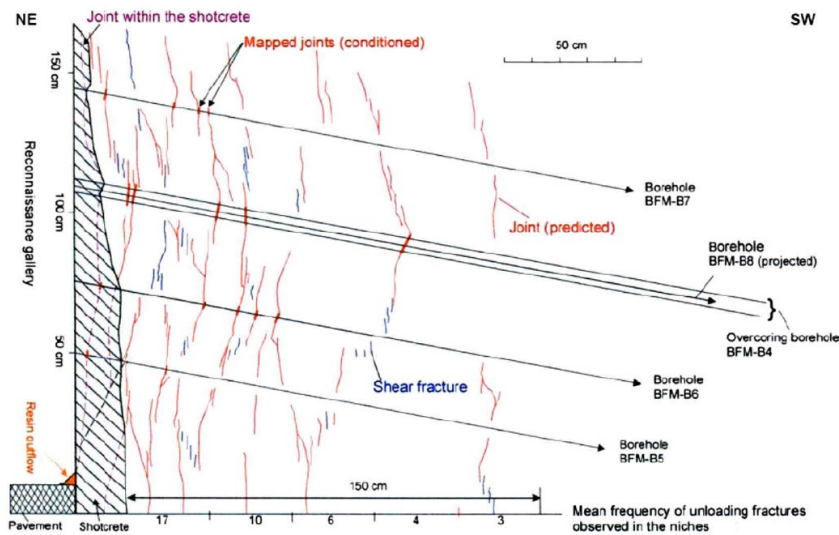


Fig. 2-3: Coalescence of extension and shear fractures to form a network of composite fracture planes observed in the sidewall of the Reconnaissance Gallery at Mont Terri (modified from Thury and Bossart 1999; see also Appendix 4 in Bock et al. 2010).

Yong (2007) reports a comparison of fracture density in boreholes around tunnels and niches at Mont Terri using data from over 100 boreholes (see Fig. 2-4). All structures other than those clearly related to tectonic features or drill core handling were counted over 0.5 m intervals. Almost 75% of the boreholes were drilled into the side-walls and data has been normalized per borehole to reduce the bias. Fracture count in the first 0.5 m can be as high as 10 (mean spacing 5 cm) around some excavations but typically reduces to less than 2 at 3 m from the tunnel wall. Detailed investigation of macro fracturing around the EZ-B niche suggested a much narrower zone of macro-fracturing ~ 20 cm in thickness with an outer zone extending to 70 cm of reduced seismic velocity.

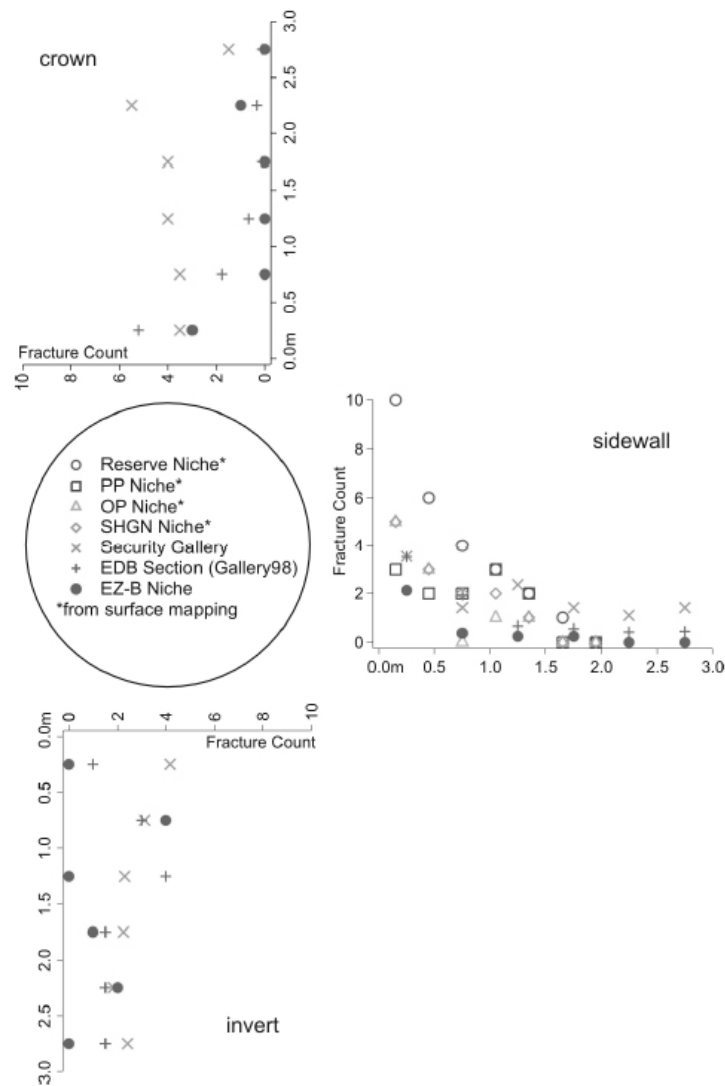


Fig. 2-4: Fracture counts in 0.5 m borehole intervals from around the EZ-B Niche and previous sub-parallel excavations (from Yong 2007).

**Permeability Measurements**

Small-scale in situ permeability measurements in the EDZ at the scale of underground works in indurated clays have been conducted in the Kimmeridgian marls of Bure site (Wileveau & Bernier 2008, Shao et al. 2008, Baechler et al. 2011), in the Opalinus Clay at Mont Terri and in

Tournemire (Matray et al. 2007). Measurements have been carried out in the damaged (macroscopically fractured) zone, the disturbed (micro-fractured zone) and the intact rock.

Most permeability measurements in the EDZ at Mont Terri were made in boreholes equipped with multi-packer systems oriented radial to the drift, isolating measurement intervals of 10 to 50 cm at various distances from the wall. Pulse tests (SEPMI probe and MMPS equipment, Bossart & Thury 2008) and constant head tests (MMPS equipment) were used. In the partly de-saturated rock, which corresponds closely to the excavation damaged zone, pneumatic tests were used to investigate the local effective permeability.

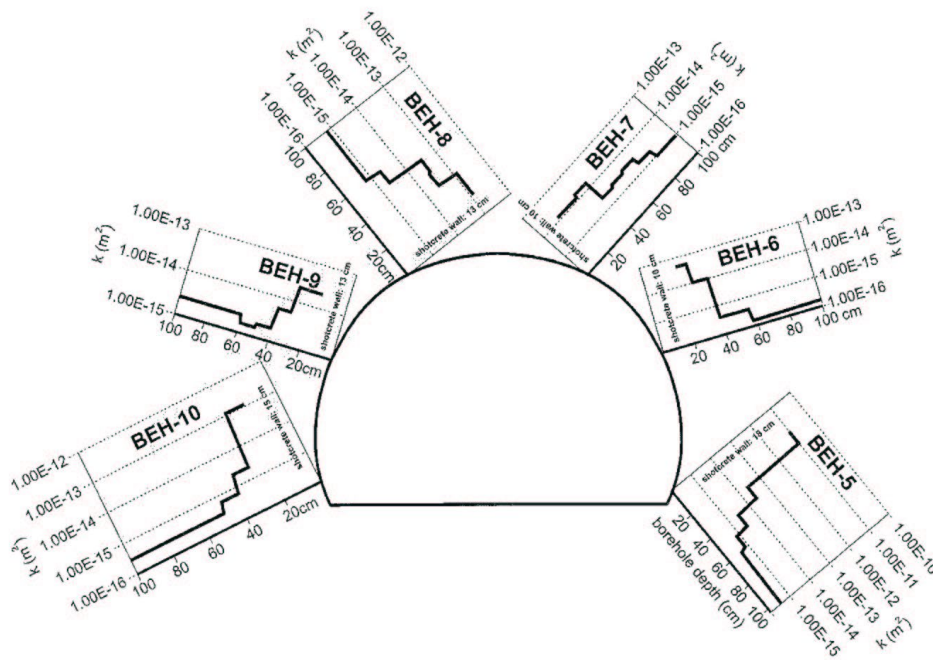


Fig. 2-5: In situ permeability measurements conducted in Mont Terri experimental drift (from Bossart and Thury 2008).

Permeability values obtained within the sidewall of an experimental drift in the Mont Terri underground laboratory vary considerably and can be shown to depend on fracture density and interconnectivity (Bossart and Thury 2008). Fig. 2-5 shows that the permeability is increased by several (up to 6 or 7) orders of magnitude within 20 to 40 cm from the tunnel. This zone coincides with the extent of high fracture density in the rock. A similar reduction in permeability with depth into the rock is reported by Shao et al. (2008) for Bure.

Observations of fracture and fracture network properties at larger scales are limited. In the framework of the EZ-A experiment at the Mont Terri URL transmissivity tests were performed in a 9 borehole array in some 6 m<sup>2</sup> of the floor of a drill and blast tunnel. Cross-hole pneumatic responses were detected within 3 boreholes over 3.3 m, however permeability and hydraulic responses were highly variable and the tested area was thought to have been highly disturbed (Armand et al. 2004). Tests using multiple boreholes in the EH experiment at Mont Terri showed that fracture connectivity was limited to ~ 1 m (Martin & Lanyon 2003).

## 2.2 Conceptualisation of porewater flow in Opalinus Clay

### 2.2.1 Geological setting and basic rock characteristics

The Opalinus Clay is part of a thick Mesozoic - Tertiary sedimentary sequence in the Molasse Basin of Northern Switzerland. It was deposited about 180 Ma ago in a shallow marine environment. Geological investigations on the regional scale confirmed the remarkable homogeneity of the formation. In the candidate siting regions of Northern Switzerland the Mesozoic sediments reveal uniform thickness over a distance of several tens of kilometres, dipping gently to the south-east, and are hardly affected by faulting.

The Opalinus Clay is a moderately over-consolidated claystone that has been formed by a complex burial and compaction history with two distinct periods of subsidence during the Cretaceous and late Tertiary, respectively. In the Molasse Basin the greatest burial depth of the Opalinus Clay was about 1000 m below the present depth. From about 10 Ma ago, alpine uplift and erosion brought the Opalinus Clay progressively up to its present burial depth. At Mont Terri, the Opalinus Clay reached a maximum depth of about 1000 m and the present burial depth is about 200 - 300 m.

On a regional scale, the mineralogical composition of the Opalinus Clay exhibits moderate lateral variability and a slight increase in clay content with depth. Quantitative laboratory analyses of core samples from Benken, Schlattingen and Mont Terri provide a total mass fraction of clay minerals of 40 - 80%, a quartz content of 15 - 35% and 5 - 25% calcite. The fraction of swelling clay minerals, with 10 - 15% illite / smectite mixed layers, is of particular interest for the gas-related studies. Further minerals are siderite, pyrite and feldspar. The mass fraction of organic carbon is < 1%.

Porosity depends on clay content and burial depth; average values of 10%, 12% and 16% are reported for Schlattingen, Benken and Mont Terri Rock laboratory, respectively. Figure 3-1 depicts a compilation of porosity measurements from various locations in Northern Switzerland as a function of the burial depth. A clear decrease of porosity with depth is observed. Further geotechnical characteristics of the Opalinus Clay have been determined as part of comprehensive laboratory programmes, revealing moderate stiffness (Young's modulus in the range 5 - 15 GPa), moderate strength (UCS values of the intact rock matrix between 10 and 35 MPa) and distinct swelling pressures (0.5 - 2 MPa).

Hydraulic tests have been performed in the Opalinus Clay in the Riniken, Schafisheim and Benken boreholes. Beauheim (2013) carried out a detailed review of the packer test data, applied methods and associated uncertainty providing an evaluation of the test interpretations quality. Field investigations suggest a hydraulic conductivity of the Opalinus Clay in the order of  $10^{-13}$  to  $10^{-14}$  m/s.

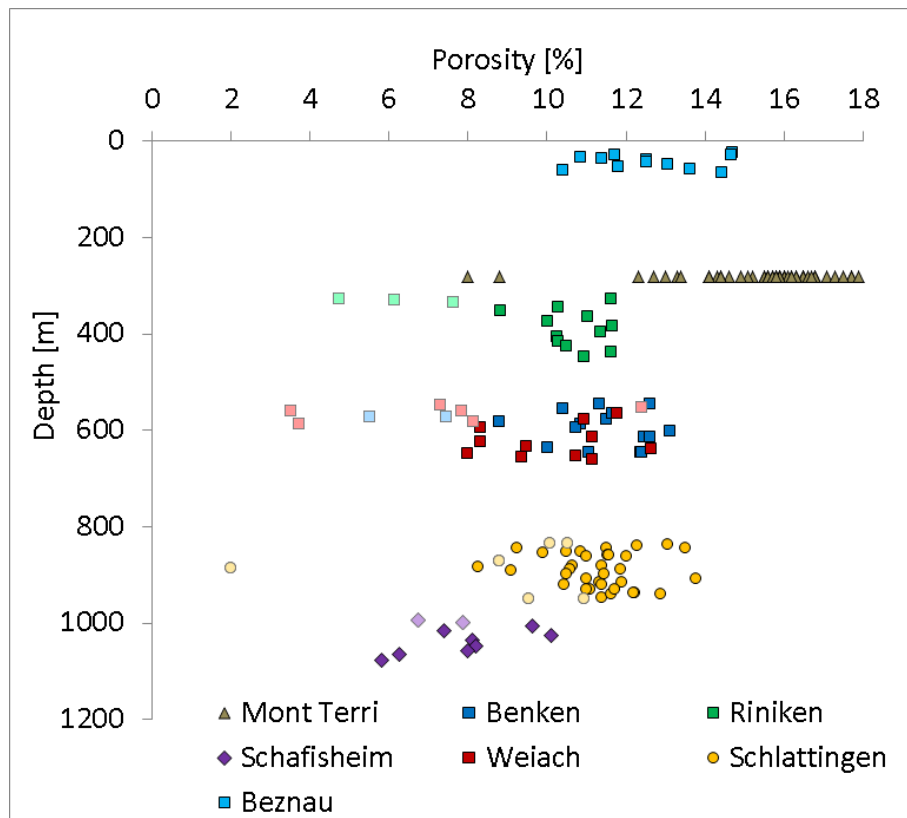


Fig. 2-6: Depth dependency of porosity measured in Opalinus Clay core samples recovered from different depths (after Senger et al. 2013).

Over the course of the Mont Terri research programme, a comprehensive hydrogeological investigation programme has been conducted. Some of the key achievements regarding porewater flow in the Opalinus Clay were summarized in Bossart and Thury (2008):

- Hydrogeological evidence on different investigation scales confirms that the Opalinus Clay at Mont Terri exhibits the features of a typical seal formation, characterized by rather homogeneous hydraulic properties. Hydraulic packer testing in boreholes and permeameter testing with drillcore specimen exhibit consistently low values for hydraulic conductivity, typically in the range between  $5 \times 10^{-12}$  and  $1 \times 10^{-14}$  m/s (see also Senger et al. 2013).
- No significant variations in hydraulic conductivity are seen among the different facies. A reference value of  $5 \times 10^{-13}$  m/s has been reported for the Opalinus Clay at Mont Terri.
- Localised porewater inflow towards the galleries is observed only at a very few locations; in most cases localized inflow is linked to excavation phenomena. The highest packer tests transmissivities recorded for the Opalinus Clay at Mont Terri, which cannot be explained by EDZ phenomena are  $< 1 \times 10^{-10}$  m<sup>2</sup>/s.

No marked enhancement of hydraulic conductivity has been measured in the vicinity of tectonic features, indicating that tectonic fractures in the Opalinus Clay are tight. Extensive packer testing in the main fault did not reveal any correlation between hydraulic conductivity and fracture frequency along the boreholes.

### 2.2.2 Permeability of the intact rock matrix

#### Depth/stress dependence of porosity and permeability

The Opalinus Clay is an indurated, overconsolidated claystone. When the rock is exposed to changing stress conditions in an elastic deformation regime, a logarithmic relationship holds for the inter-dependence between void ratio and mean effective stress (Fig. 2-7; see also Nagra 2004):

$$e = e_{\kappa 0} - \kappa \cdot \ln \frac{\sigma'_m}{\sigma'_0} \tag{2-1}$$

- e - void ratio, [-]
- $\kappa$  - negative slope of the *rebound-reconsolidation line* (RRL), [-]
- $e_{\kappa 0}$  - Intercept of the void ratio at effective mean stress  $\sigma' = \sigma'_0$ , [-]

where the mean effective stress is defined as:

$$\sigma'_m = \frac{\sigma_1 + \sigma_2 + \sigma_3}{3} - p_w = \frac{\sigma'_1 + \sigma'_2 + \sigma'_3}{3} \tag{2-2}$$

- $\sigma_i$  - principle stress components, [Pa]
- $\sigma'_i$  - principle components of effective stress ( $\sigma_i - p_w$ ), [Pa]
- $\sigma'_m$  - mean effective stress, [Pa]
- $p_w$  - porewater pressure, [Pa]

and porosity  $\phi$  (-) can be calculated from the void ratio, using:

$$\phi = \frac{e}{1 + e} \tag{2-3}$$

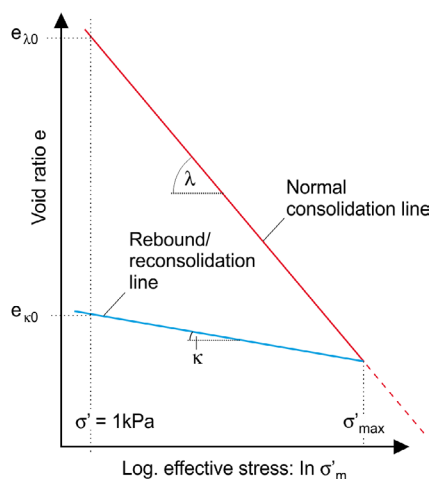


Fig. 2-7: Volumetric deformation behaviour of Opalinus Clay: normal consolidation and rebound/ reconsolidation in response to changes of mean effective stress (from Nagra 2004).

Senger et al. (2013), Ferrari et al. (2013) and Romero & Gomez (2013) consider the permeability of the Opalinus Clay based on packer tests, geophysical log analyses and core testing from deep boreholes. The dependence of porosity and permeability on effective stress determined from tests on cores is shown in Fig 2-8. Low porosity typically corresponds to core samples with low clay content and high carbonates content. A consistent trend in porosity reduction with effective stress can be observed, although each sample shows the influence of overburden and mineralogy. Hydraulic conductivity is typically below  $10^{-13}$  m/s for effective stresses greater than 20 MPa and reduces further to  $\sim 10^{-14}$  at 100 MPa. The power-law relationship between porosity and  $\log K$  is illustrated in Fig. 2-9.

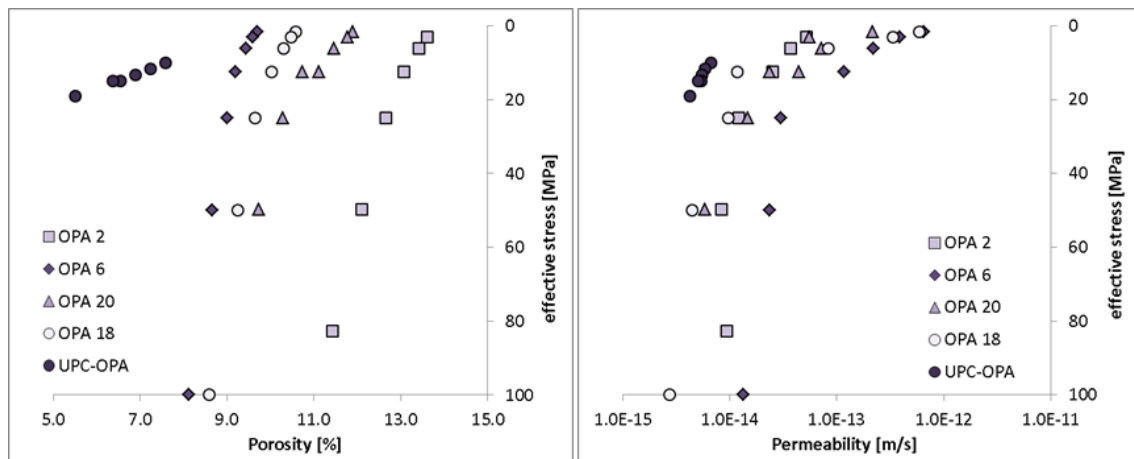


Fig. 2-8: Depth dependency of porosity (left) and hydraulic conductivity (right) derived from tests on Opalinus Clay core samples under different effective stresses (from Senger et al. 2013). Light colors denote core samples with clay content below 40% (or carbonates content above 25% when clay content was not available).

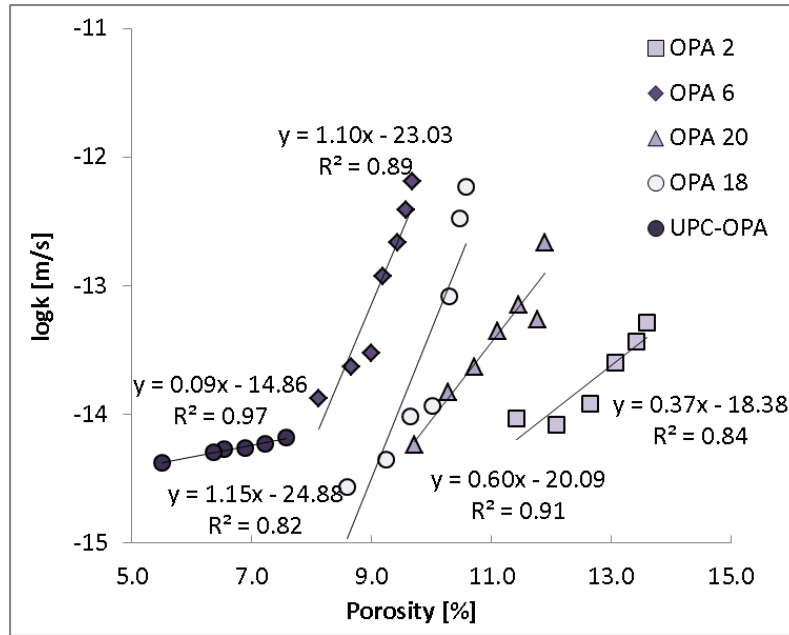


Fig. 2-9: Correlation between hydraulic conductivity and porosity measured under different effective stresses in Opalinus Clay core samples, from Ferrari et al. (2013) and Romero & Gomez (2013).

**Correlation with petrophysical properties**

Clay content, porosity and specific surface data obtained from the laboratory analysis of Opalinus Clay core samples have been used to infer matrix hydraulic conductivity based on the Kozeny-Carman relationship (Kozeny 1927; Carman 1937 and 1956):

$$K = \frac{\phi^3}{(1-\phi)^2} \cdot \frac{\rho_w \cdot g}{\tau^2 \cdot (\rho_s \cdot S) \cdot C_s \cdot \mu_w} \tag{2-4}$$

where  $\rho_s$ ,  $\rho_w$  and  $\mu_w$  are grain density, fluid density and fluid viscosity, respectively.  $\phi$  is porosity,  $S$  is specific surface,  $g$  is gravitational acceleration,  $\tau$  is a tortuosity factor (usually:  $\tau = \sqrt{2}$  in the absence of independent experimental evidence) and  $C_s$  is a shape factor, ranging between  $C_s = 2$  (circular cross-section capillary) and  $C_s = 3$  (parallel plate flow). More recently, Yang & Aplin (2010) proposed an empirical relationship for shales:

$$K = \frac{\rho_w g}{\mu} \exp(b)$$

$$b = -69.59 - 26.79 f_{clay} + 44.07 f_{clay}^{0.5} + (-53.61 - 80.03 f_{clay} + 132.78 f_{clay}^{0.5}) e + (86.61 + 81.91 f_{clay} - 136.61 f_{clay}^{0.5}) e^{0.5} \tag{2-5}$$

where  $f_{clay}$  is the clay fraction and  $e$  represents the void ratio:  $e = 1/(1+\phi)$ .

Further details of the approach are given in Senger et al. (2013). The resulting hydraulic conductivity values are plotted versus clay content in Fig. 2-10 together with hydraulic conductivity values measured in core samples. The plot shows an overall trend of hydraulic conductivity, which slightly increases first and then decreases with increasing clay content. The values predicted with by Yang and Aplin formula are approximately 1 to 2 orders of magnitude below the values calculated via Kozeny-Carman relationship. The comparison indicates that the range of measured hydraulic conductivities is bounded by the two approaches.

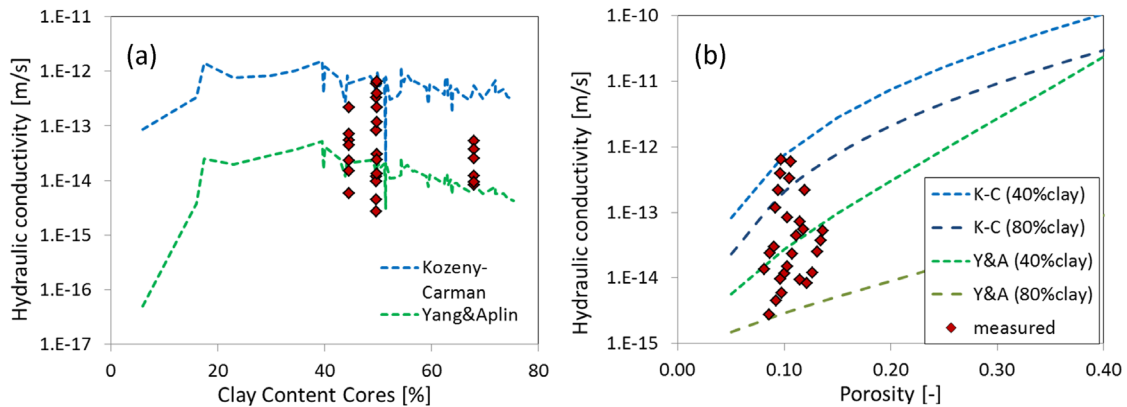


Fig. 2-10: Comparison of the hydraulic conductivity indicators after Kozeny-Carman (K-C) and Yang&Aplin (Y&A) with the available measurements in Opalinus Clay core samples: (a) clay content versus hydraulic conductivity and (b) porosity versus hydraulic conductivity (assumed clay content<sup>1</sup>: 40 and 80%, respectively).

### Reference values for the siting regions in Northern Switzerland

Senger et al. (2013) compiled representative hydraulic data bases and derived the corresponding hydraulic reference parameters for all host rocks in the candidate siting regions, comprising hydraulic conductivity, K-anisotropy, porosity and lower bound of fracture pressure. For the Opalinus Clay, two different sets of reference parameters were specified, namely for the shallow and deep repository configurations (shallow: 300 – 500 m bg.; deep: 500 – 900 m bg). The reference and alternative values (as qualitative indicators of the range of uncertainty) are summarized in Table 2-1.

<sup>1</sup> In the Kozeny-Carman equation, another empirical correlation is used to convert the clay content in an equivalent specific surface:  $S[m^2/kg]=0.4254*CC[\%]+2.0088$ .

Tab. 2-1: Reference values for the gas-related parameters of the undisturbed Opalinus Clay for a shallow/deep repository in Northern Switzerland (RV – reference value; AV – alternative value).

Parameter	RV	AV	Remarks
<b>Opalinus Clay – shallow (300 – 500 m bg)</b>			
Intrinsic permeability normal to bedding $k_{\perp}$ [m <sup>2</sup> ]	1×10 <sup>-20</sup>	2×10 <sup>-21</sup> (1)  5×10 <sup>-20</sup> (2)	RV: corresponds to the reference value for hydraulic conductivity at Mont Terri. AV <sup>(1)</sup> : corresponds to the reference value for hydraulic conductivity in the Zürich Nordost. AV <sup>(2)</sup> : corresponds to the upper range for hydraulic conductivity at Mont Terri.
Anisotropy coefficient $k_{\parallel}/k_{\perp}$	5	1	RV: according to Nagra (2002), Romero and Gomez (2013). AV: no significant anisotropy
Total porosity [%]	12%	16%	AV: Porosity of the shaly facies at Mont Terri: 16%. RV: corresponds to the reference value for the porosity of the ZNO area. At Mont Terri, the sandy facies exhibits typical porosity values of about 12%
<b>Opalinus Clay – deep (500 – 900 m bg)</b>			
Intrinsic permeability normal to bedding $k_{\perp}$ [m <sup>2</sup> ]	2×10 <sup>-21</sup>	1×10 <sup>-21</sup>	RV: corresponds to the reference value for hydraulic conductivity at Benken (Nagra 2002). AV: corresponds to the lower range for hydraulic conductivity at Benken.
Anisotropy coefficient $k_{\parallel}/k_{\perp}$	5	1	RV: according to Nagra (2002). AV: no significant anisotropy
Total porosity [%]	12%	10%	RV: Porosity measurements from Schlattingen core (OPA-20) (avg. Value between different core samples) 16%. AV: corresponds to the lower value in OPA-of about 10%
Relationship between intrinsic permeability and hydraulic conductivity (20°C):			
$k \left[ m^2 \right] = \frac{\eta_w}{\rho_w \cdot g} \cdot K \approx 1 \times 10^{-7} \cdot K \left[ m/s \right]$			
$\eta_w$ - dynamic viscosity of water, [Pa·s] $\rho_w$ - density of water, [kg m <sup>-3</sup> ] $g$ - gravitational acceleration, [m s <sup>-2</sup> ]			

### 2.2.3 Transmissivity of tectonic fractures

As stated in Chapter 2.1, none of the discontinuities observed in Nagra's deep boreholes at Benken, Riniken, Weiach and Schafisheim revealed enhanced permeabilities of faults or fractures in comparison to the rock matrix. Even though faults, shear-zones and joints have been observed in Opalinus Clay at different locations and depths in tunnels intersecting the formation, significant transmissivities ( $\sim 10^{-10}$  m<sup>2</sup>/s) were not observed at locations with overburdens greater than 200 m. The tightness of fractures at overburden > 200 m was explained by the efficient self-sealing capacity of Opalinus Clay (Nagra 2002).

In Nagra (2004), a simple conceptual model was presented which explains mechanical closure of transmissive fractures caused by the increase of normal effective stress on the fracture plane (e.g., increase of total stress due to increasing overburden), whereas reactivation of a tight fracture was described by the reduction of normal effective stress (e.g., increase of pore pressure in the fracture). Figure 2-11 displays a conceptual sketch of a rock joint subjected to a normal stress  $\sigma_n$  and porewater pressure  $p_{pw}$ . The joint is characterised by a geometric and hydraulic aperture (i.e., effective to flow),  $a_p$  and  $a_h$  respectively, and the normal joint stiffness  $K_n$ . Bandis et al. (1983) developed a simple relationship between the aperture of the joint and the normal effective stress for hard rocks:

$$a_h = a_{ho} \cdot \left(1 - \frac{\sigma_n'}{a_{ho} \cdot K_{no} + \sigma_n'}\right) \quad (2-6)$$

where:

- $K_{no}$  - normal joint stiffness for  $\sigma_n' = 0$  [Pa m<sup>-1</sup>]
- $a_{ho}$  - joint aperture for  $\sigma_n' = 0$  [m]
- $\sigma_n'$  - effective normal stress ( $\sigma_n - p_{pw}$ )  $\geq 0$ , [Pa]

Equation (2-6) indicates that the joint has an aperture  $a_{ho}$  when it is completely unloaded, i.e., when effective normal stress is zero. The joint will progressively close with increasing normal effective stress. The cubic law (Witherspoon et al. 1980; De Marsily 1986), provides a relationship between hydraulic aperture  $a_h$  and fracture transmissivity  $T_f$ :

$$T_f = \frac{\rho_w \cdot g \cdot a_h^3}{12 \cdot \eta_w} \quad (2-7)$$

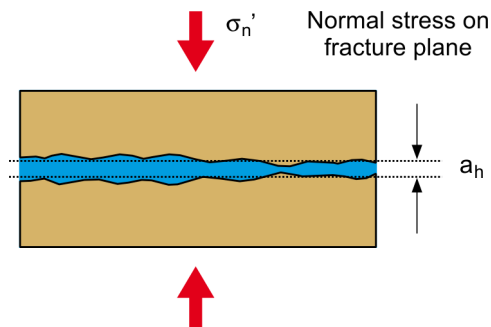


Fig. 2-11: Dependency between fracture aperture and normal effective stress after Bandis et al. (1983). The fracture will close when the effective stress increases.

As part of the GS experiment at Mont Terri, hydraulic tests were performed in a borehole before and after a combined hydro- and gas-frac (Nagra 2004). Testing was conducted in the test interval which contained the hydrofrac (Fig. 2-12a). Interval transmissivity increased by 5 - 6 orders of magnitude when the injection pressure exceeded the normal stress on the fracture plane (Fig. 2-12b). For low injection pressures, however, the interval transmissivity was indistinguishable from that of the intact rock ( $T \leq 1 \times 10^{-12} \text{ m}^2 \text{ s}^{-1}$ ). These findings can be explained by the dependence of fracture transmissivity (or hydraulic conductivity) on effective



- Sedimentation and filtration of solid particles carried by the liquid phase (e.g., colloids)
- Precipitation of dissolved minerals on the fracture planes

Sedimentation, filtration and precipitation are of limited relevance for the assessment of self-sealing processes in the EDZ, because a significant water flow through the fractures is required to make these processes efficient. Hence, mechanical fracture closure and swelling are the self-sealing mechanisms to be considered here.

*Mechanical closure of fractures* in response to normal and shear stresses is controlled by a multitude of factors such as fracture geometry (orientation, extension, fracture density, joint roughness), hydro-mechanical properties of the rock mass (elastic moduli, strength, hydraulic conductivity of the rock matrix) and in-situ state conditions (stress state, pore pressure, water saturation, porewater chemistry). A simple model, that describes fracture closure in terms of fracture stiffness and mean normal effective stress, has been presented in Chapter 2.2.2.

*Swelling and disaggregation of clay minerals* are chemical-osmotic processes that contribute to the closure of fractures. Swelling pressures were measured on Opalinus Clay cores, ranging between 0.5 and 2 MPa. Swelling heave tests on unconfined core samples revealed typical swelling strains in the order of 10 millistrains.

Several field experiments have been conducted as part of the Mont Terri Project to demonstrate the self-sealing capacity of excavation-induced fractures and to investigate the time dependence of the self-sealing process. The experiments account for the combined action of mechanical and chemical-osmotic fracture closure.

Bossart et al. (2002) performed a sequence of hydraulic single hole and interference tests in the EDZ of an open tunnel section. The test results indicated a significant reduction of the EDZ transmissivity over a period of 800 days from  $5 \times 10^{-7} \text{ m}^2 \text{ s}^{-1}$  to  $2 \times 10^{-9} \text{ m}^2 \text{ s}^{-1}$  (Figure 2-13). During the subsequent test phase, a load plate was installed and the EDZ was subjected to radial stresses between 1 and 5 MPa to simulate bentonite swelling pressures in a backfilled emplacement tunnel (Figure 2-13). A further drop in transmissivity of two orders of magnitude to  $2 \times 10^{-11} \text{ m}^2 \text{ s}^{-1}$  was observed (Nagra 2002).

Within the EZ-A experiment 10 short boreholes ( $\sim 2 \text{ m}$ ) were drilled into the EDZ in the floor of the tunnel after injection tests using Pearson water traced with fluorescein. The cores showed a high density ( $\sim 10 \text{ m}^{-1}$ ) of induced or reactivated features in the first 40 cm of rock. The surfaces of artificial fractures were notably wet and mapping identified self-sealing features as shown in Figure 2-14.

Larger scale measurements of axial flow along the EDZ (parallel to the excavation axis) are very limited due to the difficulty of establishing a head-gradient along an excavation in operational conditions (Lanyon 2011). Within the HG-A experiment the axial flow of water and gas around a 3 m long packer seal (layout shown in Fig. 2-15) has been studied over several years (Marschall et al. 2013). A 13 m long, 1 m diameter micro-tunnel was excavated in the Opalinus Clay at Mont Terri. The micro-tunnel was sealed with a Megapacker after instrumentation.

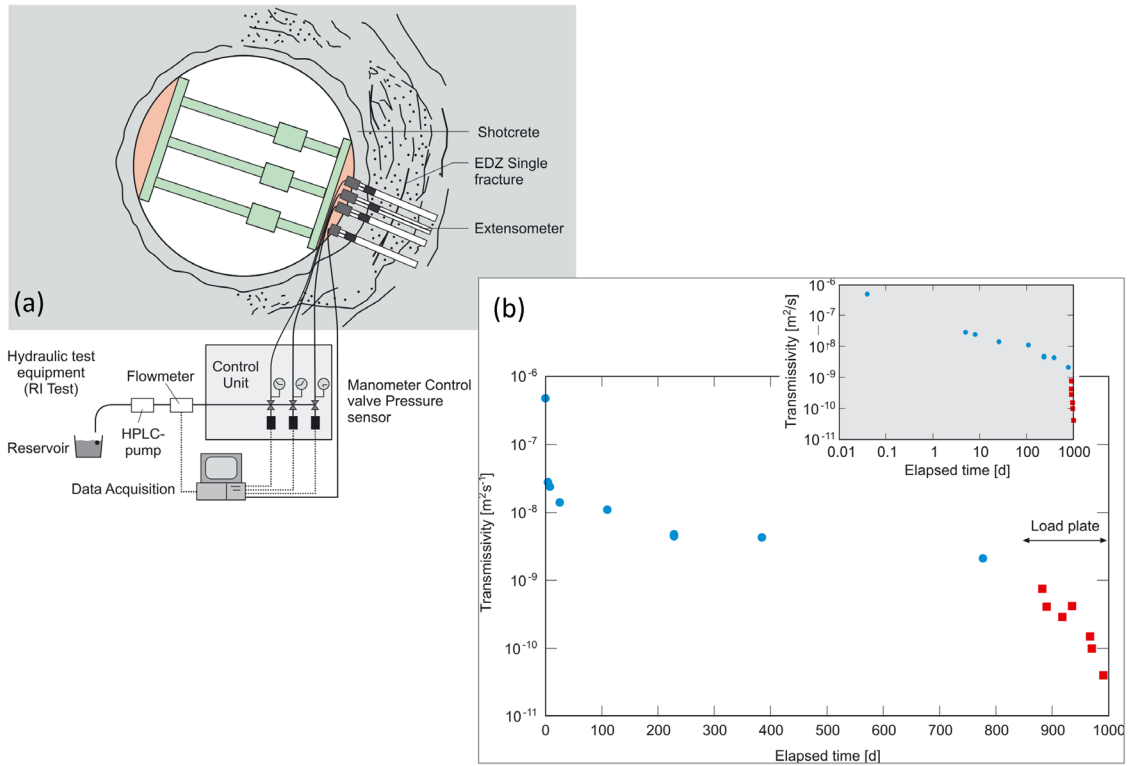


Fig. 2-13: Long-term changes in EDZ transmissivity in an open tunnel section at the Mont Terri Rock Laboratory (after Nagra 2004): (a) sketch of the experimental set-up and (b) long-term monitoring of EDZ transmissivity. Initially, the EDZ was saturated for a period of 800 days (blue dots) and EDZ transmissivity was monitored periodically. Afterwards, a load plate was installed (1 - 5 MPa) and the transmissivity measurements were repeated.

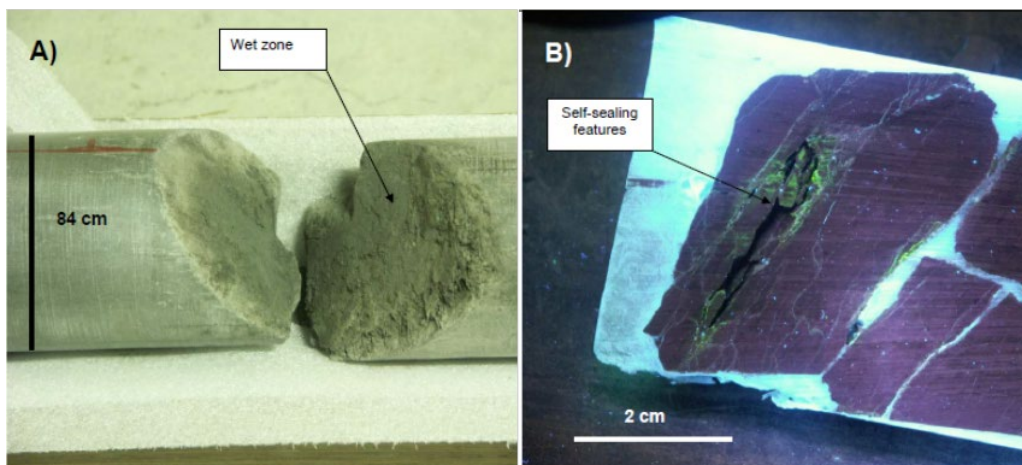


Fig. 2-14: Sample core from EZ-A boreholes: a) core showing wet zone along fracture; b) self-sealing feature showing fluorescein dye from previous injection tests.

Following emplacement of the Megapacker a year-long saturation period was followed by extensive multi-rate injection testing over 2 years. Water was injected into the test section at the end of the micro-tunnel. During the multi-rate test the injection rate was reduced from an initial 10 ml/min to less than 0.1 ml/min as the permeability of the EDZ dropped. The Sealing Index  $S$  (ml/min/kPa) – a simple measure of the conductance of the EDZ – was calculated from the applied injection rate and the test section pressure and is shown in Figure 2-16.

$$S = \frac{Q}{P_{\text{Test section}} - 100 \text{ kPa}} \quad \text{and} \quad K_{\text{effective}} [m/s] = 5 \cdot 10^{-7} \cdot S \quad (2-8)$$

The overall conductance of the EDZ dropped by several orders of magnitude over the test period and recovered quickly after gas injection tests. A steady decline in the Sealing Index is visible with the exception of two periods when the Megapacker pressure was reduced to a level below the test section injection pressure, resulting in low effective stress conditions within the EDZ that led to an increase in EDZ conductance as shown in Fig. 2-16. At the end of the observation period, the effective hydraulic conductivity  $K_{\text{EDZ}}$  of an equivalent radial EDZ with a cross-sectional area of 1 m<sup>2</sup> is around 2E-12 m/s.

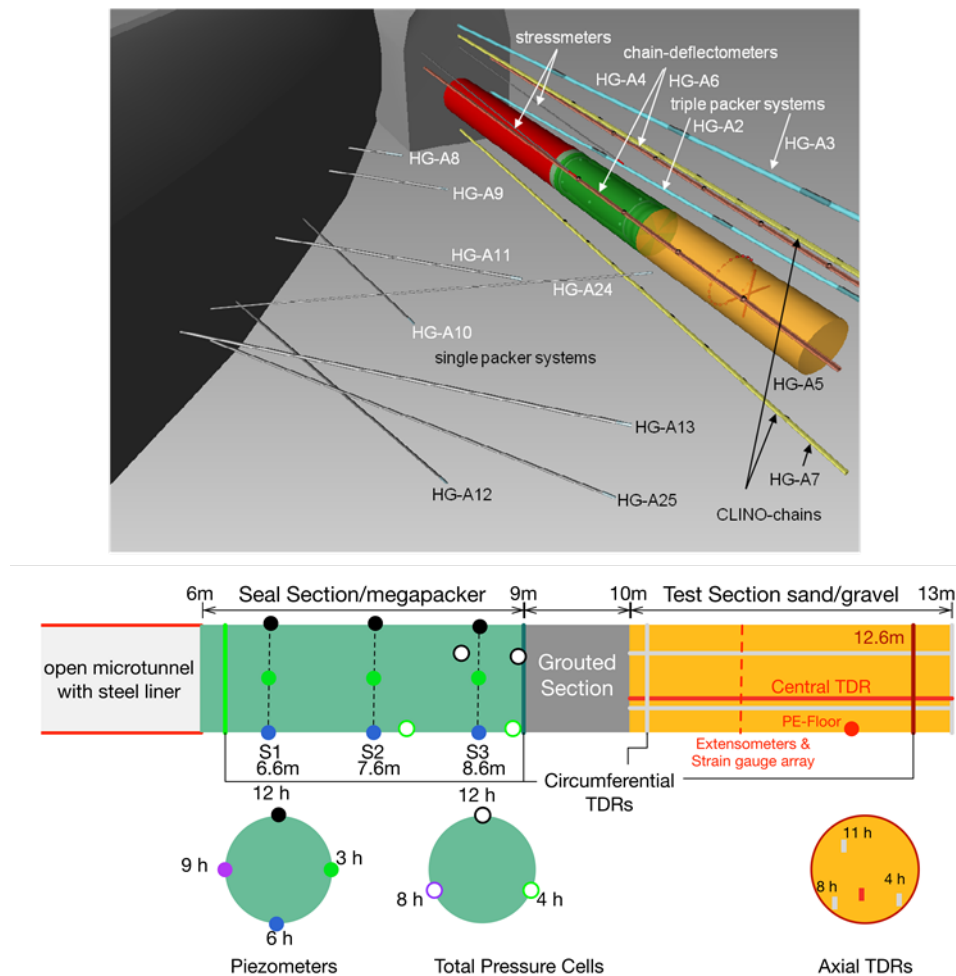


Fig. 2-15: The HG-A experiment in the Mont Terri URL (Marschall et al. 2013): experimental layout (top) and microtunnel instrumentation (bottom).

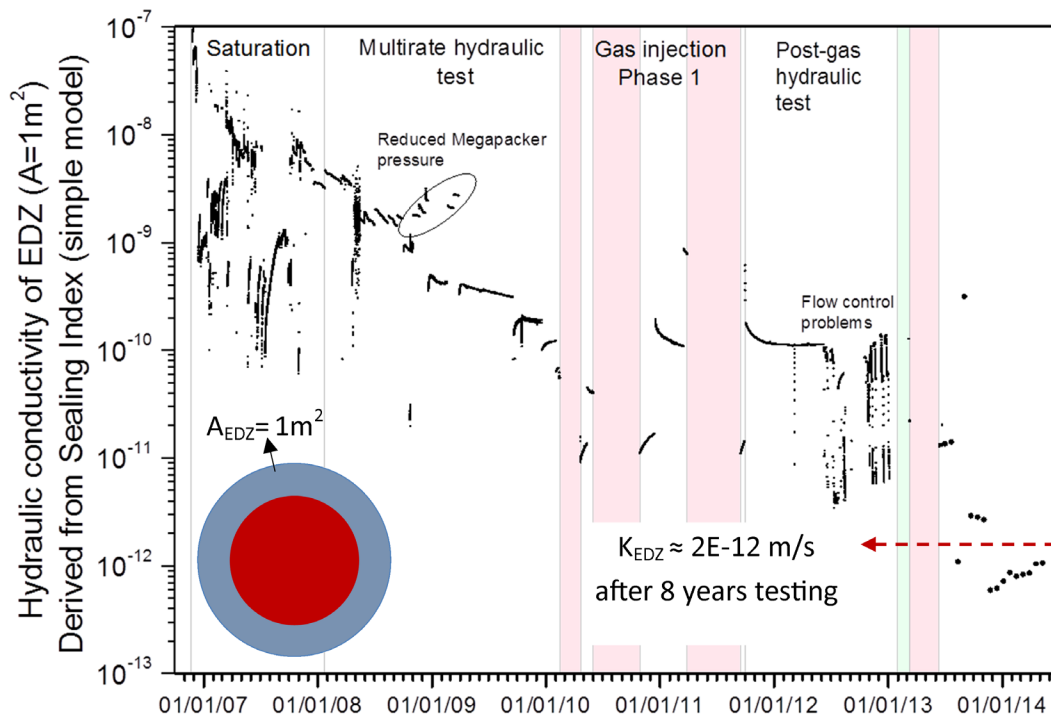


Fig. 2-16: Sealing index for HG-A experiment showing reduction in ability to inject water into the Test Section due to reduction in EDZ conductance. At the end of the observation period, the effective hydraulic conductivity of an equivalent radial EDZ with a cross-sectional area of  $1 \text{ m}^2$  is around  $2\text{E-}12 \text{ m/s}$ .

### 2.2.5 A conceptual framework for EDZ fracture closure in Opalinus Clay

Drawing on the presented empirical and experimental evidence about the hydraulic significance of the EDZ during tunnel construction, its evolution during operational times and after backfilling of tunnels, the functional requirements associated with a quantitative EDZ closure model can be formulated as follows (see Fig. 2-17):

- The creation of the EDZ is a brittle process, i.e. the increase of the void volume of the plastified rock zone around the excavation is solely attributed to the fracture opening, whereas the porosity of non-fractured rock domains remains essentially unchanged during the early times.
- Initially, the newly created EDZ fractures are unsaturated and exposed to atmospheric pressure, whereas the non-fractured rock domains remain saturated and exhibit high matrix suction as a consequence of the high gas entry pressure of the Opalinus Clay. The initial transmissivity of the unsaturated EDZ fractures is controlled by the fracture aperture and can be very high. The matrix conductivity remains essentially unchanged, i.e. it is the same as the conductivity the intact rock.
- With time the matrix suction in the rock matrix ceases out due to the uptake of pore water from outer rock zones and the fractures start to resaturate.
- Porewater uptake of the non-fractured rock zones is associated with swelling and consequently with an increase of matrix porosity. This porosity increase of the rock matrix happens at the expense of fracture aperture, i.e. the fractures start to close and fracture transmissivity reduces drastically, whereas the hydraulic conductivity of the non-fractured matrix zones increases slightly as a consequence of the porosity increase.

- This process of porosity and conductivity increase of the matrix is associated with the decrease of fracture aperture and transmissivity progresses until the equilibrium of effective stress is reached. This is essentially the case, when pore pressure reaches the static formation pressure.

In the Chapter 3, a heuristic EDZ model is developed, which mimics the aforementioned functional features in a simplified manner. The evolution of porewater flow along the EDZ is simulated spanning over the entire period ranging from the early post excavation phase until static formation pressure recovery.

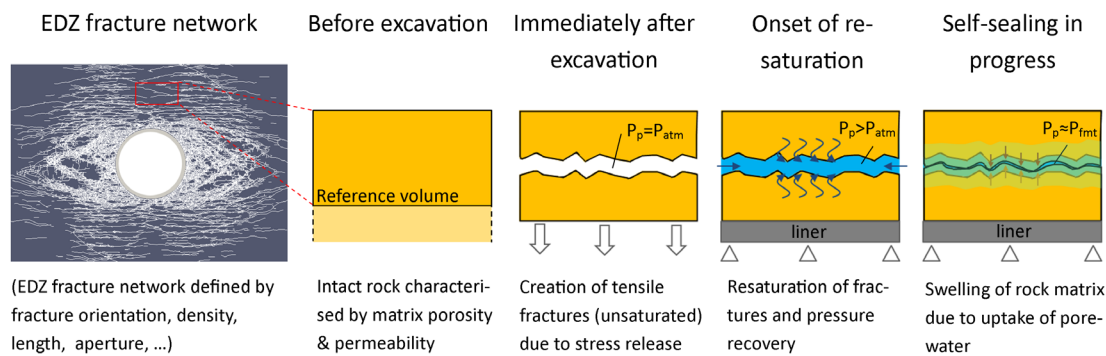


Fig. 2-17: A conceptual framework for EDZ fracture closure in Opalinus Clay, covering the key phenomena and features from the early post excavation phase until static formation pressure recovery.

### 2.3 Previous EDZ Abstractions for Safety Assessment

Performance assessment studies of the EDZ in Opalinus Clay have previously conceptualized it as a composite structure consisting of two concentric shells (EDZ-i, EDZ-o as shown in Fig. 2-18), whose radii depend on the local tunnel radius and on the orientation of the tunnel axis with respect to the principal horizontal stress direction (Nagra 2002). The division into two zones follows the concept by Bossart et al. (2002), i.e., a connected fracture system is assumed to exist within the inner zone while any fracturing in the outer zone is assumed to be disconnected.

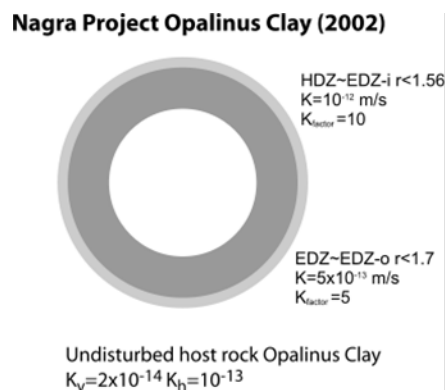


Fig. 2-18: Nagra's EDZ conceptualisation (Lanyon 2011): The reference case is shown, although the assessment included "what-if" scenarios with higher EDZ hydraulic conductivity or the absence of EDZ (for gas studies).

An approach to the derivation of effective properties for performance assessment models of the EDZ, based on geological and hydraulic characterization of the EDZ Discrete Fracture Network is given in Lanyon & Senger (2011) and illustrated in Fig. 2-19. The approach assumes generation of a range of models from an evaluation of attribute/parameter uncertainties.

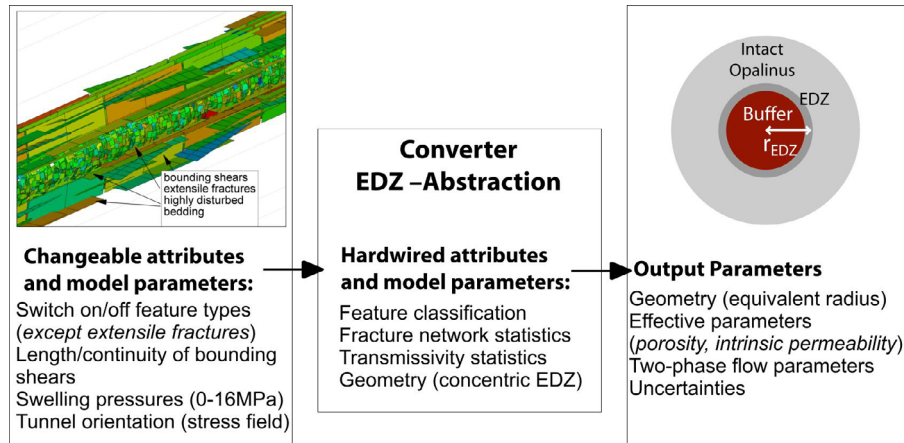


Fig. 2-19: Components of the EDZ converter: input (definition of parameters / experts), hardwired EDZ abstraction procedure and output for end users (from Lanyon & Senger 2011).

The underlying DFN models are converted to equivalent porous medium (EPM) models using the approach suggested by Jackson et al. (2000). Inverse modelling of gas flow in the EDZ is then used to derive effective properties suitable for performance assessment. An example of a single realization of a DFN model and the equivalent porous medium model are shown in Fig. 2-20.

Gas migration through the EDZ was simulated using the heterogeneous EPM with the TOUGH2 code. Appropriate effective properties for a homogeneous single-shell EDZ model were then derived using the ITOUGH inverse model as shown in Fig 2-21.

A similar approach is presented by Hawkins et al. (2011) for a repository in the Callovo-Oxfordian (COX; Fig 2-22).

The DFN models used in Lanyon & Senger (2011) were based on a synthesis of data from Mont Terri and 2D mechanical models of the expected evolution of the EDZ around repository tunnels. The models presented in the next section are derived from newer, more advanced, FEMDEM models of the EDZ (Geomechanica 2013).

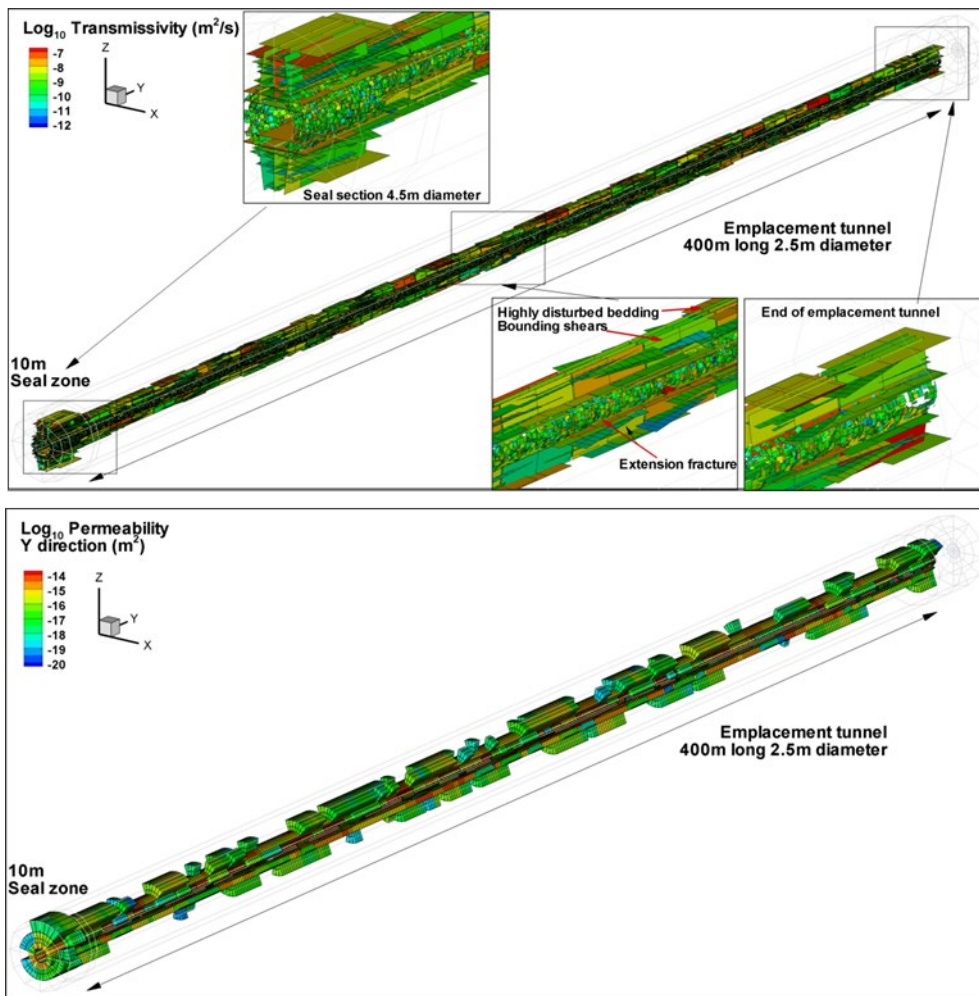


Fig. 2-20: DFN (upper) and EPM (lower) models of the EDZ along a 400 m tunnel in Opalinus Clay (from Lanyon & Senger 2011).

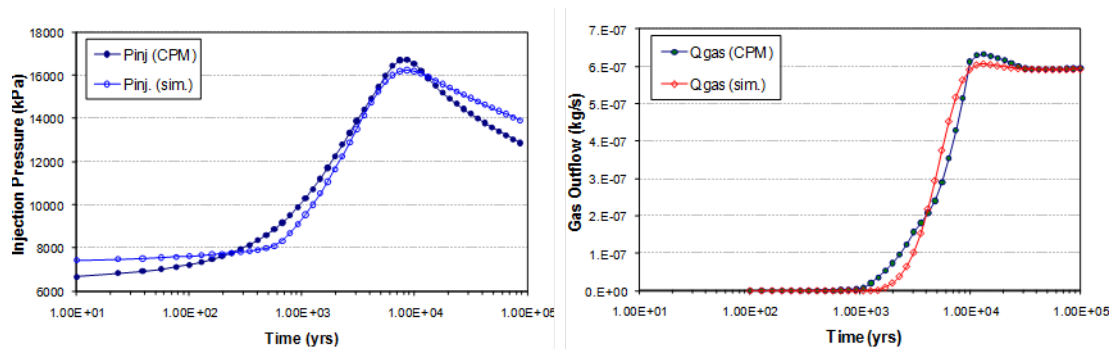


Fig. 2-21: Simulated response to gas injection: left: pressure; right: gas flow for equivalent heterogeneous CPM model and simplified single-shell effective property model.

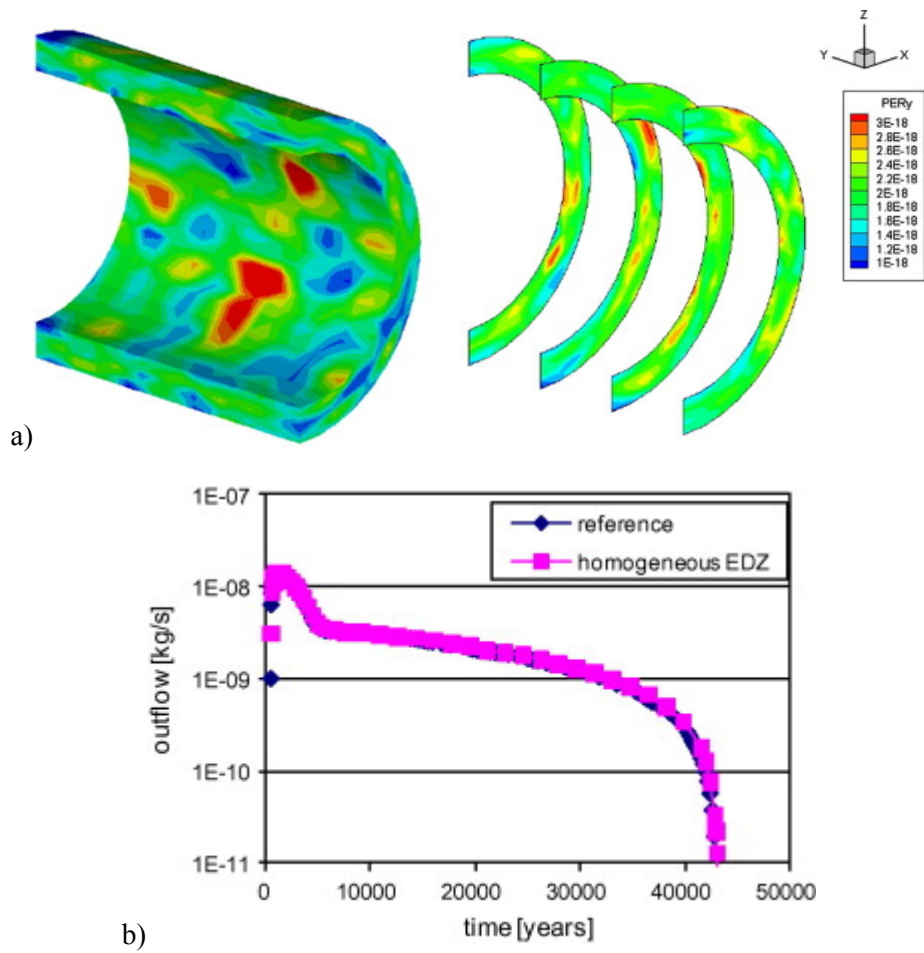


Fig. 2-22: EDZ model for tunnel in COX from Hawkins et al. (2011): a) distribution of axial permeability in heterogeneous CPM model; b) gas flow for equivalent heterogeneous CPM model and simplified single-shell effective property model.

### 3 EDZ model abstraction for Safety Assessment - Methodology

#### 3.1 Expectations and model requirements

The Excavation Damaged Zone (EDZ) around underground structures is a zone with significant plastic deformation and significant changes in flow and transport properties. These changes can include one or more orders of magnitude increase in flow permeability (Tsang et al. 2005). Previous Safety Assessment studies of the EDZ in Opalinus Clay were based on idealized representations, assuming concentric shells (single shell or double shell, respectively) with enhanced hydraulic conductivity, the radius of which depends on the local tunnel radius and the orientation of the tunnel axis to the principal horizontal stress direction (Nagra 2002). The idealized EDZ of seal sections and access tunnels retained typically an enhanced hydraulic conductivity of 10 times that of undisturbed Opalinus Clay and a thickness of less than a tunnel radius. The so-called "EDZ-converter" (Chapter 2.3) provided a new modelling tool for the abstraction of complex EDZ fracture networks to simplified representations with equivalent flow and transport characteristics. The approach made explicit use of geological and hydraulic data, associated with the in-situ characterization of EDZ fracture networks in open tunnels. In the framework of SGT – Stage 2, further endeavors were made to develop a versatile workflow for EDZ abstraction with the following expectations:

- To cope with the full range of geological, hydrogeological and geomechanical conditions in the candidate siting regions and the associated conceptual and parametric uncertainties. In this context, particular emphasis has been given to an appropriate consideration of the extent and shape of the EDZ as a function of the in-situ stress conditions and repository depth.
- To cover a wide range of geomechanical phenomena and processes, associated with the creation of the EDZ during construction and the evolution thereof during operational times and after backfilling of the underground structures (brittle failure of the rock, drainage, re-compaction, self-sealing of EDZ fractures).
- To meet in a consistent way the experimental evidence on EDZ self-sealing, which has been gained as part of in-situ experiments in underground rock laboratories (see Chapter 2.2.4).

In the present report hydraulic EDZ abstractions are derived for cylindrical tunnel cross-sections, assuming that Opalinus Clay is the host rock. The approach consists of the following steps (Fig. 3-1):

- A geomechanical sensitivity analysis was conducted to assess the extent and the shape of the EDZ around the underground structures of a geological repository for radioactive waste (Geomechanica 2013). The geomechanical simulations with a discrete element model (FEMDEM) provided discrete fracture networks of the EDZ around the repository structures for a wide range of possible repository configurations in the Opalinus Clay of the candidate siting regions in Northern Switzerland.
- The FEMDEM fracture networks consist of thousands of fractures, each of them characterized by fracture orientation, fracture length and fracture aperture. A box counting approach is applied to convert the fracture networks into cell-based porosity distributions.
- An empirical porosity-permeability relationship (Kozeny-Carman) is adopted to convert cell porosities in hydraulic conductivities.
- Cell-based porosity and conductivity distributions are converted in a shell defined by a radius and homogeneous porosity / conductivity.

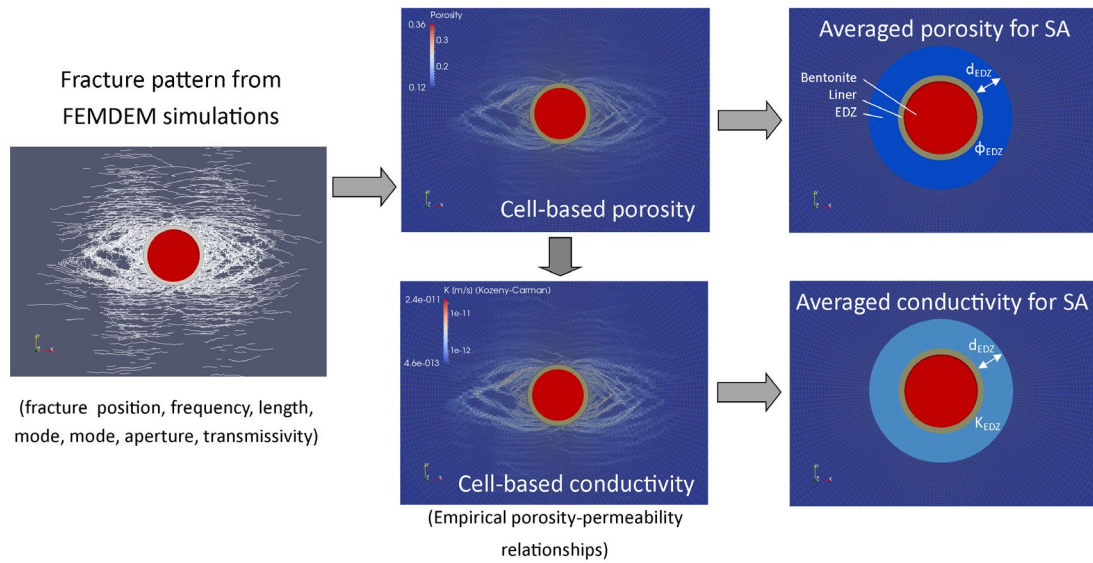


Fig. 3-1: Concept of the EDZ abstraction process for a circular tunnel (diameter 2.8 m): representative fracture patterns are simulated for relevant repository configurations with a discrete element model. The discrete fracture patterns are converted in heterogeneous porosity and conductivity distributions. In a final abstraction process, the heterogeneous porosity / conductivity distributions are converted in a shell defined by a radius  $r_{EDZ} = r_{tunnel} + d_{EDZ}$  and homogeneous porosity / conductivity.

### 3.2 Model implementation – General workflow

A traceable approach is required to implement the aforementioned concept of EDZ abstraction in a numerical model. The general workflow for the modeling of the EDZ around circular tunnels and seal sections of a geological repository is based on the conceptual framework given in Chapter 2.2.5 and consists of five main steps (Fig. 3-2). These are outlined below and presented in detail in the following subsections.

The starting point is a 2-D FEMDEM (Fig 3-2a) consisting of composite fracture patches characterized by a certain length and orientation, aperture and failure/propagation mode (i.e., tensile, shear or torsion). FEMDEMs are the main outcomes of fracture mechanics simulations conducted in 2-D cross sections for representative repository configurations in the candidate siting regions, drawing on the geomechanical characteristics of the Opalinus Clay as the host rock formation (after Geomechanica 2013).

The first step of the suggested workflow consists of calculating some statistics of the FEMDEM. These are presented as histograms (Figure 3-2c). While this step is ancillary, it helps to detect some spurious effects in the input data sets (e.g., very long fractures with very small aperture).

The second step consists of generating a finite element mesh (Figure 3-2b) over which the aforementioned FEMDEM properties will be mapped and converted to hydraulic properties. Given that the flow towards the gallery will be pseudo-radial, the selected grid resembles radial flow conditions. Radial grids present several advantages if compared to regular grids with square or rectangular elements, e.g., ability to locally refine at zones of interest, absence of artificial grid anisotropy, etc. From the programming standpoint, search algorithms relying on the concept of radial distance are also more efficient than global search algorithms based on Cartesian coordinates. In addition, they are easy to implement. Radial search algorithms demand

a circular shape of the gallery, what forces us to exclude momentarily the L/ILW sections in this study. A major effort to accommodate irregular galleries like L/ILW is being made and will be documented elsewhere.

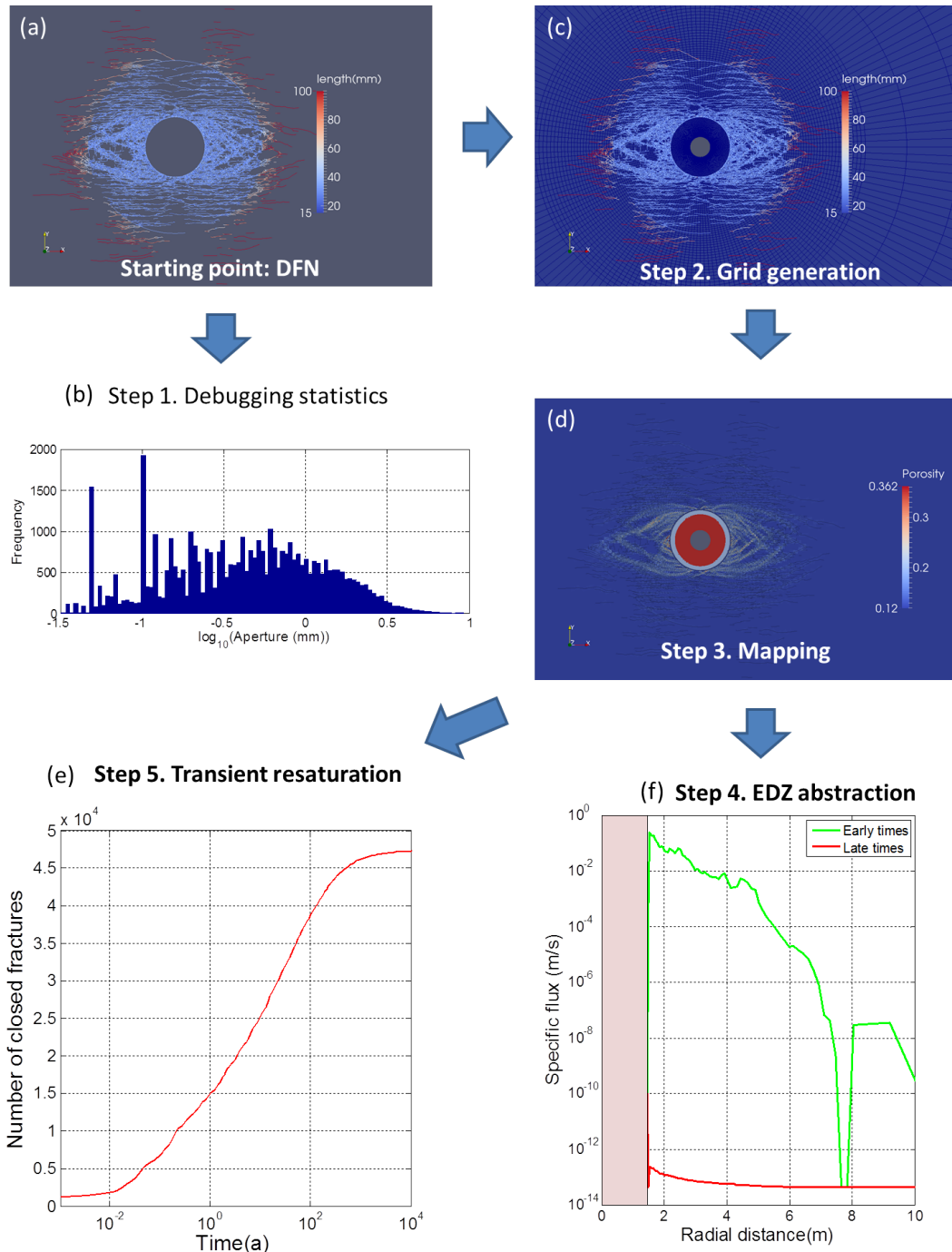


Fig. 3-2: Basic features and steps of the modeling strategy: (a) FEMDEM as input data set; (b) radial grid over which geometric properties of the FEMDEM are mapped, (c) debugging statistics of the FEMDEM, (d) mapping of hydraulic properties (total porosity in this case), (e) transient simulation of the resaturation of the system (in the figure, temporal evolution of number of closed fractures), (f) early and late time abstractions of the EDZ.

The third step consists of mapping fracture geometric properties, i.e., trace length (over each cell) and aperture to hydraulic properties governing fluid flow to the gallery caused by resaturation. To that end, transmissivity and porosity of the fractures intersecting a cell are upscaled to a single value of hydraulic conductivity and porosity.

Once hydraulic properties have been mapped to cells, abstractions of the EDZ (in the sense of simplified models) (step 4; Figure 3-2f) and fluid flow simulations mimicking the resaturation of the system (step 5; Figure 3-2e) can be carried out.

A salient feature of the transient simulations presented here is that hydraulic parameters of both fracture and matrix evolve with time as a response to resaturation (see Chapter 3.3.4).

Two abstractions of the EDZ are made, i.e., at early times after excavation and emplacement of the canisters, and at late times, after full resaturation of the system. The latter is of particular interest towards safety analysis. This simplified model alleviates the computational burden of carrying out complex risk analysis models. The abstractions of the EDZ are built upon the axial specific fluxes across the section (i.e., circulating volume per unit area under unit hydraulic head gradient parallel to the gallery).

The aforementioned steps are described in detail in the following subsections. To that end, we make use of the HAA-01 FEMDEM and go through all steps of the methodology describing its details. The main features of the HAA-01 FEMDEM are summarized in Table 3-1.

Tab. 3-1: Basic description of the HAA-01 FEMDEM, used to show the workflow.

Diameter of the circular gallery pre-deformation	3 m
Shotcrete thickness	20 cm
In situ stress conditions (MPa)	$\sigma_v = 19.6$ ; $\sigma_h = 15.7$
Shotcrete stiffness (GPa)	32 GPa
Core softening ratio	0.01
Strength parameters	2 x lab calibrated values for Opalinus Clay

### 3.3 Discrete fracture network representation of the EDZ

#### 3.3.1 Basic input

FEMDEM simulations supplied by Geomechanica Inc. (after Geomechanica 2013) are summarized in csv files. Each fracture is defined by an identification code (ID) and a 4-points polygon contained on the vertical cross-section. In addition, the file reports on:

- Failure mode: 1 for tensile opening, 2 for shearing, 3 for torsion (i.e., a combination of modes 1 and 2) and 4 for fractures within the gallery (removed, as the excavation and emplacement processes are assumed to be instantaneous). Figure 3-3 displays a sketch of the basic fracture modes.
- Fracture aperture.
- Fracture inclination with respect to the x axis and measured counterclock-wise.
- Fracture area.

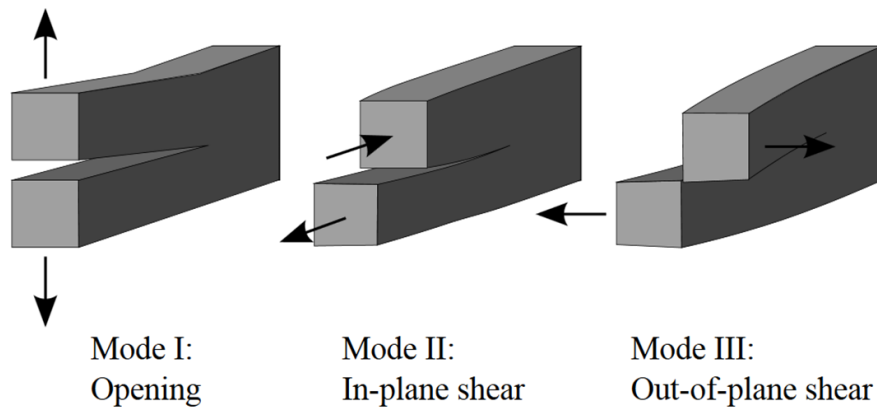


Fig. 3-3: Fracture failure modes.

### 3.3.2 Pre-processing of data

Prior to further calculations, fractures within the tunnel (i.e., those flagged with break mode = 4 in the csv files) are removed because the corresponding length is very large  $\sim 3$  m, what leads to very large fracture transmissivities and wrong results. The original csv files do not report on fracture length, a key element in the mapping of geometric to hydraulic properties. Fracture length is therefore re-calculated from fracture polygons.

Figure 3-4 displays the notation for the fracture polygons used in this work. First, the mid points A and B along the shortest fracture segments (1-4 and 2-3 in the sketch) are identified. Fracture length is then calculated as  $L_{AB}$  and the fracture aperture as  $a = 0.5 \cdot (d_{14} + d_{23})$ . Fracture transmissivity is then calculated from aperture according to the cubic law in Equation 2-7. Fluid density and viscosity are set to  $1'000 \text{ kg/m}^3$  and  $0.001 \text{ Pa}\cdot\text{s}$ , respectively, for consistency with previous works (Lanyon and Senger 2011). Some fractures have zero area (and aperture; Figure 3-4 right) due to a poor precision in the fracture node location in the csv files. These fractures are attributed with a residual aperture of  $8.9 \cdot 10^{-8} \text{ m}$ , what leads to an irreducible transmissivity of  $5.7 \cdot 10^{-16} \text{ m}^2/\text{s}$ . Sometimes the sorting of nodes leads to a distorted geometry of the fracture with a very large aperture and very small length (e.g., sorting counterclockwise in Figure 3-4a). Such cases are easily detected in the histograms of geometric properties (Figure 3-5) and the nodes are re-ordered in a coherent manner.

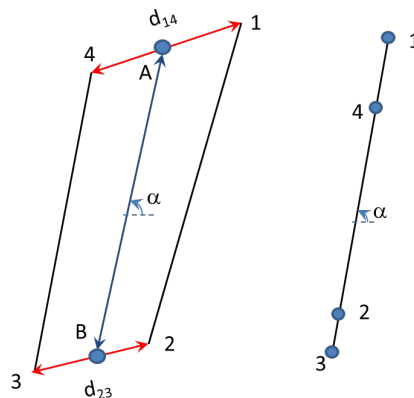


Fig. 3-4: Basic notation for the 4-nodes polygon defining a fracture. On the right, extreme case of fractures with zero aperture.

The aforementioned calculations are carried out for all fractures and histograms of fracture geometric properties and transmissivity are drawn (Figure 3-5). Also, quartiles of these parameters are reported as text files. The automated script also plots histograms and statistics of fracture parameters split by fracture mode (not displayed here) to facilitate the identification of outliers.

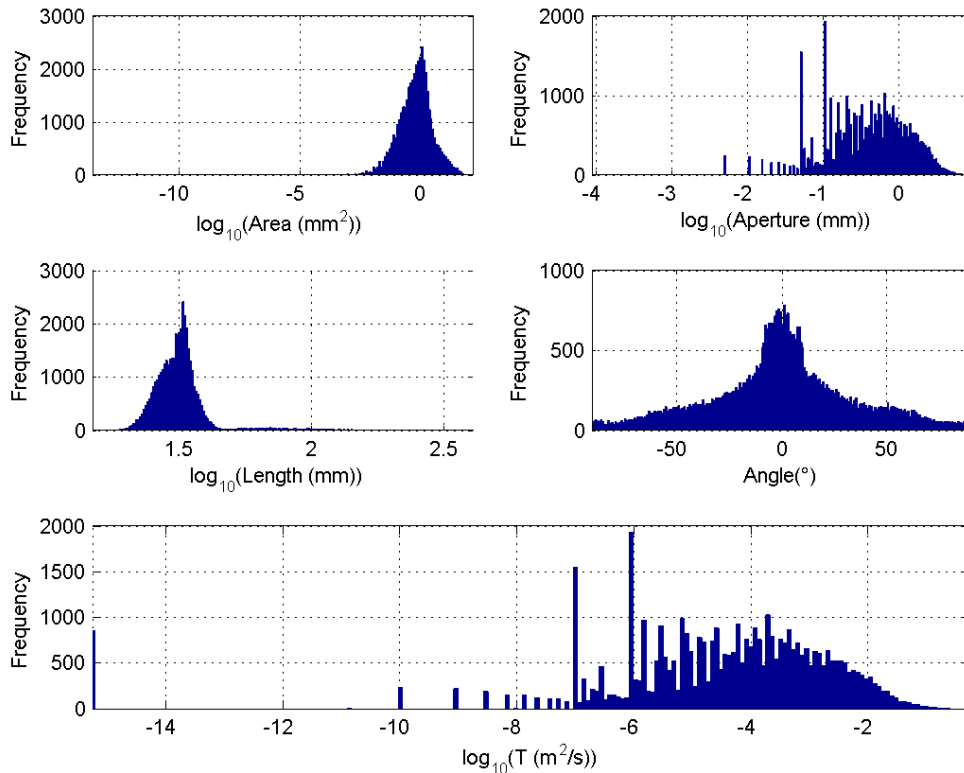


Fig. 3-5: Histograms of fracture parameters.

Figure 3-6 displays the geometric variables characterizing the FEMDEM. As observed in panel (a), the inclination of fractures is most prominent in the horizontal direction, although the spread, as measured by the standard deviation (Figure 3-5) is important. Panel (b) displays the length of the fracture patches. It may look like that fracture lengths are small and uniform around the gallery. However, one must bear in mind that fractures are a composite of patches, most of them of small length. As such, composite fractures can be (and actually are) very long. Panel (c) displays fracture areas, which are small in average.

Figure 3-7a displays the initial fracture aperture, as derived from the geometry of the FEMDEM. Fracture aperture diminishes monotonically with radial distance away from the gallery because the response to the excavation is smaller. One can observe an anisotropic distribution of fracture apertures (or transmissivities). The anisotropy is most prominent in the horizontal direction as a consequence of the deformation of the liner. This issue will be further discussed in the next section. Figure 3-7b displays fracture aperture at late times after full resaturation of the system. As observed, fracture aperture is constant and equal to the irreducible aperture because we assume that all fractures are closed. Finally, Figures 3-7c and d report on fracture transmissivity at early and late times respectively. These are derived from fracture aperture through the cubic law. Figure 3-7e displays the number of fractures intersecting cells along trace lines at inclinations 0, 45 and 90°. In average, 10 to 20 fractures define the EDZ in

different directions along the first 6 m. However, one can observe peaks of 40 to 50 fractures. This fracture density is higher than the one observed in the EZ-B Niche (approximately a factor 10; Yong 2007 and Figure 2-4). Such high fracture density will lead to overestimated axial fluxes and underestimated resaturation times, what renders the calculations presented here a worst case scenario.

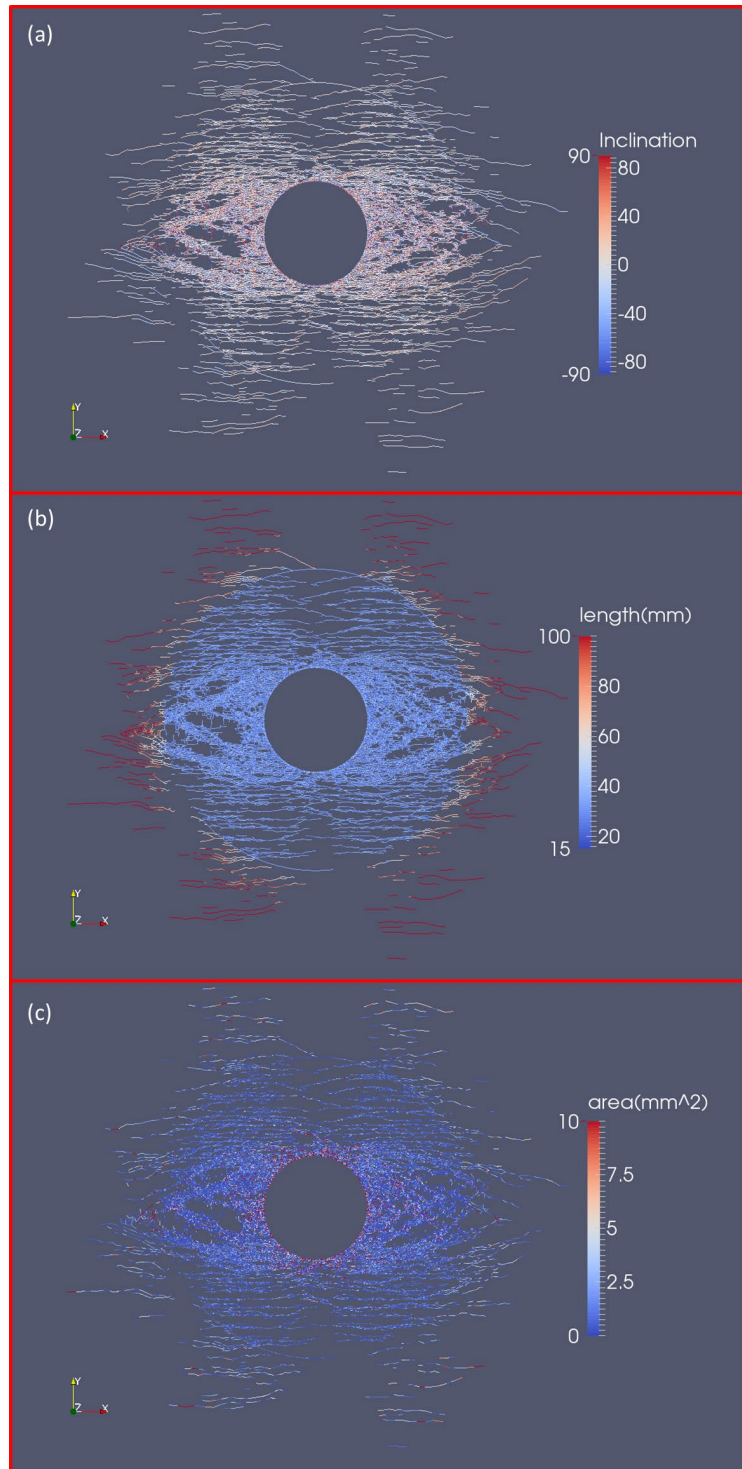


Fig. 3-6: Geometric definition of the input FEMDEM.

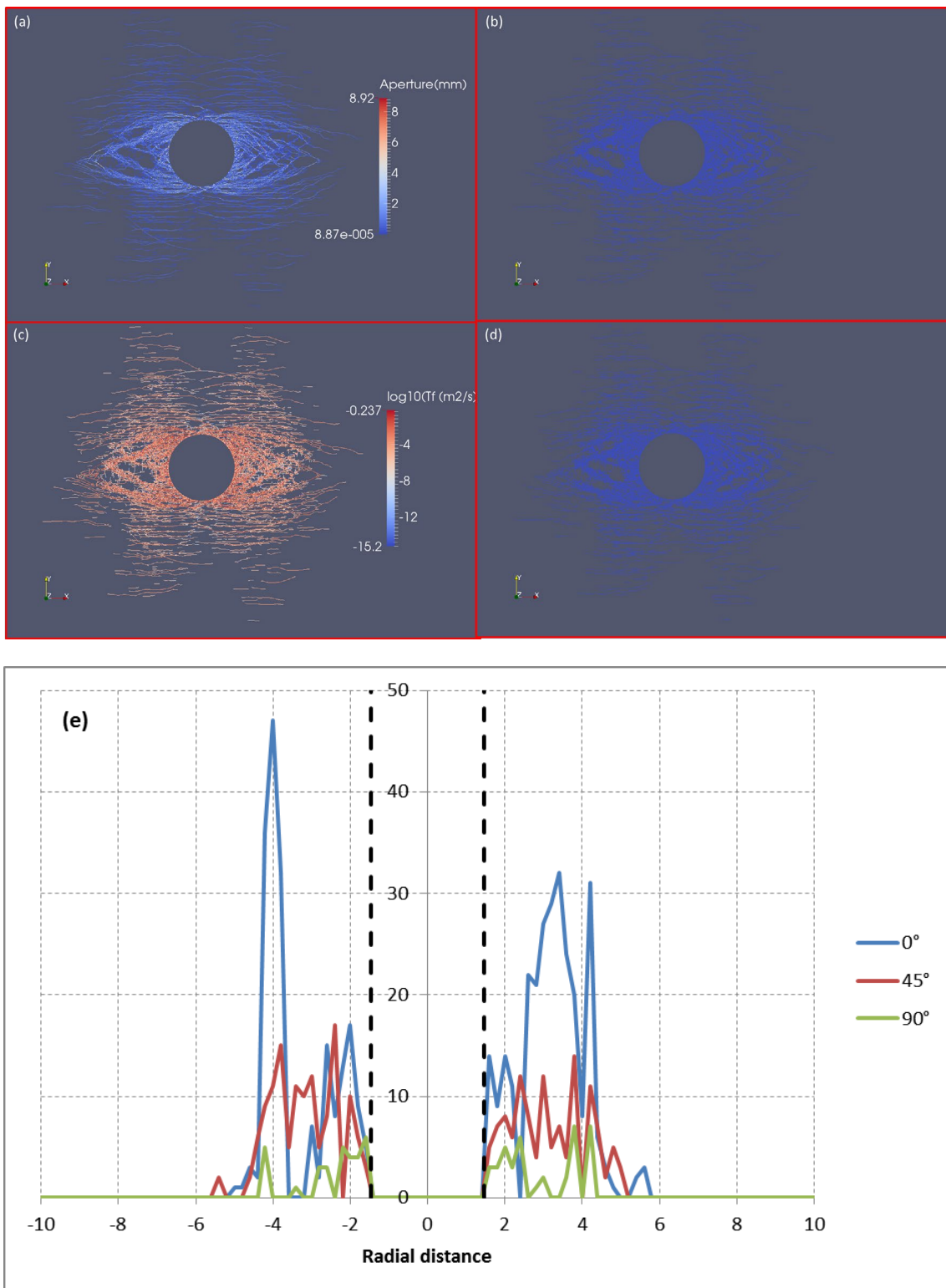


Fig. 3-7: Hydraulic definition of the input FEMDEM. Panels (a) and (b) report on initial and irreducible fracture apertures (early and late times, respectively). Panels (c) and (d) report on initial and irreducible fracture transmissivities. Panel (e) displays the number of fractures at trace lines at inclinations 0, 45 and 90° (counterclockwise from x axis). Dashed black lines depict the extension of the buffer zone.

### 3.4 Equivalent continuum model of the EDZ

The geometric and hydraulic properties of the DFN described in Chapter 3.3 are mapped onto a finite element mesh. This enables (i) the upscaling of discrete FEMDEM properties to equivalent properties of a continuum medium, (ii) the modeling of fluid flow in the EDZ and (iii) the abstraction of simplified EDZ models that will serve as input to the safety analysis.

#### 3.4.1 Mesh generation

The fluid flow caused by resaturation of the EDZ is predominantly radial due to the shapes of the EDZ and the gallery. Therefore, a radial finite element mesh is generated (Figure 3-8). An advantage of radial meshes when compared with pseudo-regular structured meshes oriented parallel to coordinate axis is that radial meshes do not suffer from artificial anisotropy in the flow simulations. A structured mesh made of square/rectangular elements with increasing element size generates very elongated elements that lead to spurious anisotropy effects in the form of preferential flow paths along the longest-edge direction of the cells. The only way to get rid of those effects while using a structured mesh is by means of a constant element size. This leads to very dense meshes for accurate models and render the flow simulations unaffordable.

Four zones with different discretization density can be distinguished. The parameters defining the cell density at each zone depend on several factors (e.g., the size of the EDZ), and are selected as a compromise between simulation accuracy and CPU time. Radial rays are thrown every 2° to keep the elements as uniform in shape as possible. Thus, each "ring" contains 180 cells. From the center and towards the boundary, the zones with different discretization densities are:

1. Bentonite: coarse mesh, with element size decreasing with radial distance (Figure 3-8c), attaining a minimum size at the contact between the bentonite and the liner. This is required due to stability issues caused by the stark contrast between the hydraulic parameters of the liner and of the bentonite.
2. Liner: the discretization density is high (Figure 3-8c) and the element size is kept approximately constant due to the high hydraulic conductivity of the liner.
3. Area encompassing the EDZ: the mesh is also refined because the EDZ is precisely the area of interest and it requires enhanced simulation accuracy (Figure 3-8b). The element size is kept approximately constant.
4. Outside the area encompassing the EDZ, the element size grows following a geometric progression (Figure 3-8a). The model spans over a circular area with radius 100 m, such that boundaries are far away from the EDZ to avoid spurious numerical effects.

For the modeling of the HAA-01 case, the mesh consists of 22'500 cells and 22'680 nodes, what leads to a good balance between solution accuracy, numerical stability and CPU time.

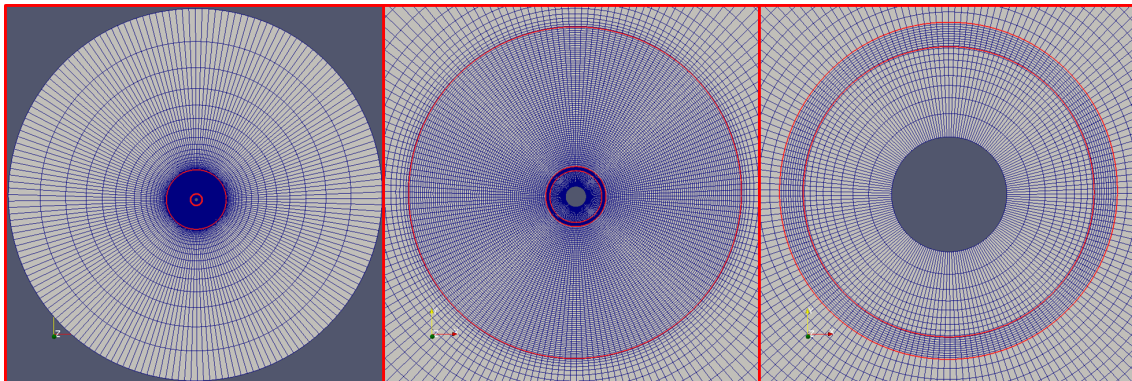


Fig. 3-8: Three zoom levels of the finite element mesh adopted in this work. From left to right: (a) overall mesh, with radius 100 m; (b) zoom at the zone of interest encompassing the EDZ; (c) zoom at the closest vicinity of the canister. The red lines encompass the input DFN (radius ~ 6-8 m in this case) and the liner. The inner circle represents the canister, with radius 0.5 m, assumed to be impervious.

Note that the mesh is not conditioned to the deformed geometry of the liner. None the less, the deformed liner is accommodated in the mesh by direct mapping. In addition, the elements at the wall-rock contact are also mapped. For an easy identification in the output files, each cell is attributed with a code that reports on material type. These codes, together with the deterministic hydraulic properties used in this study are summarized in Table 3-2. Figure 3-9 displays three zoom levels of the zonation.

Tab. 3-2: Zones of the model and deterministic values for hydraulic properties used in this study.

Zone	Cell code	Porosity	$K_{xx}$ (m/s)	$K_{zz}$ (m/s)
Intact OPA	1	0.12	$10^{-13}$	$2 \cdot 10^{-14}$
Cells intersected by fractures	2	Variable	Variable	Variable
Bentonite	3	0.35	$10^{-13}$	$10^{-13}$
Liner	4	0.20	$10^{-10}$	$10^{-10}$
Wall-rock contact	5	0.12	$10^{-13}$	$2 \cdot 10^{-14}$

Hydraulic properties at cells are calculated upon geometric properties. To that end, each cell is visited and the fractures properties intersecting the element (if any) are upscaled. The upscaling procedure is explained in detail in Chapter 3.4.2.

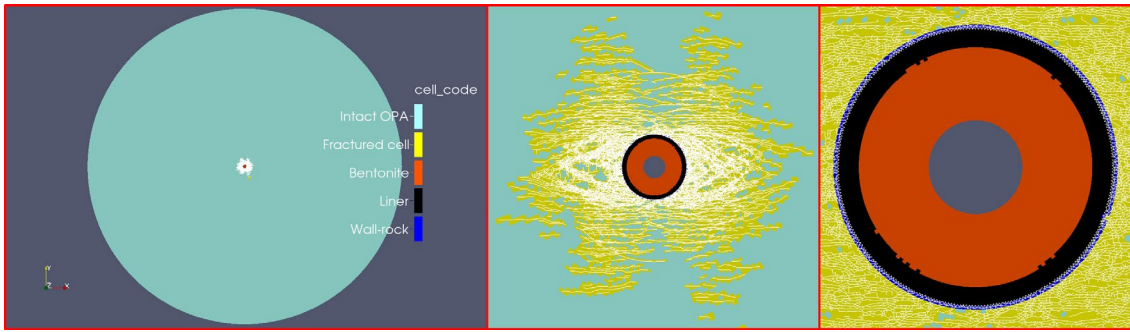


Fig. 3-9: Model zonation. From left to right: (a) Global domain. The intact OPA (light blue) predominates; (b) zoom at the scale of the EDZ (radius  $\sim 6-8$  m). In this area, a vast majority of cells are intersected by fractures (in yellow); (c) zoom at the scale of the gallery. Although some fractures intersect the wall-rock cells (blue color), these are not taken into account in the calculations because the wall-rock contact is attributed with deterministic properties (Table 3-2) regardless of the fracturation intensity. Fracture traces are highlighted in white. The central grey circle is a hole depicting the canister ( $r = 0.5$  m), assumed impervious.

### 3.4.2 Upscaling procedure: Equivalent continuum parameters

Cell porosity is calculated as:

$$\phi = \frac{V_p}{V_{tot}} = \frac{V_{pf} + \left(1 - \frac{V_{pf}}{V_{tot}}\right)V_{pm}}{V_{tot}} = \phi_f + (1 - \phi_f)\phi_m \quad (3-2)$$

$$= \phi_f(1 - \phi_m) + \phi_m$$

where  $\phi$  is total porosity,  $V_p$  and  $V_{tot}$  are volume of pores and total volume of the cell, respectively. Note that we work per unit length in the axial direction. Therefore, cell volumes are equivalent to cell areas. Subscripts 'f' and 'm' refer hereinafter to fracture and matrix, respectively. Constant deterministic values of matrix porosity of the different materials are summarized in Table 3-2. Fracture porosity of a given cell is calculated as an average of the geometric parameters defining the fractures intersecting the cell:

$$\phi_f^j = \frac{\sum_i a_i L_i^j}{V_j} \quad (3-3)$$

where  $a_i$  [L] and  $L_i^j$  [L] are the aperture and trace length of a fracture 'i' intersecting cell 'j'.  $V_j$  is the cell volume (actually, area).

Hydraulic conductivity along a certain direction is calculated as:

$$K = K_m + K_f \quad (3-4)$$

where  $K_m$  [ $LT^{-1}$ ] denotes matrix hydraulic conductivity (see Table 3-2 for constant deterministic values at selected zones) and  $K_f$  [ $LT^{-1}$ ] is fracture conductivity of cells intersected by fractures.  $K_f$  is calculated from fracture transmissivity and trace length:

$$K_f^j = \frac{\sum_i T_i L_i^j}{V_j} \quad (3-5)$$

where  $T_i$  [ $L^2T^{-1}$ ] is the transmissivity of fracture 'i' intersecting cell 'j'.

Within the cross section, the flow takes place mainly in the fracture plane and not in the orthogonal out-of-plane direction. Thus, anisotropic hydraulic conductivities are calculated from the maximum conductivity by standard projection:

$$\begin{aligned} K_{f,xx} &= K_f \cos \theta \\ K_{f,zz} &= K_f \sin \theta \end{aligned} \quad (3-6)$$

where  $\theta$  is the inclination of the fracture.

Hydraulic conductivities in  $x$  and  $z$  direction are calculated at each cell:

$$\begin{aligned} K_{xx} &= K_{f,xx} + K_{m,xx} \\ K_{zz} &= K_{f,zz} + K_{m,zz} \end{aligned} \quad (3-7)$$

Finally, cell conductivity  $K_{yy}$ , orthogonal to the cross section (i.e., parallel to the axis of the gallery) is calculated as:

$$K_{yy} = \sqrt{K_{xx} \cdot K_{zz}} \quad (3-8)$$

In Equation 3-8, we assume that the cell size is sufficiently small and that the anisotropy of hydraulic conductivity is not significant. This simplification is made towards more efficient resaturation simulations.

### 3.4.3 Initial equivalent continuum parameters

Figure 3-10 displays the mapped distributions of fracture, matrix and total porosity, as derived from the geometric properties of the FEMDEM. In this study, it is assumed that the process of excavation and emplacement is instantaneous (in the sense of its impact is not transient). As observed,  $\phi_f$  and  $\phi$  resemble well the fracture distribution at the EDZ. Initial  $\phi_m$  is piece-wise constant, with values reported in Table 3-2. The same observations become apparent from Figure 3-11, which displays the mapped distributions of hydraulic conductivity. As observed, the high fracture density leads to very high initial values of porosity and hydraulic conductivity.

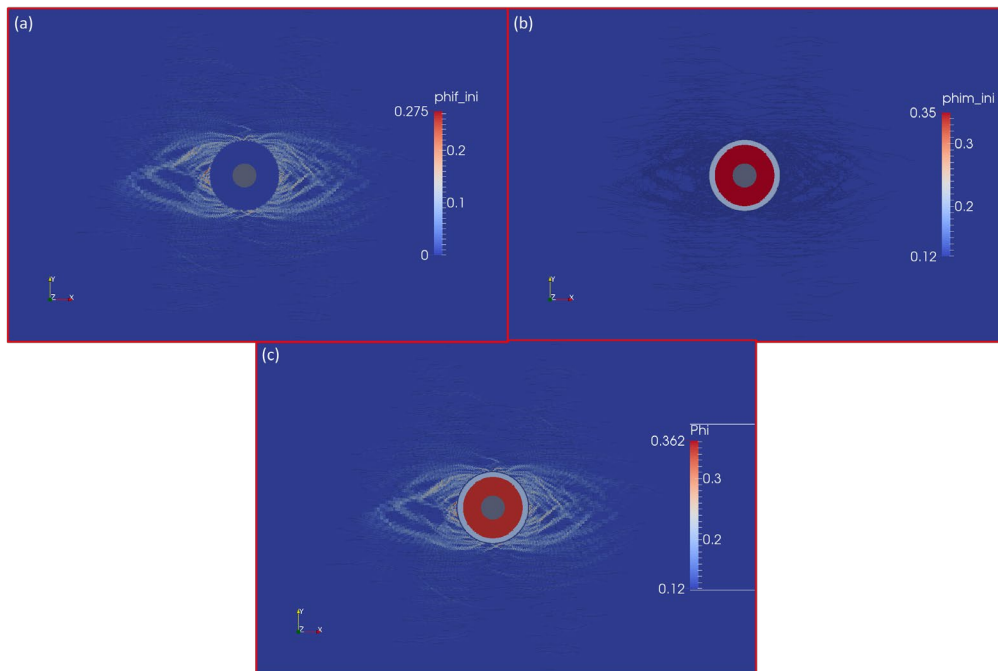


Fig. 3-10: Mapped distributions of: (a) initial fracture porosity, (b) initial matrix porosity and (c) total initial porosity. Fracture traces are depicted by shaded black lines in panel (b).

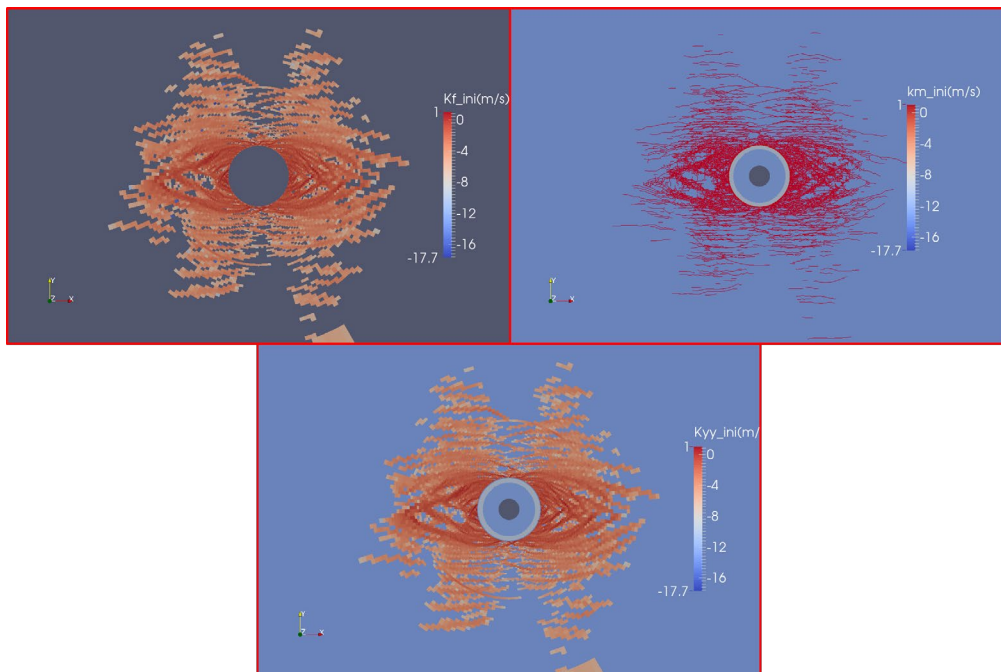


Fig. 3-11: Mapped distributions of: (a) initial fracture hydraulic conductivity, (b) initial matrix hydraulic conductivity and (c) cell conductivity in the axial direction. Fracture traces are depicted by red lines in panel (b). Dark grey color in panel (a) depicts elements not intersected by fractures. log10 distributions are plotted for clarity.

### 3.4.4 Resaturation of the system: Temporal evolution of equivalent continuum parameters

The conceptual model for the resaturation of the system has been presented in Chapter 2.2.5. Resaturation causes two effects. On the one hand, a pressure increase at the fractures from atmospheric to nearly hydrostatic pressure conditions of the formation causes a reduction of effective normal stress. This reduction leads to a mechanical fracture closure (see Equation 2-6). Fracture closure leads to a loss of fracture porosity and hydraulic conductivity, according to equations 3-3 and 3-5. On the other hand, the high percentage of clay materials makes the rock matrix to swell at low pressure variations ( $< 2$  MPa; see Figure 2-13). Swelling causes both matrix porosity and conductivity to increase with time. Early stages of the resaturation process are controlled by the high transmissivity of the many fractures defining the EDZ. This process is initially very fast, but very slow at mid and late times, when a certain degree of resaturation already took place.

Actually, the buffer zone and some fractures are initially unsaturated. A set of two-phase flow scoping simulations was carried out to address the impact of the initial unsaturated state (see Appendix B). It was observed that the saturation process of the initially unsaturated pores takes 20-50 years. This time frame is negligible compared to the total time required for the full resaturation of the system ( $> 1000$  years). Therefore, the initial unsaturated state was ignored in this study in order to render the simulations solvable in a reasonable amount of CPU time.

The resaturation process is simulated using the finite element mesh described in Chapter 3.4.1. Boundary conditions are zero drawdown (i.e., the far field does not undergo any resaturation) at the boundaries and zero flux at the inner circle representing the canister, assumed impervious. Initial condition is hydrostatic pressure (which varies in depth) at elements not intersected by fractures. At elements intersected by fractures and within the buffer zone, atmospheric pressure conditions are imposed.

A salient feature of the simulations presented here is that hydraulic parameters vary in time according to the aforementioned physical processes of mechanical closure and matrix swelling. Equations 3-2 and 3-7/3-8 can be written without loss of generality as:

$$\begin{aligned}\phi &= \phi_f(t) + (1 - \phi_f(t)) \phi_m(t) \\ K_{xx}(t) &= K_{f,xx}(t) + K_{m,xx}(t) \\ K_{zz}(t) &= K_{f,zz}(t) + K_{m,zz} \\ K_{yy}(t) &= \sqrt{K_{xx}(t) \cdot K_{zz}(t)}\end{aligned}\tag{3-9}$$

Note that it is implicitly assumed that total porosity  $\phi$  does not vary in time. This assumption can be justified by the fact that fracture porosity diminishes with time, while matrix porosity increases with time. The amount of porosity increase/reduction of each component is highly unknown at this stage and therefore it is assumed for simplicity that the two effects balance. A second assumption in Equation 3-9 is that the cell size is sufficiently small and the anisotropy of hydraulic conductivity is not significant. This allows us to calculate the axial hydraulic conductivity as the geometric mean of the components  $K_{xx}$  and  $K_{zz}$ .

Bandis et al. (1983) introduced a simple hyperbolic model for a single fracture (see Chapter 2.2.3), expressing the fracture closure (or aperture, depending on the sign criteria)  $a$  as a function of effective normal stress  $\sigma'_n$  acting over the fracture plane:

$$a(t) = a_0 - \frac{\sigma'_n(t)}{a_0 K_{n0} + \sigma'_n(t)} \quad (3-10)$$

where  $a_0$  is the initial fracture aperture (here, before the resaturation starts, immediately after excavation and emplacement) and  $K_{n0}$  is fracture normal stiffness ( $\text{ML}^{-2}\text{T}^{-2}$ ). Barton and Bandis' experiment consisted of varying effective stresses by varying the confining (total) stresses, i.e., at a constant sample pressure. Instead, we assume that total stresses in the near field are constant and that variations of effective stresses are caused simply by pressure variations during the resaturation of the system. To mimic these phenomena, we propose a modified version of Barton-Bandis' model depending on incremental pressure:

$$a(t) = a_0 - \frac{\Delta p(t)}{a_0 K_{n0} \Delta p(t)^\alpha + \Delta p(t)} \quad (3-11)$$

$K_{n0}$  is approximately 920 MPa/m (Yong et al. 2010). The exponent  $\alpha$  controls the velocity of fracture closure. Note that when  $\Delta p \rightarrow 0$ , the aperture tends to the initial one, in the absence of pressure perturbations. Figure 3-12 displays the pressure dependence of a fracture with initial aperture  $6.7 \cdot 10^{-4}$  m (mean fracture aperture) for different values of the factor  $\alpha$ . As observed, low values of  $\alpha$  lead to smaller aperture for a given value of overpressure (or of resaturation time). Correspondingly, the time required for a full resaturation of the system is smaller for small values of the exponent  $\alpha$ . One has to bear in mind that Equation 3-11 is a simple artifact (in fact, it is dimensionally incorrect) to link aperture and pressure variations. If Barton-Bandis' model is used instead (Equation 3-10), one would need anomalously high values of fracture stiffness to achieve a minimum closure of the fracture system. Future work will focus on the goodness of the suggested model.

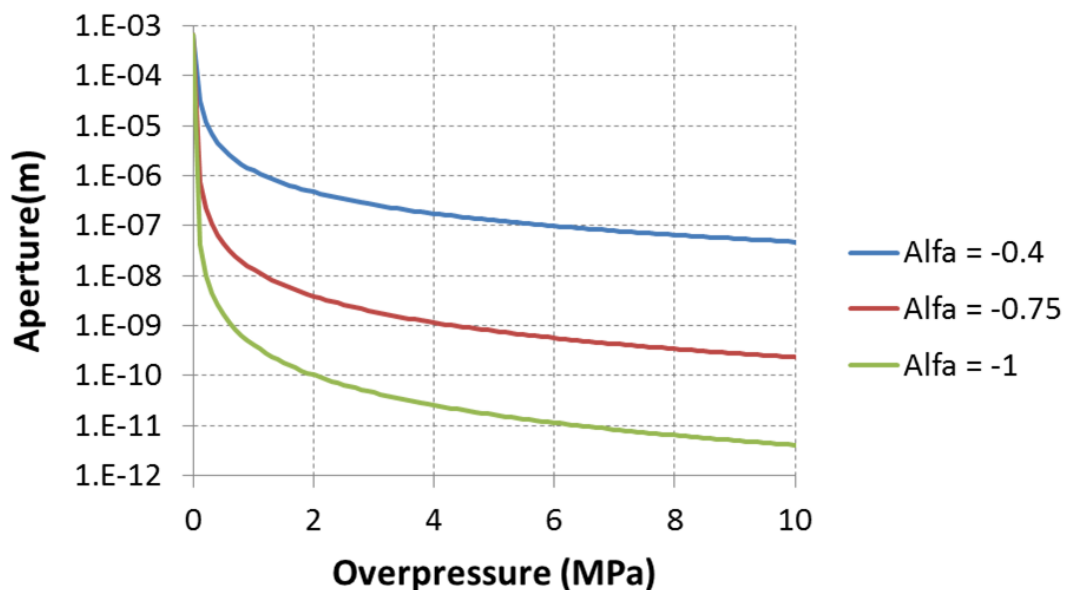


Fig. 3-12: Fracture aperture vs. overpressure (with respect to atmospheric) for different values of the exponent  $\alpha$  defining the modified Barton-Bandis' model in Equation 3-11.

At a certain time  $t$ , the spatial distribution of pressure is calculated by the flow model described above and the fracture aperture is recalculated following Equation 3-11. Fracture transmissivities are then calculated according to the cubic law in Equation 2-7. Fracture porosity and conductivity are then calculated at current time according to equations 3-3 and 3-5.

Matrix porosity  $\phi_m(t)$  is calculated from  $\phi_f(t)$  by assuming that total porosity  $\phi(t)$  is constant along the resaturation process (Equation 3-9).

Matrix porosity and conductivity are related through the well-known Kozeny-Carman law in Equation 2-4. Kozeny-Carman law is preferred over Yang and Aplin relationship (Equation 2-5) because predicted hydraulic conductivities are higher, what leads to a worst case scenario with regards to circulating fluxes and resaturation times. A simpler, less parameterized version is applied here (Horseman et al. 1996):

$$K_m(t) = \frac{\phi_m(t)^3}{(1 - \phi_m(t))^2} \cdot \frac{\rho \cdot g}{\mu} \cdot \frac{d_{10}^2}{180} \quad (3-12)$$

where  $d_{10}$  (L) is the particle size for which 10% of the soil is finer.

Our two free parameters,  $\alpha$  (the closure rate in 3-11) and  $d_{10}$  are calculated from available data.  $d_{10}$  is calculated by plugging in Equation 3-12 the pair of porosity-conductivity values of the intact Opalinus Clay in Figure 2-10, i.e.,  $\phi_m = 0.21$  and  $K_m = 10^{-12} \text{ m/s}$  (see Table 3-2), resulting  $d_{10} = 1.94 \cdot 10^{-8} \text{ m}$ . The exponent  $\alpha$  is calculated by assuming that, after full resaturation, all fractures are closed and attributed with a residual aperture  $b_r = 8.9 \cdot 10^{-8} \text{ m}$ , what corresponds to a transmissivity  $T_r = 5.7 \cdot 10^{-16} \text{ m}^2/\text{s}$ . The residual aperture is selected in such a way that, after full resaturation (i.e.,  $\Delta p \sim 7.8 \text{ MPa}$ ), the fracture hydraulic conductivity of the most conductive cell is small and similar to the matrix conductivity of the intact Opalinus Clay. This low residual transmissivity is in agreement with the results of the GS-experiment at Mont Terri (Nagra 2004; Figure 2-12). Plugging  $\Delta p$  and  $b_r$  in Equation 3-11 yields  $\alpha \sim -0.4$ .

The following figures display a few snapshots of the temporal evolution of pressure and axial hydraulic conductivity (the complete animated sequence is found in the digital appendix). Figure 3-13 displays the temporal evolution of pressure. As observed, the resaturation is very fast at early times ( $\sim 100\text{-}500$  years) but very slow after a certain partial resaturation has been attained. In fact, the system reaches at that time a pseudo-steady state. The time at which this phenomenon actually occurs is highly uncertain and, in our model, it largely depends on the exponent  $\alpha$  controlling the velocity rate of fracture closure.

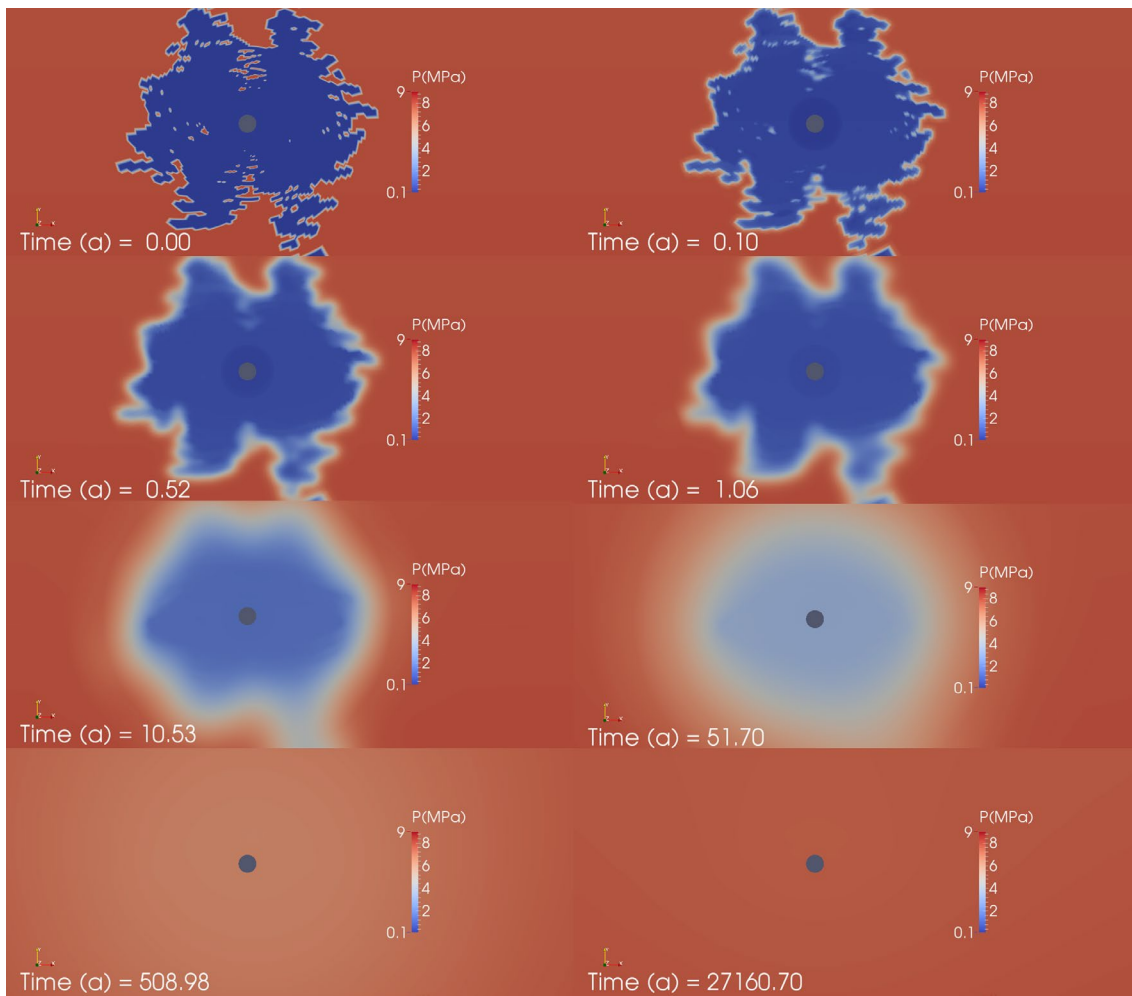


Fig. 3-13: A few snapshots of the temporal evolution of pressure.

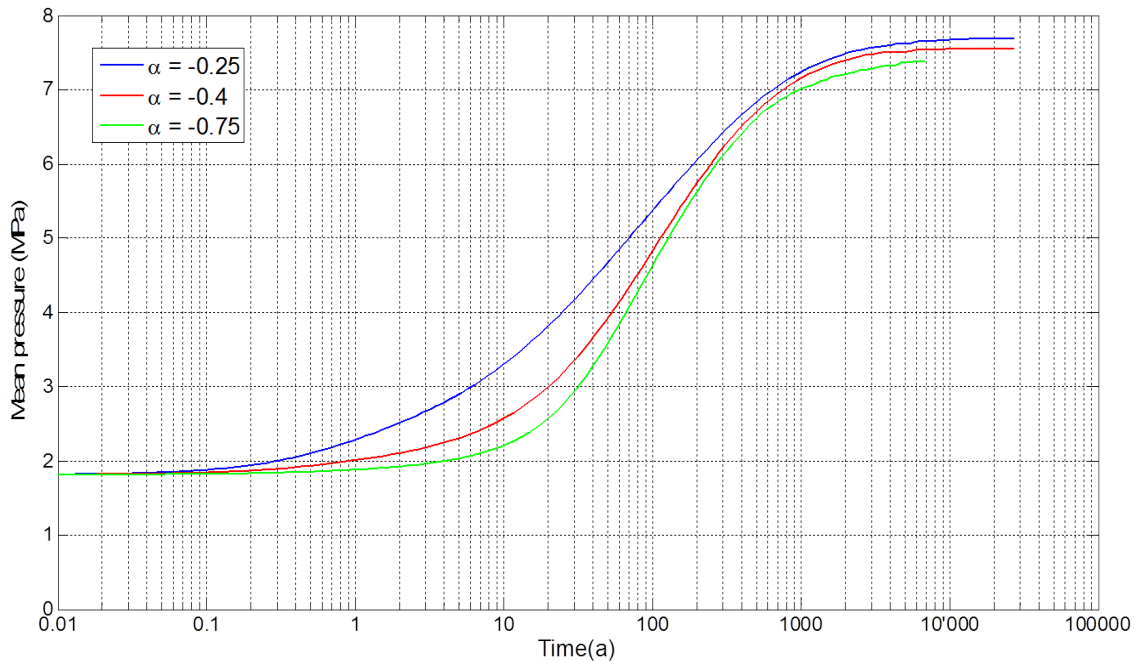


Fig. 3-14: Mean pressure as a function of time for different values of the  $\alpha$ -values defining the rate of fracture closure.

The pseudo-steady state is best observed in Figure 3-14, which displays the temporal evolution of the average pressure in the backfilled emplacement rooms. As observed, the resaturation time increases as  $\alpha$  increases. Hereinafter, we focus on the results attained with  $\alpha = -0.4$  only. Yet, three animations with different values of  $\alpha$  can be found in the digital appendix.

Figure 3-15 displays a few snapshots of the temporal evolution of hydraulic conductivity. For illustration purposes, the same scale applies to each panel. The maximum  $K$  value (i.e., that of the most conductive cell) diminishes from 9 m/s at early times after excavation and emplacement to  $7.4 \times 10^{-10}$  m/s after full resaturation of the system.

Figure 3-16 displays the number of closed fractures (i.e., attributed with the residual aperture) as a function of time. The fast hydraulic response of the system is also observed in this plot. Most fractures are closed at early resaturation times (in fact, a good portion was initially closed; see Chapter 3.4.2). This number steadily decreases with time after 1'000 years and reaches a plateau after approximately 1'000-10'000 years.

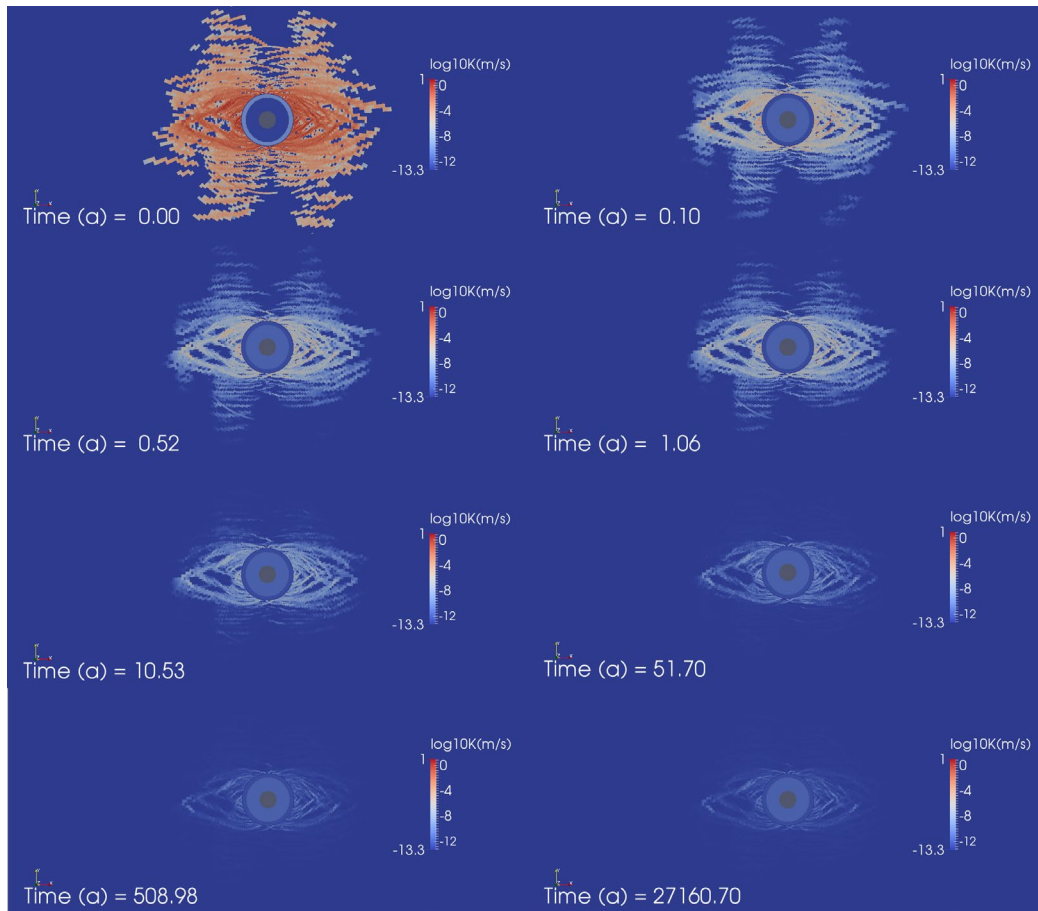


Fig. 3-15: Temporal evolution of axial (total) hydraulic conductivity. For clarity,  $\log_{10}$  distributions are displayed.

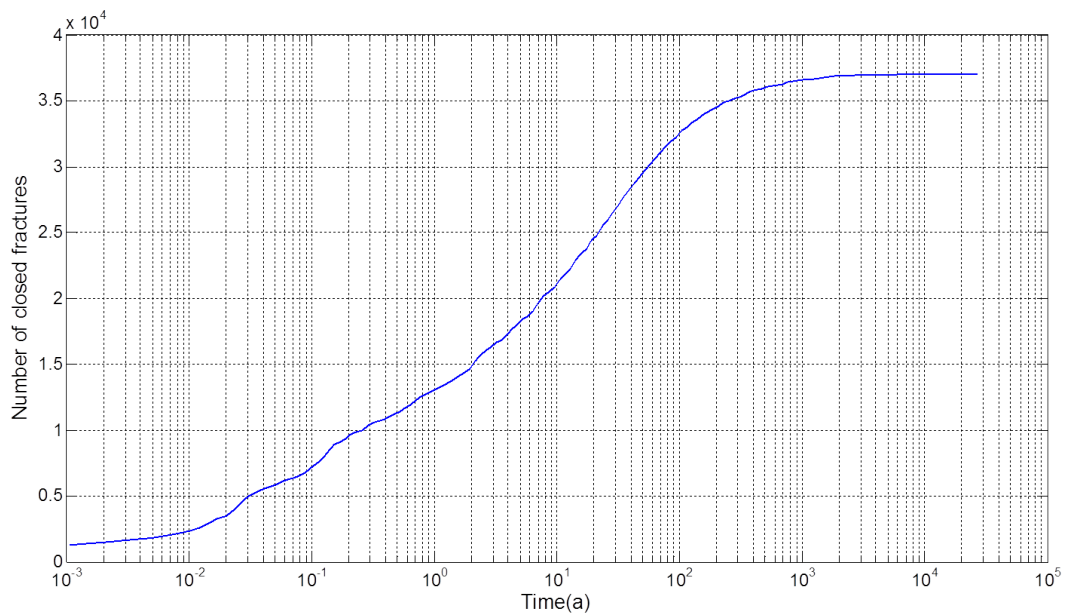


Fig. 3-16: Number of closed fractures as a function of time.

### 3.4.5 Abstraction of the EDZ

This section describes the methodology for the abstraction of the EDZ and focuses on the early and late time behaviors of the EDZ. The abstraction consists of a simple piece-wise homogeneous model including the buffer zone, the liner, the wall-rock contact, an equivalent EDZ and the intact Opalinus Clay. Each zone is attributed with constant hydraulic properties. Hydraulic properties of the EDZ are averaged over its extension. Such abstraction is amenable to the simulation of safety analysis and frees the modeler of the burden of having to deal with complex, heterogeneous, EDZ models. We consider the axial flow (i.e., parallel to the axis of the gallery) through the modeled section, calculated as:

$$Q_y(r_i) = \sum_{j \in ring, i} K_y^{i,j} A_{i,j} \quad (3-13)$$

where  $r_i$  denotes the radius of a ring 'i', 'j' is a counter of cells defining the ring,  $A_{i,j}$  is the area of the cell and  $K_y^{i,j}$  denotes axial hydraulic conductivity.  $Q_y(r_i)$  [ $L^3T^{-1}$ ] is the axial flow rate under unit hydraulic head gradient between the extremes of the gallery. To get rid of spurious effects caused by the increasing area of the rings,  $Q_y$  is standardized by the ring area, thus becoming a specific flux  $q_y$  [ $LT^{-1}$ ]. Under unit hydraulic head gradient conditions, the specific flux at a certain ring is precisely an average of the axial hydraulic conductivity. Figure 3-17 displays the specific axial flow rates at early and late times as a function of radial distance. Two figures are displayed. The left panel displays the specific axial fluxes across the elements intersected by fractures only. To that end, we have removed the matrix conductivity in 3-13:

$$Q_y(r_i) = \sum_{j \in ring, i} (K_y^{i,j} - K_{y,m}^{i,j}) A_{i,j} \quad (3-14)$$

The right panel displays the total specific flux (i.e., including the conductive feature of the matrix, as in 3-13). As observed,  $q_y$  drops at fractured elements almost 14 orders of magnitude after full resaturation of the system (13 orders of magnitude when the matrix is considered). It is expected that axial fluxes will be even smaller than the ones presented here, given that the FEMDEM simulations overestimate fracture density by a factor 5 - 10. Note that the total axial flux is already the residual one ( $\sim 10^{-13}$  m/s) approximately 6 m far away from the center of the gallery.

Porosity can also be upscaled along rings (Figure 3-18). Two observations become apparent. First, at early times, fracture porosity decays several orders of magnitude along a very small distance of 6-8 m away from the center of the gallery (i.e., the equivalent radius of the EDZ). One can also observe the piece-wise definition of matrix porosity at early times. At late times, fracture porosity is reduced  $\sim 4$  orders of magnitude due to mechanical closure. Instead, matrix porosity coincides with total porosity because all fractures are closed. In fact, there is no distinction between the red and black lines on the right panel.

The effective radius of the EDZ,  $R_{EDZ}$ , can be clearly observed in Figures 3-17 and 3-18. A way to calculate it is by simple visual inspection, i.e., the distance at which the total specific flux reaches a plateau. This is best observed in Figure 3-19 reporting on fracture density. The maximum extension of the EDZ is approximately 6 m.

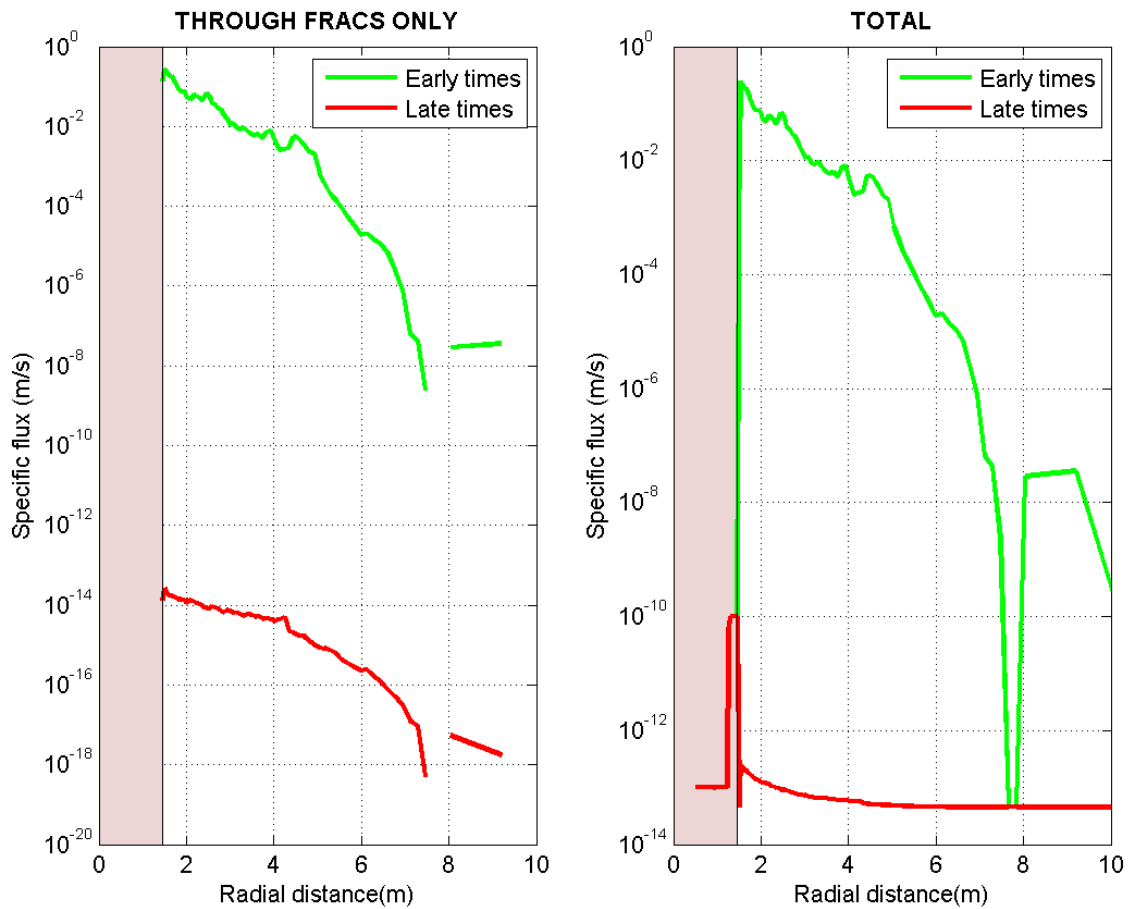


Fig. 3-17: Spatial distribution of specific axial fluxes. Left panel: fluxes across fractures only (i.e., the axial conductivity of the matrix is removed in the calculations). Right panel: total fluxes, including matrix hydraulic conductivity. The pink insets depict the buffer zone. The gap at radial distance between 7.5 and 8 m, corresponds to a disconnected fracture zone as shown in Fig. 3-11.

Hydraulic properties can now be averaged along the extension of the EDZ. In this case, the extension of the EDZ is 6.3 m (a threshold fracture density of 10 is used). The average total hydraulic conductivity is 0.039 m/s at early times and drops dramatically to values smaller than  $10^{-12}$  m/s at late times, when all fractures are closed. Equivalent porosity, which does not vary in time, is 0.14. Figure 3-20 presents a sketch of the EDZ abstraction at early and late times.

Although so far we have focused on the early and late time behavior of the EDZ, the abstraction methodology presented here can be applied at any stage of resaturation without loss of generality. Figure 3-21 displays the temporal evolution of equivalent EDZ hydraulic conductivity and of the flow rate across the abstracted EDZ. Note that the latter is simply the equivalent hydraulic conductivity multiplied by the area of the EDZ. As observed, the equivalent hydraulic conductivity of the EDZ (or equivalently, the total circulating flow rate) drops approximately 11 orders of magnitude due to mechanical closure of fractures and swelling of the clayey materials of the matrix. The late time value of equivalent hydraulic conductivity is in good agreement with experimental values obtained during the GS-experiment (Figure 2-12). Finally, Figure 3-22 reports on the temporal evolution of specific fluxes along the EDZ.

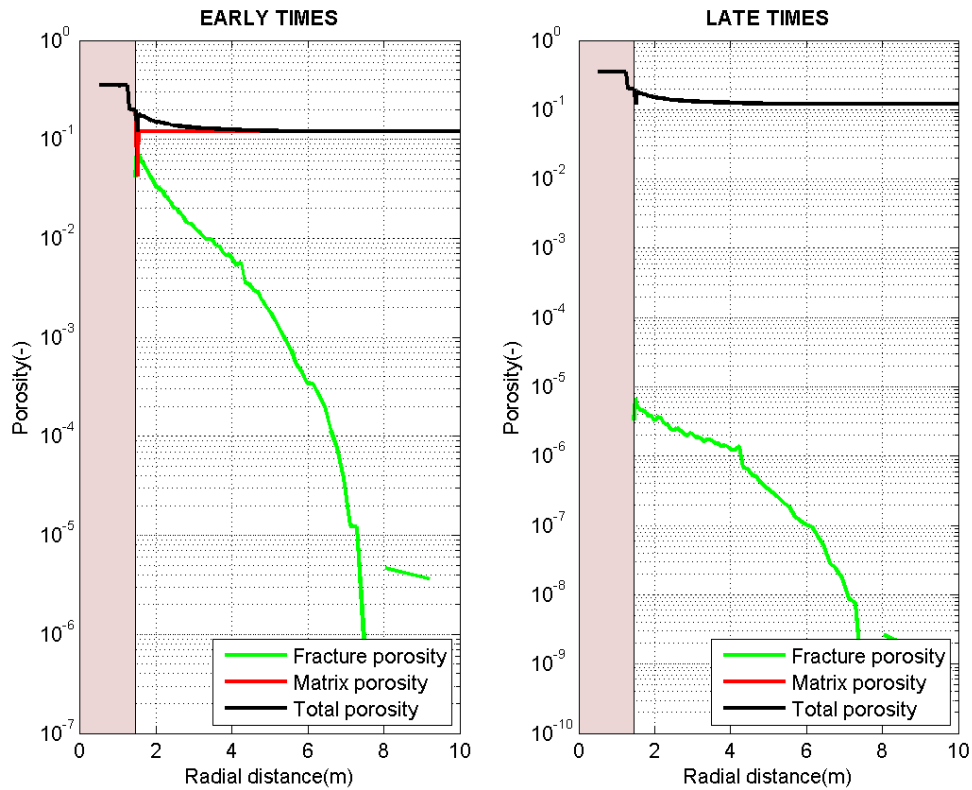


Fig. 3-18: Spatial distribution of integrated fracture matrix and total porosity at early (left panel) and late times. Note that total porosity is assumed to be constant in time. The pink insets depict the buffer zone.

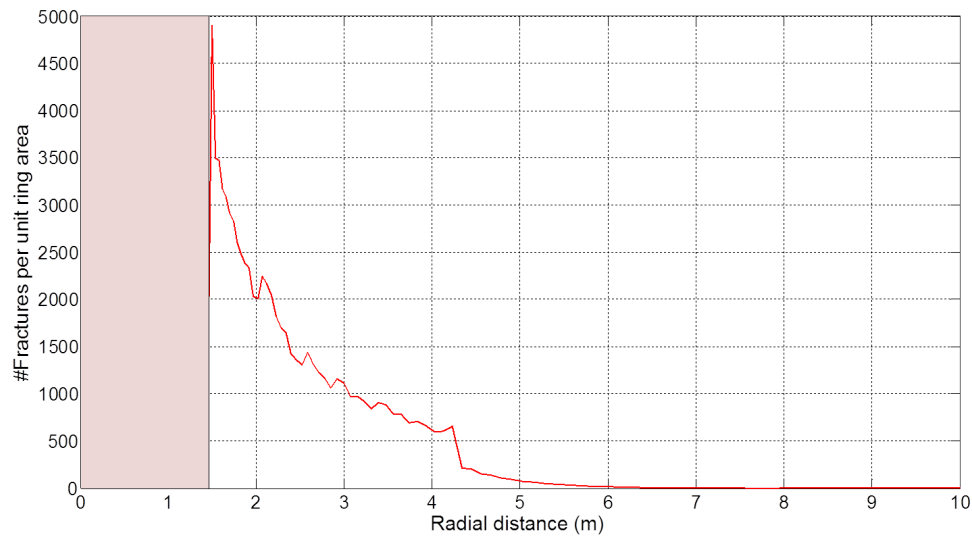


Fig. 3-19: Fracture density (number of fractures per unit ring area) vs. radial distance. The extension of the EDZ is approximately 6 m.

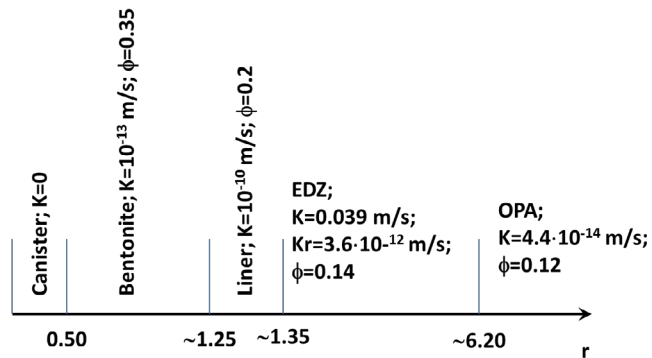


Fig. 3-20: Abstracted EDZ model, based on simulation case HAA-01. Radial distribution of equivalent hydraulic conductivity and porosity of the HAA-near-field components (cansiter, bentonite buffer, liner, EDZ, host rock). K and  $K_r$  denote hydraulic conductivity at early and late times, respectively.

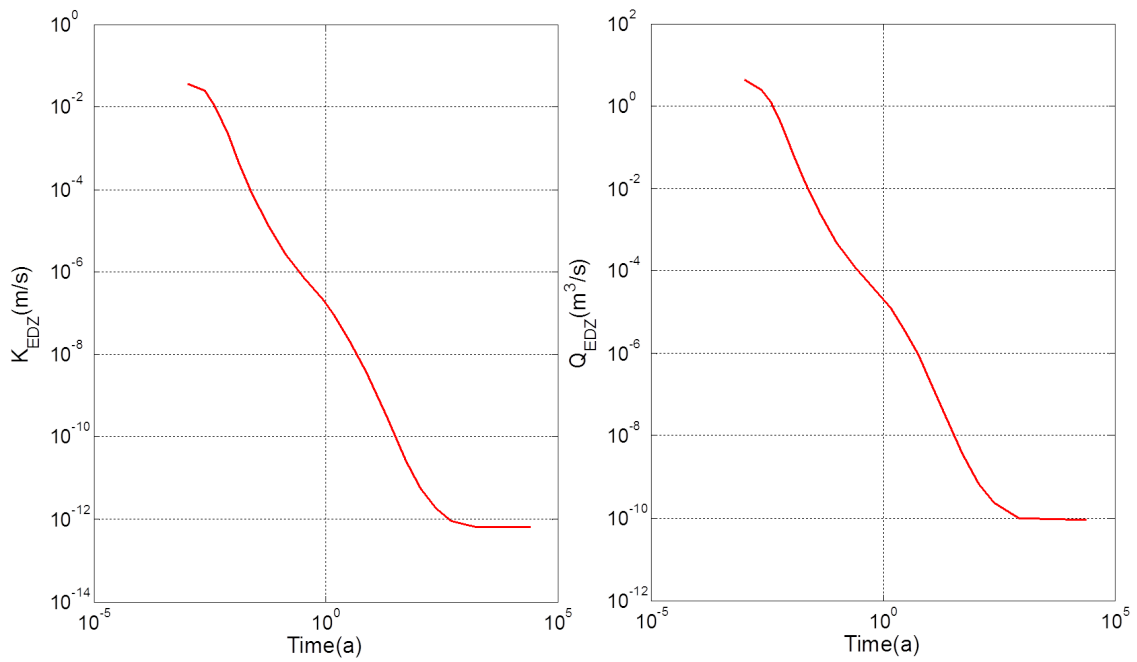


Fig. 3-21: Temporal evolution of equivalent hydraulic conductivity of the EDZ (left) and of axial flow rate across the abstracted EDZ (right).

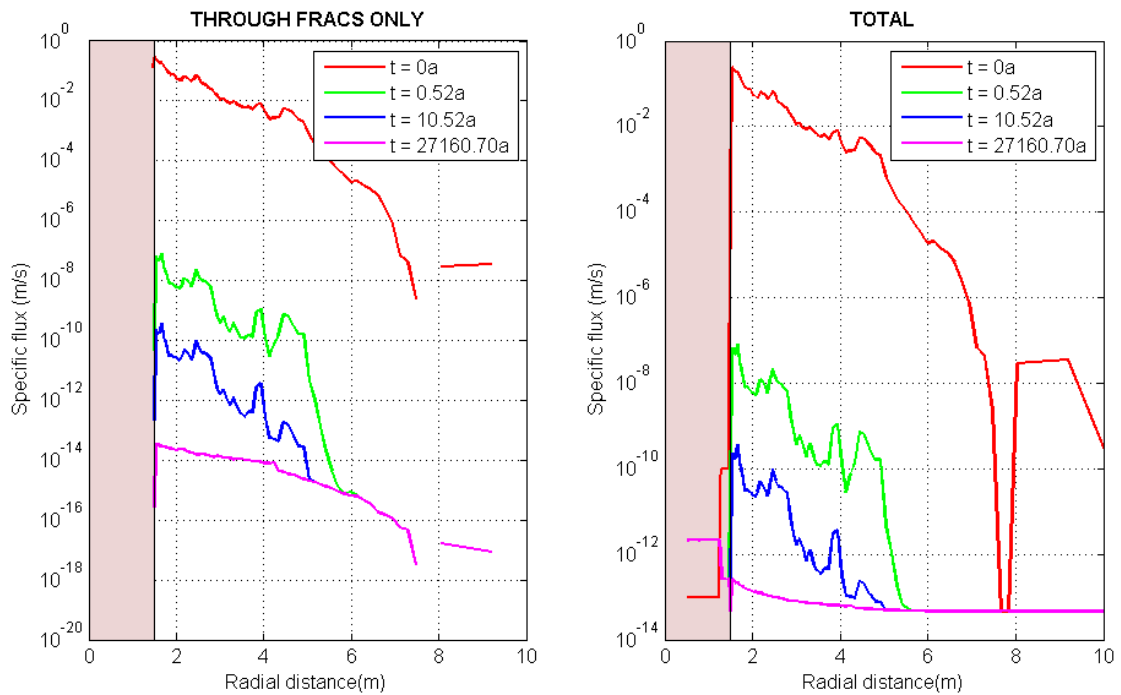


Fig. 3-22: Spatial distribution of axial fluxes at selected stages of resaturation. Note that the two end-member calculations at  $t = 0$  and  $t = 27\,160$  years are reported also in Figure 3-17.

## 4 Hydraulic properties of the EDZ – A sensitivity analysis

The EDZ around the backfilled underground structures of a geological repository represents a possible release path for dissolved and volatile radionuclides which needs to be addressed appropriately in safety assessments. The efficiency of this release path depends on the shape, extent and hydraulic properties of the EDZ.

The creation of the EDZ in response to the excavation process and its evolution in operational and post-operational times is controlled not only by engineering aspects such as the excavation method, design of tunnel support and operational regimes but also by the deformation behavior of the rock and the geological setting of the underground structures. In this context, a geomechanical sensitivity analysis was conducted to assess the extent and the shape of the EDZ around the underground structures of a geological repository for radioactive waste for a wide range of possible repository configurations in the Opalinus Clay of the candidate siting regions in Northern Switzerland (Geomechanica 2013). The geomechanical simulations provided discrete fracture networks of the EDZ around the disposal structures for a range of repository settings and the associated conceptual and parametric uncertainty:

- The geomechanical simulations were conducted for circular cross-sections (SF/HLW emplacement tunnels, shafts, seals) and for oval-shaped cross-sections (L/ILW caverns). Only the circular cross-sections are evaluated in this report, representing the EDZ release paths which are of highest significance.
- The assumed stress conditions are representative for a wide spectrum of repository settings representing repository depths of 450 m ( $\sigma_v = 11$  MPa), 650 m ( $\sigma_v = 15.9$  MPa) and 800 m ( $\sigma_v = 19.6$  MPa). The assumed stress ratios  $\sigma_v / \sigma_h$  range between 0.8 and 1.3.
- Tunnel convergence was assumed to reach values of up to 4%, which is beyond the upper limit of acceptable deformation from the engineering perspective. Simulation cases with high convergence were aimed at exploring the upper bounds of EDZ conductance to be expected in deep repository settings.
- A sequence of simulations was dedicated to the re-compaction of the EDZ of a backfilled seal section in response to the swelling pressure exerted by a bentonite buffer. Swelling pressures of 10 MPa were mimicked by the application of a radial stress on the tunnel circumference.

This chapter reports on the sensitivity analysis of the EDZ behavior with respect to its hydraulic properties in the course of the repository evolution. Chapter 4.1 contains an overview of the simulations carried out. Chapter 4.2 focuses on the simulations of the SF/HLW near-field. Chapter 4.3 reports on the EDZ simulations of a vertical shaft model. The behavior of the system under resaturation is investigated using three exemplary simulations HAA-01 to -03 and is reported in Chapter 4.4. Finally, Chapter 4.5 summarizes the main findings of the sensitivity analysis.

### 4.1 Overview of considered FEMDEM simulations

Two model geometries are considered in this study (Figure 4-1): (i) a 3.0 m diameter circular opening for the SF-HLW emplacement tunnel (HAA models hereinafter hereinafter) and (ii) a 6.0 m diameter circular opening for the vertical shaft (shaft models hereinafter). The circular gallery was placed at the center of a circular domain with 100 m radius to avoid spurious boundary effects, as discussed in Chapter 3.4.1. The cross sections of the HAA-models were assumed perpendicular to the strike of flat-lying bedding planes (i.e., HAA models are vertical

sections). Conversely, the shaft section was assumed to be oriented parallel to the bedding strike (i.e., pseudo-horizontal). The effect of the tectonic imprint on the EDZ response was investigated using 5 variants of the HAA model, in which 3 deterministic fractures dipping at  $80^\circ$  intersect the back and invert of the gallery. These deterministic fractures have 10 cm thickness and are spaced 0.5 meters.

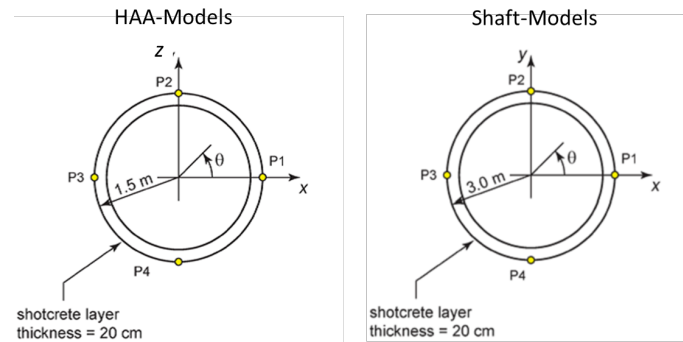


Fig. 4-1: Undeformed geometry of the HAA (left) and Shaft models (right) used in this study. Modified from Geomechanica (2013).

A total of 49 simulations have been carried out. For each simulation, we report on the following:

- Basic statistics of the geometric and hydraulic parameters defining the FEMDEM, as described in Chapter 3.2.2.
- Visual outputs of both FEMDEM and mapped (i.e., gridded) properties. Different plots for hydraulic conductivity and porosity of matrix and fractures are presented at both early times after excavation and emplacement and at late times after full resaturation of the system (i.e., all fractures closed due to mechanical effects and swelling of the clayey minerals composing the matrix).
- Spatial distribution of equivalent specific axial fluxes at early and late times (i.e., equivalent specific flux vs. radial distance). Note that, under unit head gradient across the section represented by the FEMDEM, specific axial flux is equivalent to axial hydraulic conductivity. The algorithm for upscaling hydraulic parameters is presented in detail in Chapter 3.4.2. Separate plots for the total specific flux and that at fractures only are presented.
- Spatial distribution of equivalent total, fracture and matrix porosity (see Chapter 3.4.2).
- Abstraction of the EDZ, as described in Chapter 3.4.5.

Chapter 4.2 and 4.3 report on the HAA and Shaft models respectively, and are organized as follows. First, the main conclusions after Geomechanica (2013) are listed. Following subsections focus on the sensitivity analysis to geomechanical parameters and in-situ stresses and split the results accordingly. Chapter 4.6 contains the analysis of the evaluations of the EDZ behavior under re-compaction conditions. These are presented separately due to the different nature of the boundary conditions for the geomechanical problem.

## 4.2 The SF/HLW near-field (HAA models)

The main conclusions of the study presented in Geomechanica (2013) with regard to the SF/HLW near-field are:

- The simulated ground reaction curves indicate an increase of tunnel wall displacements for decreasing values of the core softening ratio. That is, as the stiffness of the core decreases, the tunnel convergence increases.
- Displacements of larger intensity are recorded for higher in-situ stress magnitude.
- The fracture patterns are mainly characterized by shear mode of failure, with extent of the damage zone that never extends more than two tunnel diameters from the excavation boundary.
- The intensity of fragmentation varies along the excavation boundary as function of in-situ stress rotation and is generally greater in the direction perpendicular to the maximum in-situ stress.
- The sensitivity analysis to geomechanical parameters shows that as the strength parameters increase the simulated displacements decrease. This behavior is directly reflected in the EDZ extension (from about two tunnel diameters to less than about one tunnel radius).
- A three-fault system does not seem to sensibly influence the EDZ development and the tunnel deformational response. Conversely, a reduction of shotcrete stiffness causes an average increase in the tunnel displacement.

A summary of the HAA simulations is given in Table 4-1, comprising the simulation ID's, the stress state, a qualitative rock strength specification, the elastic modulus of the liner and the applied core softening ratio.

Tab. 4-1: Summary of HAA model simulations (from Geomechanica 2013).

Model Identifier	$\sigma_v$ (MPa)	$\sigma_h$ (MPa)	Strength properties	Elastic modulus of support (MPa)	Core softening ratio
<b>Sensitivity to in-situ stress conditions and core softening ratio</b>					
HAA-01	19.6	15.7	OPAx2	32	0.01
HAA-02	19.6	19.6			
HAA-03	19.6	25.5			
HAA-04	19.6	15.7			0.05
HAA-05	19.6	19.6			
HAA-06	19.6	25.5			
HAA-07	19.6	19.6			
HAA-08	15.9	20.7			
HAA-09	15.9	15.9			
<b>Sensitivity to strength parameters</b>					
HAA-10	15.9	20.7	OPAx1.5	32	0.008
HAA-11			OPAx3		
HAA-12			OPAx4		
HAA-13			OPAx5		
<b>Sensitivity to the presence of faults</b>					
HAA-14	19.6	19.6	OPAx2	32	0.01
HAA-15			OPAx1.5		0.008
HAA-16			OPAx3		
HAA-17			OPAx4		
HAA-18			OPAx5		
<b>Sensitivity to shotcrete stiffness</b>					
HAA-19	15.9	20.7	OPAx2	16	0.008
HAA-20			OPAx2	3.2	
HAA-21			OPAx1.5		
HAA-22			OPAx3		
HAA-23			OPAx4		
HAA-24			OPAx5		
<b>Re-compaction</b>					
HAA-Rec1	19.6	19.6	OPAx2	32	0.008
HAA-Rec2	15.9	20.7	OPAx2		
HAA-Rec3	19.6	15.7	OPAx2		
HAA-Rec4	19.6	25.5	OPAx2		
HAA-Rec5	15.9	20.7	OPAx3		
HAA-Rec6	15.9	20.7	OPAx1.5		
HAA-Rec7	15.9	20.7	OPAx2		
HAA-Rec8	15.9	20.7	OPAx3		

#### 4.2.1 Model simulations and overall observations

Table 4-2 summarizes the averages of the geometric and hydraulic parameters defining the input FEMDEMs. Firstly, it becomes apparent that the FEMDEMs are made of a large number of fracture patches. As commented in Chapter 3.3.2, the FEMDEM simulations overestimate fracture density by a factor  $\sim 10$ . Such high fracture density leads to overestimated axial fluxes and underestimated resaturation times, what renders the calculations presented here a worst case scenario. Secondly, the mean geometric scores of inclination, length, aperture and area are quite uniform, regardless of in situ stresses, overburden conditions, etc. For instance, the average inclination is horizontal (but with a high spread; Figure 3-5). Mean length and aperture are also quite uniform. This effect will also be observed in the uniformity of results with regards to axial fluxes.

Tab. 4-2: Geometric and hydraulic properties defining the input HAA FEMDEM simulations. Columns 3 to 7 are average values. Thick horizontal lines split the sub-groups in Table 4-1. Results under re-compaction conditions are presented separately in Chapter 4.6.

Model	Number of fractures	Aperture (mm)	Length (mm)	Inclination (rad)	Area (mm <sup>2</sup> )	log <sub>10</sub> T (m <sup>2</sup> /s)
HAA-01	43058	0.40	31.50	-0.33	0.62	-4.28
HAA-02	46366	0.40	31.50	-0.17	0.68	-4.28
HAA-03	55543	0.43	31.48	-0.17	0.70	-4.19
HAA-04	22419	0.30	31.61	-0.35	0.51	-4.66
HAA-05	25237	0.31	31.56	-0.17	0.55	-4.62
HAA-06	34891	0.36	31.50	-0.17	0.61	-4.43
HAA-07	50411	0.41	31.44	-0.16	0.67	-4.26
HAA-08	42331	0.41	31.47	0.20	0.77	-4.24
HAA-09	36658	0.45	31.44	0.00	0.90	-4.11
HAA-10	62413	0.37	31.52	0.00	0.66	-4.38
HAA-11	18492	0.51	31.43	0.09	0.96	-3.96
HAA-12	6697	0.68	31.63	0.16	1.16	-3.59
HAA-13	3363	0.84	31.70	0.43	1.45	-3.32
HAA-14	56057	0.40	31.49	0.38	0.65	-4.28
HAA-15	85324	0.38	31.51	0.49	0.58	-4.34
HAA-16	25671	0.43	31.69	0.80	0.75	-4.20
HAA-17	15037	0.45	32.00	1.25	0.74	-4.12
HAA-18	9724	0.41	32.32	2.56	0.69	-4.26
HAA-19	42376	0.41	31.47	0.20	0.77	-4.24
HAA-20	43260	0.45	31.46	0.19	0.82	-4.13
HAA-21	65376	0.40	31.52	0.00	0.69	-4.27
HAA-22	19994	0.55	31.41	0.00	1.03	-3.86
HAA-23	7378	0.71	31.56	0.00	1.21	-3.54
HAA-24	3487	0.85	31.65	0.42	1.54	-3.30

Figure 4-2 presents the spatial distribution of fracture density (i.e., number of fractures per unit area). This score is useful for the definition of the extension of the EDZ. The number of fractures at short radial distances, i.e., close to the liner, depends greatly on stress conditions and strength parameters under which the FEMDEM was generated. However, a characteristic common to all FEMDEMs is that fracture density drops dramatically to almost negligible values after a radial distance  $\sim 4.25$  m (radial distances are always measured with respect to the center of the gallery). The total extension of the EDZ (i.e., zero fracture density) is almost the same for all FEMDEMs,  $\sim 8$  m. As a conclusion, the development and geometry of the EDZ greatly depends on in situ stress conditions and strength parameters. Conversely, the extension of the EDZ for the HAA models is not sensitive to local conditions like the presence of faults. This conclusion was also reported in Geomechanica (2013).

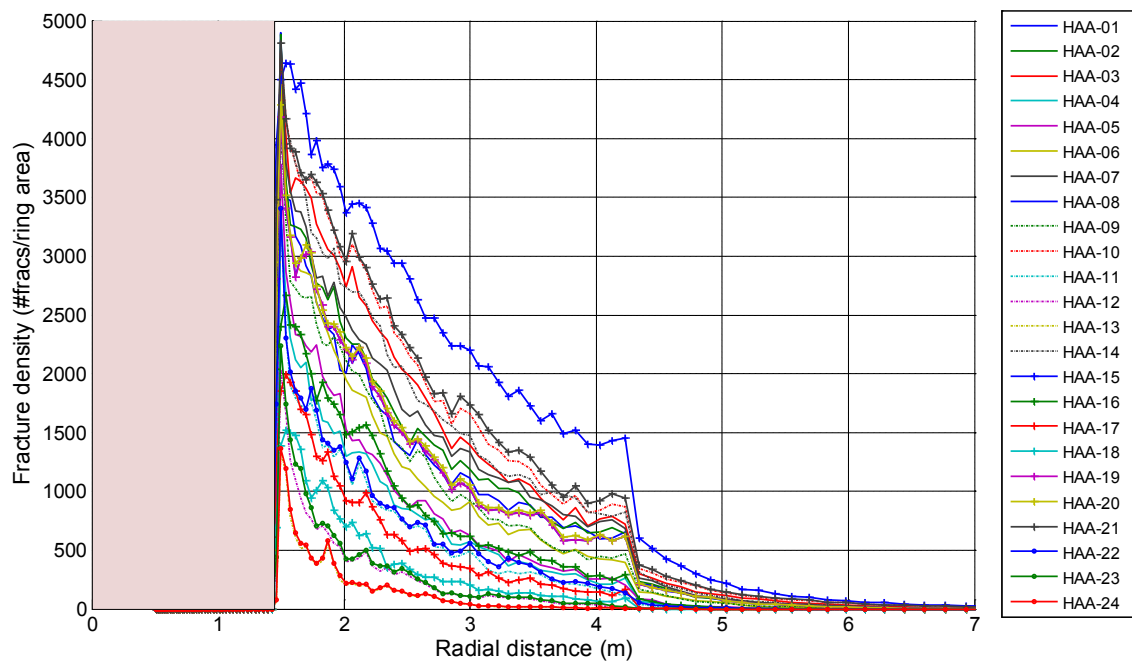


Fig. 4-2: Spatial distribution of equivalent fracture density (number of fractures on a ring of elements standardized by the ring area) of HAA models. The pink inset depicts the buffer zone.

The same conclusions can be observed in Figures 4-3 and 4-4, which summarize calculated total specific axial fluxes (equivalently, axial hydraulic conductivities) and fracture porosity respectively. Regardless of in situ stress conditions and strength parameters, we observe:

- At early times (Figure 4-3a), specific fluxes are very high ( $10^{-2}$  to  $10^0$  m/s) due to the high transmissivity of the system (in average  $10^{-4}$  m<sup>2</sup>/s; Table 4-2).
- At late times (Figure 4-3b), the resaturation of the system and the swelling of the clayey minerals of the matrix cause fractures to close. Consequently, the equivalent transmissivity of the system drops dramatically to an irreducible value  $5.7 \cdot 10^{-16}$  m<sup>2</sup>/s (assumed value). This causes the specific flux to drop more than 13 orders of magnitude. It is worth to remark that the estimations presented here overestimate fluxes because fracture density is overestimated by a factor 10. As such, actual fluxes parallel to the gallery are expected to be even smaller than the ones calculated here.

- Overall, the spread of the specific fluxes is about 1 order of magnitude at late times. Thus, specific flux is somewhat sensitive to in situ stress and strength parameters.
- All simulations yield an EDZ extension of 6 to 8 m (radial distance to the center of the gallery). Thus, the total extension of the EDZ is not too sensitive to local conditions. It is worth to mention that the effective extension of the EDZ, through which the main contribution of the axial flux circulates, strongly depends on local conditions. This is observed in the spread of specific fluxes at radial distances between 2 and 4 meters.
- Initial fracture porosity (Figure 4-4a) is very high, with values up to 0.12 (or 12%). This is due not only to the wide initial aperture of the fractures, but also due to the long length (32 mm in average; Table 4-2). Never the less, fracture porosity drops to negligible values of  $\sim 10^{-6}$  when all fractures are closed. It is worth to mention that, although fracture aperture is set to a constant irreducible value, porosity at late times is not constant, as it also depends on fracture length (Equation 3-3).

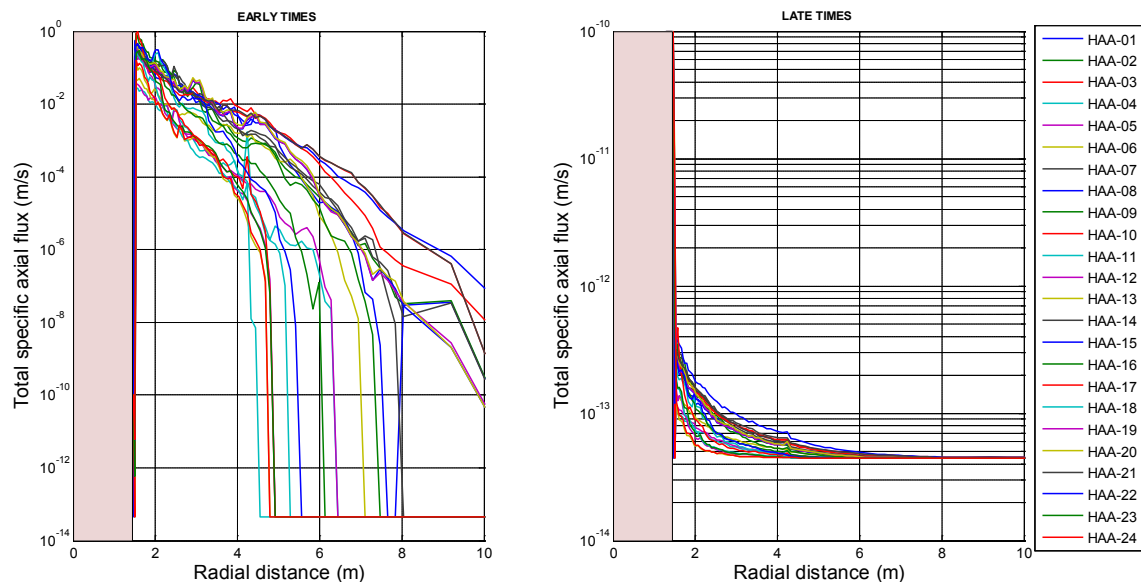


Fig. 4-3: Spatial distribution of total equivalent specific axial fluxes of HAA models. The pink inset depicts the buffer zone. On the left, early time behavior, after excavation and emplacement. On the right, late time behavior, after full resaturation of the system (i.e., assuming that all fractures are closed).

Figure 4-5 displays matrix porosity at early and late times. As observed, matrix porosity is piece-wise constant (deterministic values are summarized in Table 3-2) at early times and increases at the area encompassed by the EDZ due to the swelling of the clayey minerals. Note that the distribution of total porosity is that of matrix porosity at late times (Figure 4-5b), because it is assumed that all fractures are closed.

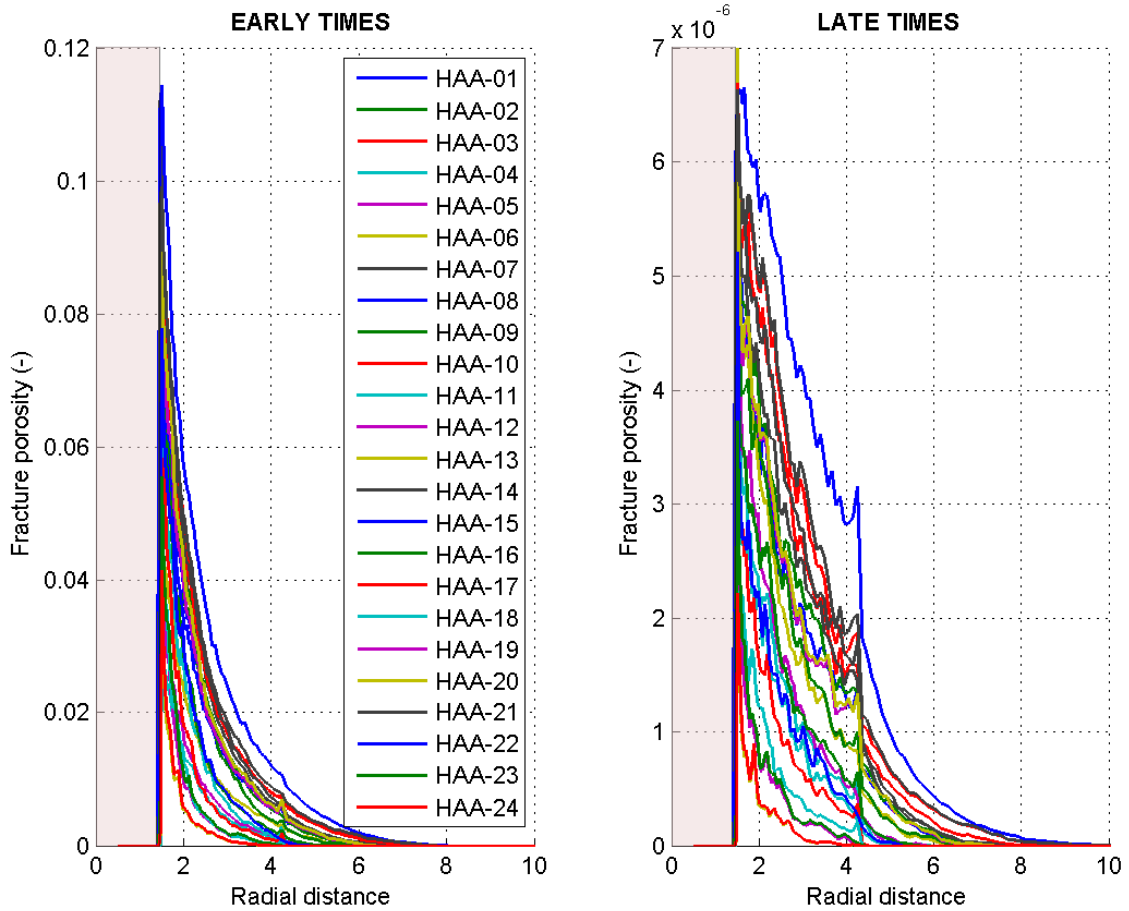


Fig. 4-4: Spatial distribution of fracture porosity of HAA models. The pink inset depicts the buffer zone. On the left, early time behavior, after excavation and emplacement. On the right, late time behavior, after full resaturation of the system (i.e., when all fractures are closed).

Figures 4-6 to 4-8 report on the abstractions of the EDZ (see Chapter 3.4.5). Figure 4-6 depicts an equivalent EDZ radius at which fracture density is approximately 10 fractures/m<sup>2</sup>. As observed, the effective extent of the EDZ depends greatly on local conditions of in-situ stresses and strength parameters. Yet, most abstracted EDZ yield equivalent radius of 6 to 8 meters. This result is coherent with that of Geomechanics (2013). Figure 4-7 summarizes the total equivalent specific axial fluxes of the EDZs abstracted with the radii in Figure 4-6. As observed, local conditions and strength parameters have some impact on the early time fluxes (specially the core softening ratio; see simulations HAA-01 to HAA-06). The same conclusion arises from Figure 4-8, reporting on total equivalent porosity. However, local conditions and strength parameters have little impact on the late time specific fluxes. Note that the abstracted specific flux drops app. 10 orders of magnitude in all cases. Finally, total porosity is not much sensitive to local conditions and strength parameters (Figure 4-8).

So far, we have analyzed all HAA simulations altogether to shed light on the global behavior and to detect some trends of the sensitivity to local conditions of in situ stresses and strength parameters. Next section is devoted to the analysis of the sensitivities of the near field behavior to variations in a specific parameter. Chapter 4.6 will summarize the results of EDZs under re-compaction conditions.

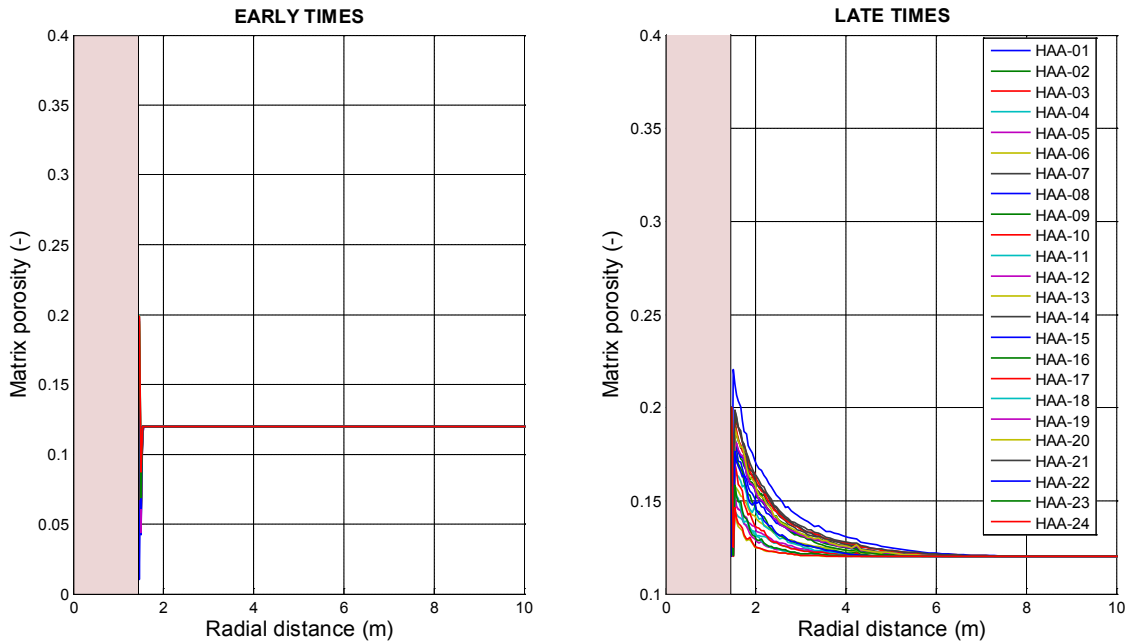


Fig. 4-5: Spatial distribution of matrix porosity of HAA models. The pink inset depicts the buffer zone. On the left, early time behavior, after excavation and emplacement. On the right, late time behavior, after full resaturation of the system (i.e., assuming that all fractures are closed). Note that matrix porosity represents total porosity at late times.

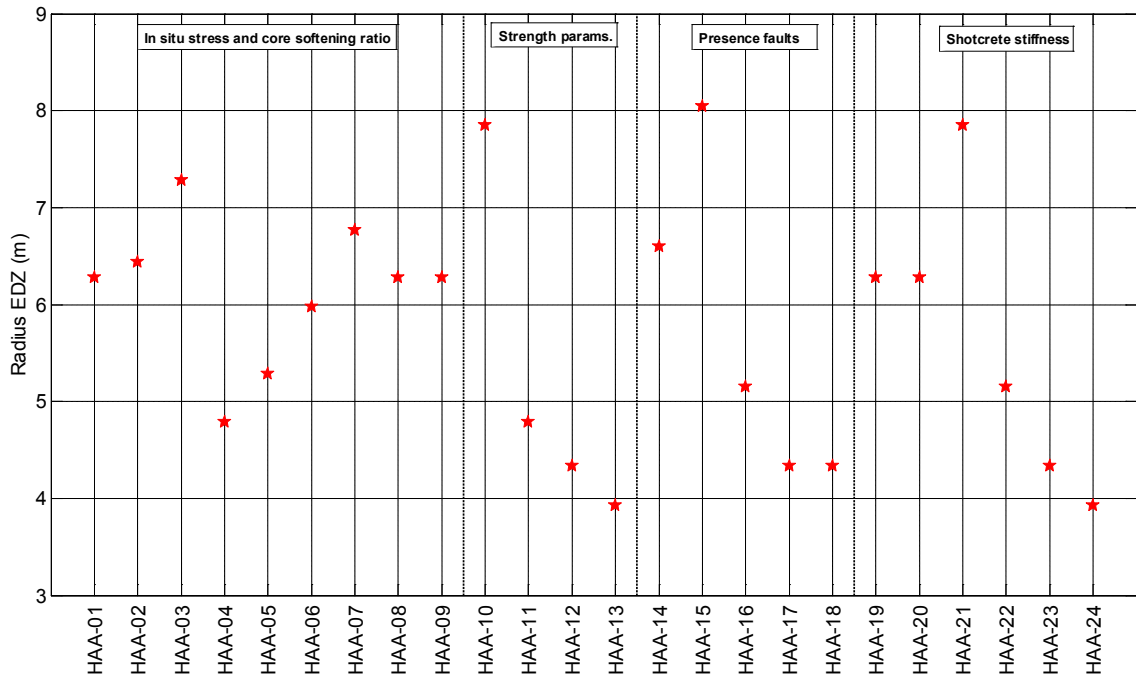


Fig. 4-6: Equivalent radius of the EDZ abstraction of HAA models, defined as the radial distance at which fracture density drops to 10 fractures/m<sup>2</sup>. Textboxes and vertical dashed lines depict the different groups of simulations in Table 4-2.

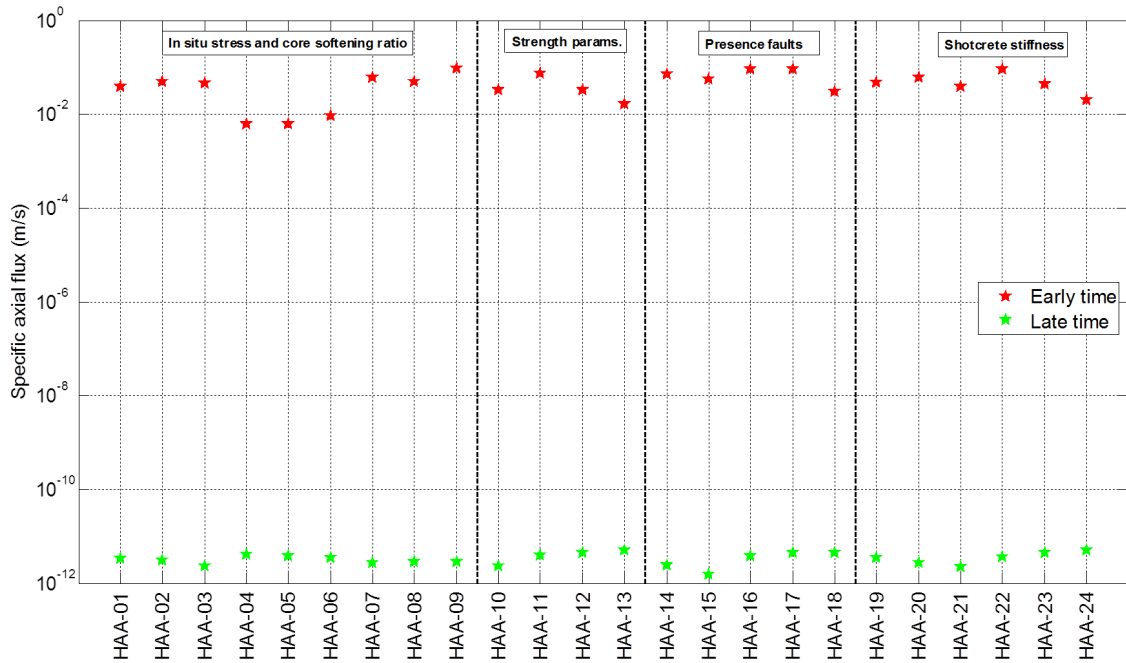


Fig. 4-7: Early and late time total equivalent specific fluxes of the abstracted HAA models.

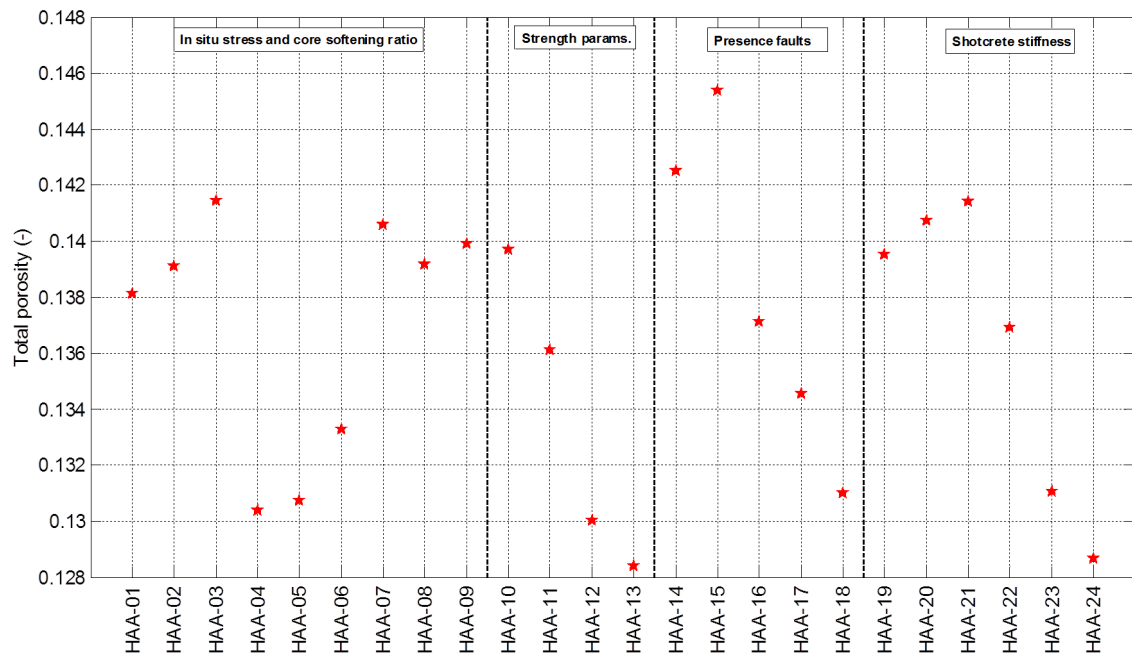


Fig. 4-8: Total equivalent porosity of the abstracted HAA models.

### 4.2.2 Sensitivity analysis

The sensitivity analysis to 5 different parameters is presented. Note that Table 4-1 mixes parameters in several groups. A major effort is made to re-group simulations sharing all parameters but just one. Five new groups are made, according to the parameter whose sensitivity is analyzed:

- in-situ stress conditions and core softening ratio: two subgroups are considered, HAA-01 to HAA-03 (with core softening ratio  $\alpha = 0.01$ ) and HAA-04 to HAA-06 ( $\alpha = 0.05$ ).
- strength parameters: two subgroups with common stress state  $\sigma_v = 15.9$ ,  $\sigma_h = 20.7$  MPa and  $\alpha = 0.008$ , (1) HAA-10 to HAA-13 (with elastic modulus of support  $E = 32$  MPa) and (2) HAA-21 to HAA-24 ( $E = 3.2$  MPa).
- elastic modulus of support: the aforementioned two subgroups but considered alternatively, i.e., HAA-10 with HAA-21, etc.
- presence of faults: we address the impact of the presence of faults by comparing simulations HAA-16 to HAA-18 with HAA-11 to HAA-13. These simulations share all parameters and only differ in the presence/absence of pre-existent faults.
- re-compaction conditions are presented in Chapter 4.6.

The remainder of this section is organized accordingly. Each subsection contains similar figures depicting (i) the spatial distribution of total equivalent specific axial flux (equivalently, of hydraulic conductivity) at early and late times and (ii) the spatial distribution of equivalent total porosity at those times. A table summarizes the abstracted models of the EDZ, in terms of radius and equivalent parameters.

### **Sensitivity to in-situ stress conditions and core softening ratio**

Two groups of simulations are compared: HAA-01 to HAA-03 (with core softening ratio 0.01) and HAA-04 to HAA-06 (0.05). The two groups share a vertical stress of 19.6 MPa and increase the horizontal stress (15.7 MPa for HAA-01 and HAA-04; 19.6 MPa –isotropic stress regime– for HAA-02 and HAA-05; 25.5 MPa for HAA-03 and HAA-06). Figures 4-9 and 4-10 report on fracture density and total axial fluxes respectively. Two observations become apparent from these figures. First, regardless of the core softening ratio, fracture density increases with horizontal stress, what leads to increased fluxes. Second, regardless of confining stresses, as the stiffness of the core increases, fracture density decrease. This leads to reduced fluxes. The same conclusions can be observed in the abstractions of the EDZ (Figures 4-6 to 4-8). These observations are coherent with those in Geomechanica (2013).

### **Sensitivity to strength parameters and elastic modulus of support**

Two groups of simulations are compared: HAA-10 to HAA-13 (with elastic modulus 32 MPa) and HAA-21 to HAA-24 (elastic modulus 3.2 MPa). The two groups share a stress regime  $\sigma_v = 19.6$  and  $\sigma_h = 20.7$  MPa. Figures 4-11 and 4-12 report on fracture density and total axial fluxes respectively. Two observations become apparent from these figures. First, regardless of the elastic modulus of support, fracture density decreases with increasing strength parameters, what leads to reduced fluxes. Second, fracture density is not much sensitive to the modulus of support under equal conditions of strength parameters and specific axial fluxes are similar in such case. The same conclusions can be observed in the abstractions of the EDZ (Figures 4-6 to 4-8) and in the previous study by Geomechanica (2013).

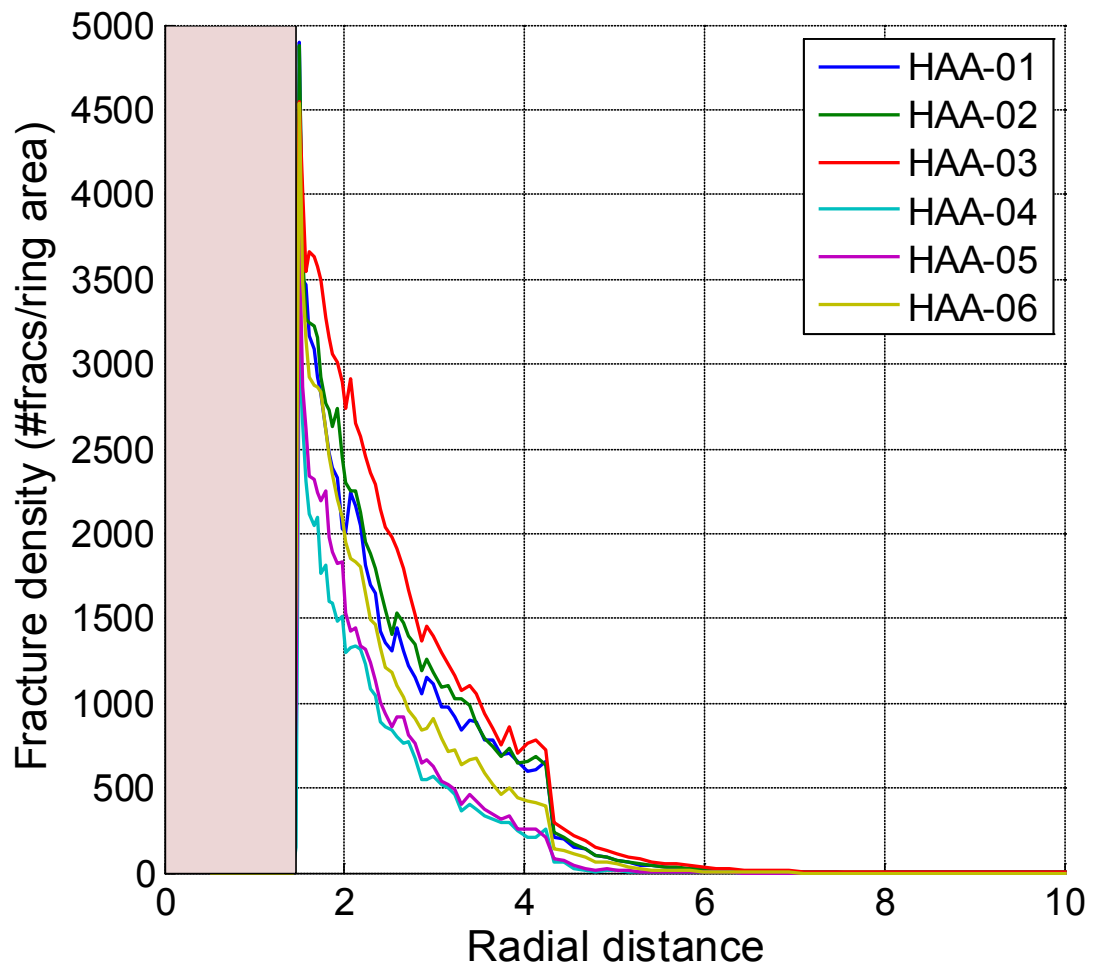


Fig. 4-9: Fracture density depending on in situ stress conditions and core softening ratio. HAA models.

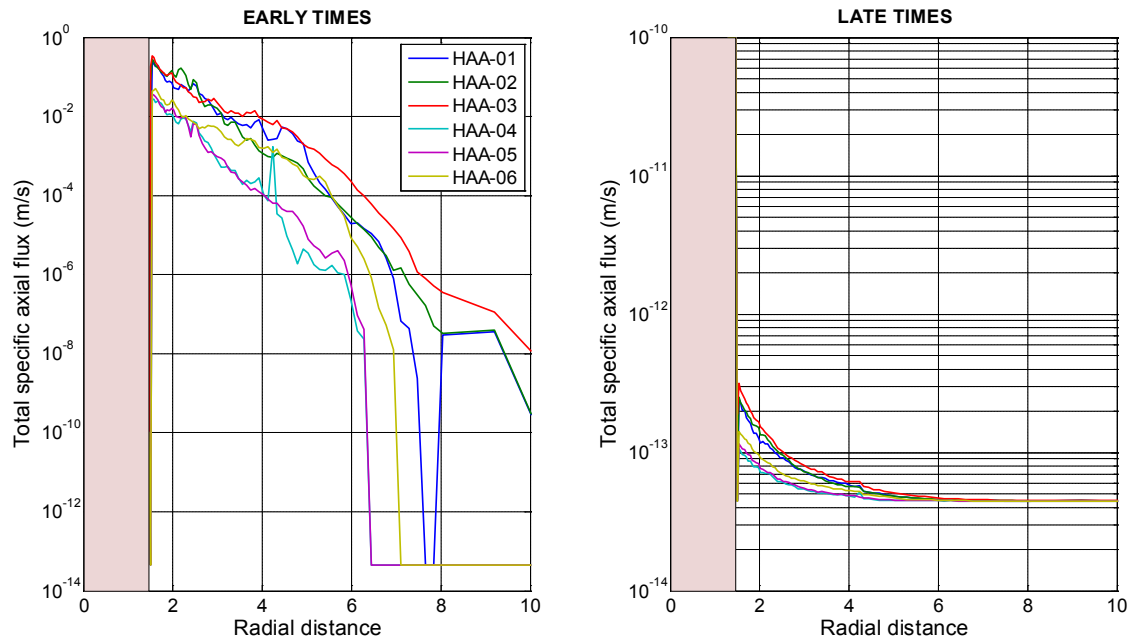


Fig. 4-10: Total axial fluxes at early (left) and late times (right) depending on in situ stress conditions and core softening ratio. HAA models.

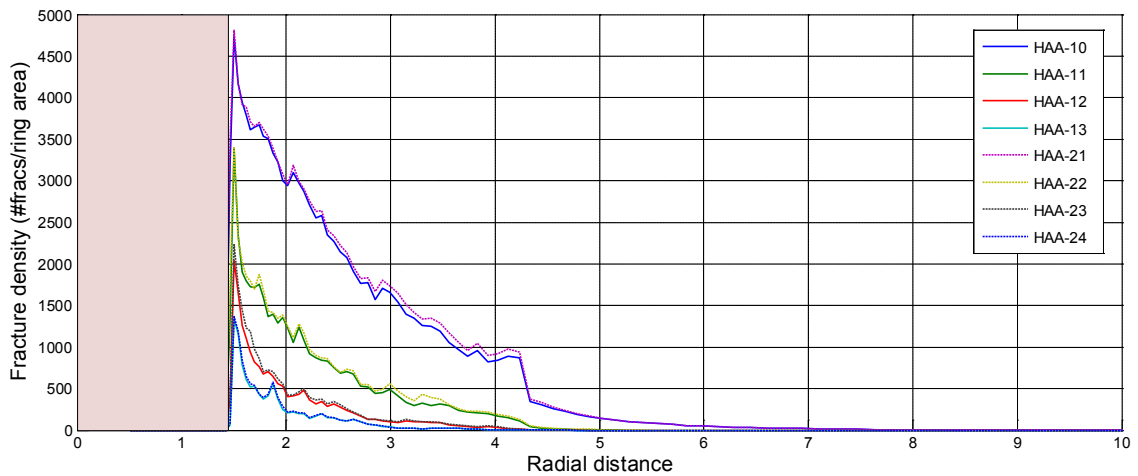


Fig. 4-11: Fracture density depending on strength parameters and elastic modulus of support. HAA models.

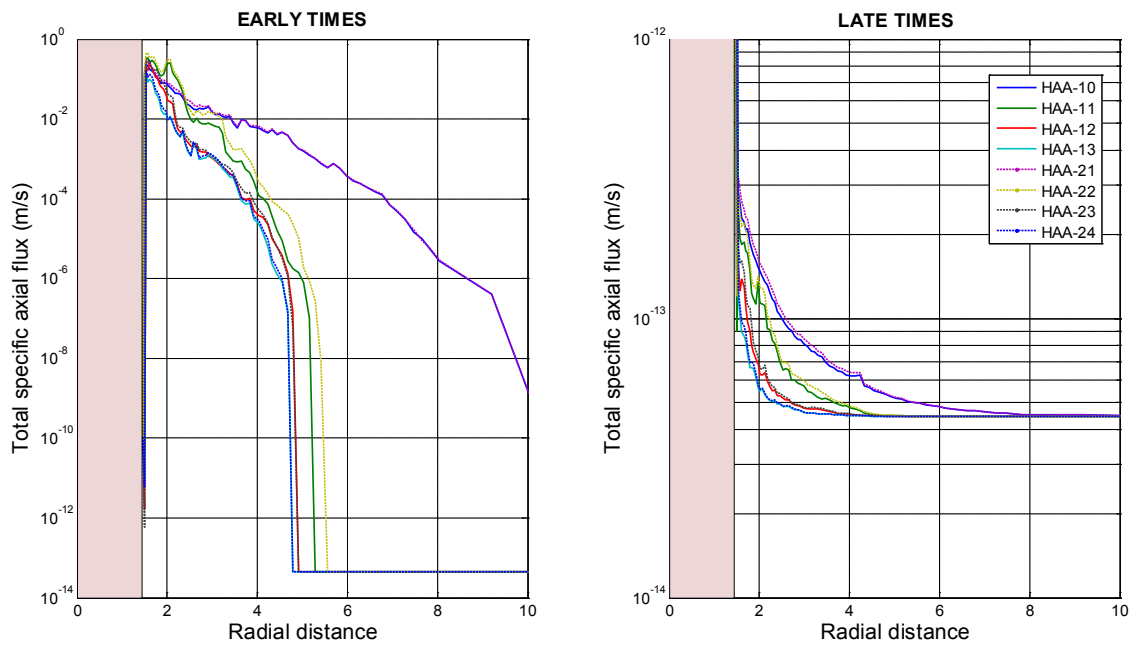


Fig. 4-12: Total axial fluxes at early (left) and late times (right) depending on strength parameters and elastic modulus of support. HAA models.

### Sensitivity to the presence of faults

The impact of pre-existent faults is addressed by comparing simulations HAA-16 to HAA-18 with HAA-11 to HAA-13. These simulations share all parameters and only differ in the presence/absence of pre-existent faults. Figures 4-13 and 4-14 report on fracture density and total specific axial fluxes respectively. As expected, the presence of pre-existent faults favors the generation and development of drilling induced fractures, what leads to increased fluxes.

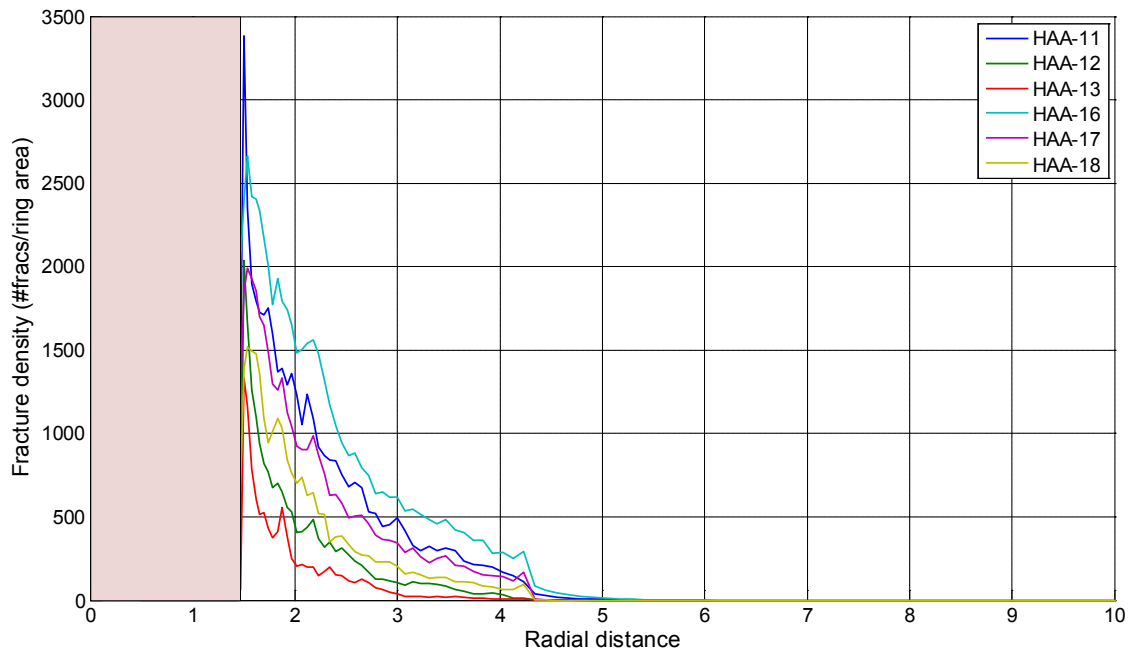


Fig. 4-13: Fracture density in the presence/absence of pre-existent faults. HAA models.

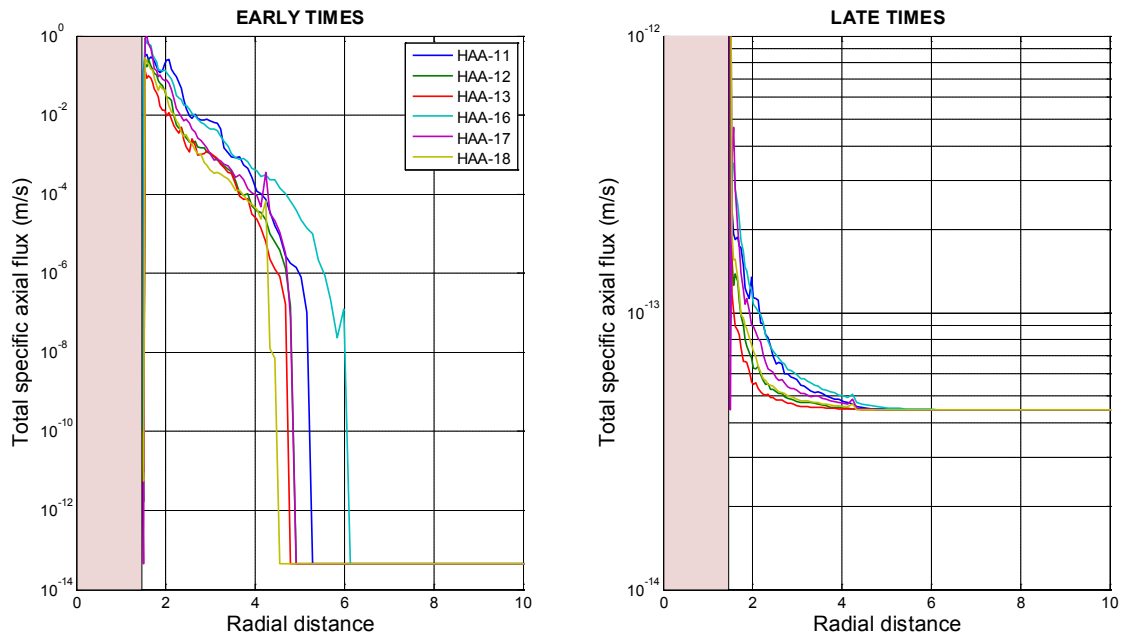


Fig. 4-14: Total axial fluxes at early (left) and late times (right) in the presence/absence of pre-existent faults. HAA models.

### 4.3 The EDZ around seal sections and shafts

Unlike HAA models, Shaft seal section models use an isotropic material model because the shaft is vertical and therefore perpendicular to the bedding plane strike. The main conclusions in Geomechanica (2013) are:

- The EDZ network is characterized by a log-spiral type of shear fractures radiating from the tunnel boundary.
- The EDZ resembles the characteristic lines that define the plastic zone around boreholes and tunnels in ductile materials.
- The damage zone extends to develop from the boundary in the direction perpendicular to the maximum principal in situ stress.
- The size of the EDZ is restricted and does not extend beyond 1 tunnel diameter.

Table 4-3 summarizes the Shaft model simulations. In this case, only in situ stresses and strength parameters are the subject of the sensitivity analysis.

Tab. 4-3: Summary of Shaft model simulations (from Geomechanica 2013). Note that models Shaft-01 and Shaft-02 do not contain fractures and are not considered in this analysis.

Model ID	$\sigma_v$ (MPa)	$\sigma_h$ (MPa)	Strength properties)	Elastic modulus of support (MPa)	Core softening ratio
Sensitivity to in-situ stress conditions					
SHAFT-01	11.0	16.5	OPA_Max	32	0.01
SHAFT-02	15.9	15.9			
SHAFT-03	19.6	15.7			
SHAFT-04	19.6	25.5			
Sensitivity to strength parameters					
SHAFT-05	11.0	16.5	OPA_Max x 0.5	32	0.01
SHAFT-06	15.9	15.9			
SHAFT-07	19.6	15.7			
SHAFT-08	19.6	25.5			
SHAFT-09	11.0	16.5	OPA_Max x 0.75		
SHAFT-10	15.9	15.9			
SHAFT-11	19.6	15.7			
SHAFT-12	19.6	25.5			
Re-compaction					
SHAFT-Rec2	19.6	15.7	OPA_Max	32	0.01
SHAFT-Rec3	19.6	25.5	OPA_Max		
SHAFT-Rec4	11.0	16.5	OPA_Max x 0.75		
SHAFT-Rec5	15.9	15.9	OPA_Max x 0.75		

#### 4.3.1 Model simulations and overall observations

Table 4-4 summarizes the averages of the geometric and hydraulic parameters defining the input FEMDEMs. Firstly, it becomes apparent that FEMDEMs are made of a large number of fractures patches. However, the number of fractures is smaller than in the HAA case, possibly due to the different stress regime. As commented in Chapter 3.3.2, the FEMDEM simulations overestimate fracture density by a factor  $\sim 10$ . Such high fracture density will lead to overestimated axial fluxes and underestimated resaturation times, what renders the calculations presented here a worst case scenario. Secondly, the mean geometric scores of inclination, length, aperture and area are quite sensitive to the parameters defining the FEMDEM. This effect will also be observed in the disparity of results with regards to axial fluxes.

Tab. 4-4: Geometric and hydraulic properties defining the input Shaft FEMDEM simulations. Columns 3 to 7 are average values. Horizontal lines split the sub-groups in Table 4-3. Results under re-compaction conditions are presented separately in Chapter 4.6.

Model	Number of fractures	Aperture (mm)	Length (mm)	Angle (rad)	Area(mm <sup>2</sup> )	log <sub>10</sub> T (m <sup>2</sup> /s)
Shaft-03	2567	0.68	88.62	-7.10	3.05	-3.60
Shaft-04	10308	0.72	88.50	-0.07	2.43	-3.52
Shaft-05	25661	0.39	89.34	-1.63	1.96	-4.31
Shaft-06	26813	0.37	88.76	-1.24	1.82	-4.38
Shaft-07	40085	0.37	89.39	-0.77	1.82	-4.40
Shaft-08	63469	0.40	90.28	0.00	1.84	-4.28
Shaft-09	5234	0.55	88.93	0.39	2.51	-3.88
Shaft-10	8369	0.53	88.80	0.57	2.62	-3.91
Shaft-11	11016	0.58	88.94	2.08	2.26	-3.81
Shaft-12	26289	0.57	89.08	0.72	2.03	-3.82

Figure 4-15 presents the spatial distribution of fracture density (i.e., number of fractures per unit area). The number of fractures at short radial distances, i.e., close to the liner, depends greatly on stress conditions and strength parameters under which the FEMDEM was generated. The observed variability is greater than that of the HAA models due to the change in the stress regime (purely horizontal to purely vertical). Still, a characteristic common to all Shaft FEMDEMs is that fracture density drops dramatically to almost negligible values after a radial distance  $\sim 10$  m (with respect to the center of the gallery). The total extension of the EDZ (i.e., zero fracture density) is almost the same for all FEMDEMs,  $\sim 12$  m. As a conclusion, the development and geometry of the EDZ greatly depends on in situ stress conditions and strength parameters.

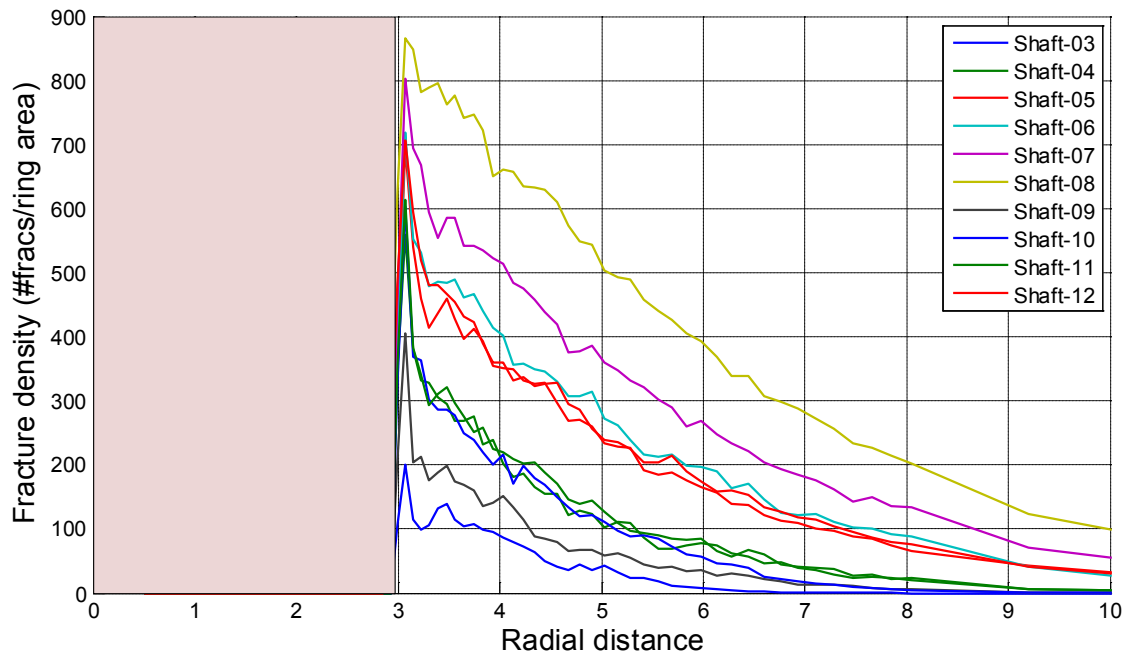


Fig. 4-15: Spatial distribution of equivalent fracture density (number of fractures on a ring of elements standardized by the ring area) of Shaft models. The pink inset depicts the buffer zone.

The same conclusions can be observed in Figures 4-16 and 4-17, which summarize calculated specific axial fluxes (equivalently, axial hydraulic conductivity) and fracture porosity respectively.

Regardless of in situ stress conditions and strength parameters, we observe:

- At early times (Figure 4-16a), fluxes are very high ( $10^{-1}$  to  $10^0$  m/s) due to the high transmissivity of the system (in average  $10^{-4}$  m<sup>2</sup>/s; Table 4-4). A similar result is also observable in the HAA models (see Figure 4-3a).
- At late times (Figure 4-16b), the resaturation of the system and the swelling of the clayey minerals of the matrix cause fractures to close. Consequently, the equivalent transmissivity of the system drops dramatically to an irreducible value  $5.7 \cdot 10^{-16}$  m<sup>2</sup>/s (value assumed in this study). This causes the specific flux to drop more than 13 orders of magnitude. It is worth to remark that the estimations presented here overestimate fluxes because fracture density is overestimated by a factor  $\sim 10$ .
- Overall, the spread of the specific fluxes is less than 1 order of magnitude at late times. Thus, specific flux is somewhat sensitive to in situ stress and strength parameters, but less sensitive than HAA models.
- All simulations yield an EDZ extension of 10 to 12 m with respect to the center of the gallery. Thus, the total extension of the EDZ is not very sensitive to local conditions. It is worth to mention that the effective extension of the EDZ, through which the main contribution of the flux circulates, strongly depends on local conditions. This is observed in the wide spread of specific fluxes at radial distances between 2 and 6 meters.

- Initial fracture porosity (Figure 4-17a) is relatively low, with values between 0.01 and 0.05 (1-5%). These values are substantially smaller than those of initial fracture porosity of the HAA models (~12%). Although average fracture length is larger in Shaft models (89 mm vs 32 mm for HAA models), the average aperture is similar (~0.5 mm). However, the average number of fractures is way smaller (22'000 for Shafts, 24'000 for HAA models, an exception being the model Shaft-08). The reduced number of fractures reduces considerably the fracture porosity. This observation is also commented in Geomechanica (2013).

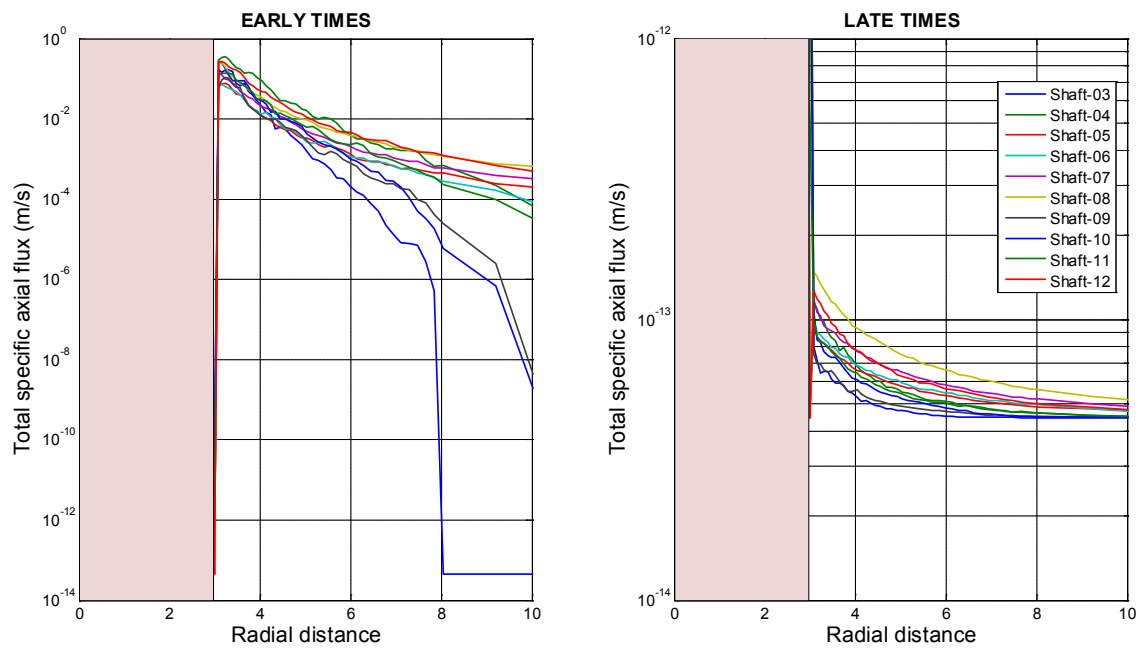


Fig. 4-16: Spatial distribution of total equivalent specific axial fluxes of Shaft models. The pink inset depicts the buffer zone. On the left, early time behavior, after excavation and emplacement. On the right, late time behavior, after full resaturation of the system (i.e., when all fractures are closed).

Figure 4-18 displays matrix porosity at early and late times. As observed, matrix porosity is piece-wise constant at early times and increases due to the swelling of the clayey minerals present in the fractures. Note that the distribution of total porosity is that of matrix porosity at late times (Figure 4-18b), because all fractures are closed.

Figures 4-19 to 4-22 report on the abstractions of the EDZ (see Chapter 3.4.5). Figure 4-19 depicts an equivalent EDZ radius at which fracture density is 100 fractures/m<sup>2</sup>. We have selected a threshold value 1 order of magnitude larger than that used for the HAA models because fracture density of Shaft FEMDEMs is considerably smaller. Using the same threshold would lead to unrealistically overestimated EDZ equivalent radii and specific axial fluxes.

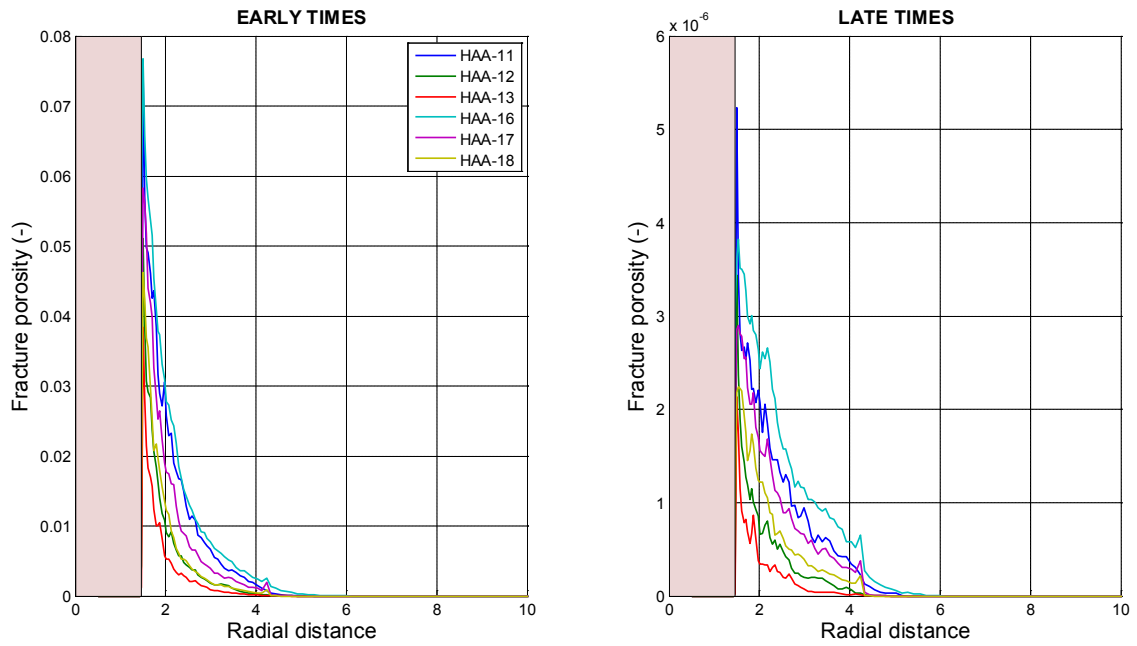


Fig. 4-17: Spatial distribution of fracture porosity of Shaft models. The pink inset depicts the buffer zone. On the left, early time behavior, after excavation and emplacement. On the right, late time behavior, after full resaturation of the system (i.e., assuming that all fractures are closed).

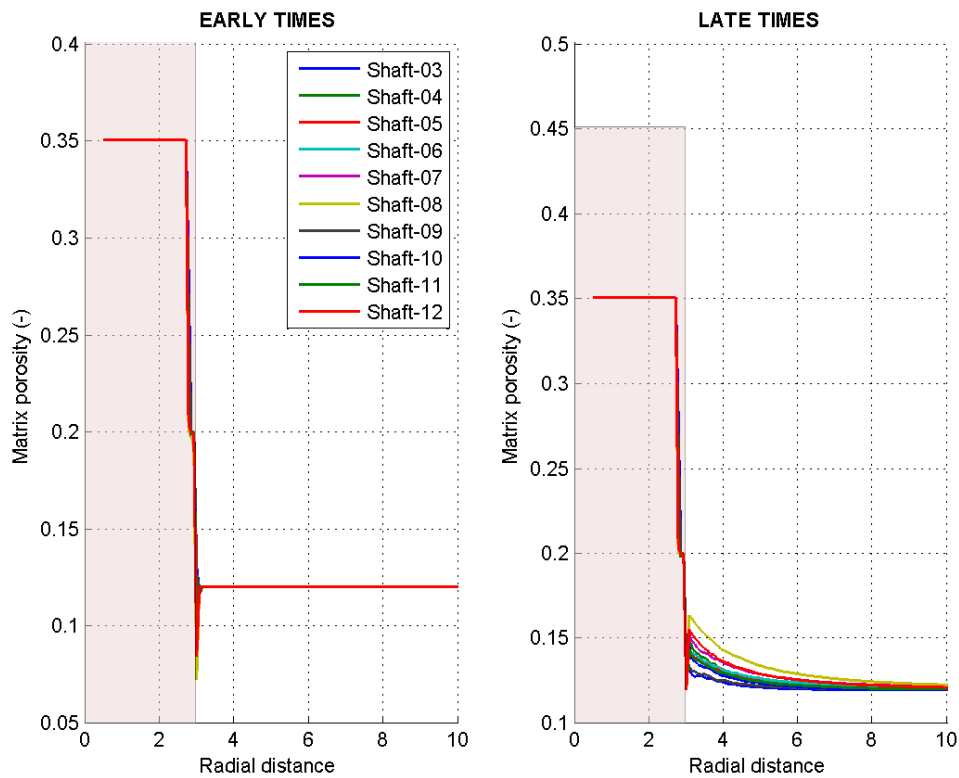


Fig. 4-18: Spatial distribution of matrix porosity of HAA models. The pink inset depicts the buffer zone. On the left, early time behavior, after excavation and emplacement. On the right, late time behavior, after full resaturation of the system (i.e., assuming that all fractures are closed). Note that matrix porosity represents total porosity at late times.

As observed, the effective extent of the EDZ depends greatly on local conditions of in-situ stresses and strength parameters. The variability of the EDZ extension of Shaft models is greater than that of HAA models because the number of fractures defining the FEMDEM is also more variable. An interesting finding is the quadratic relationship between the radius of the abstracted EDZ and the number of fractures defining the FEMDEM (Figure 4-20).

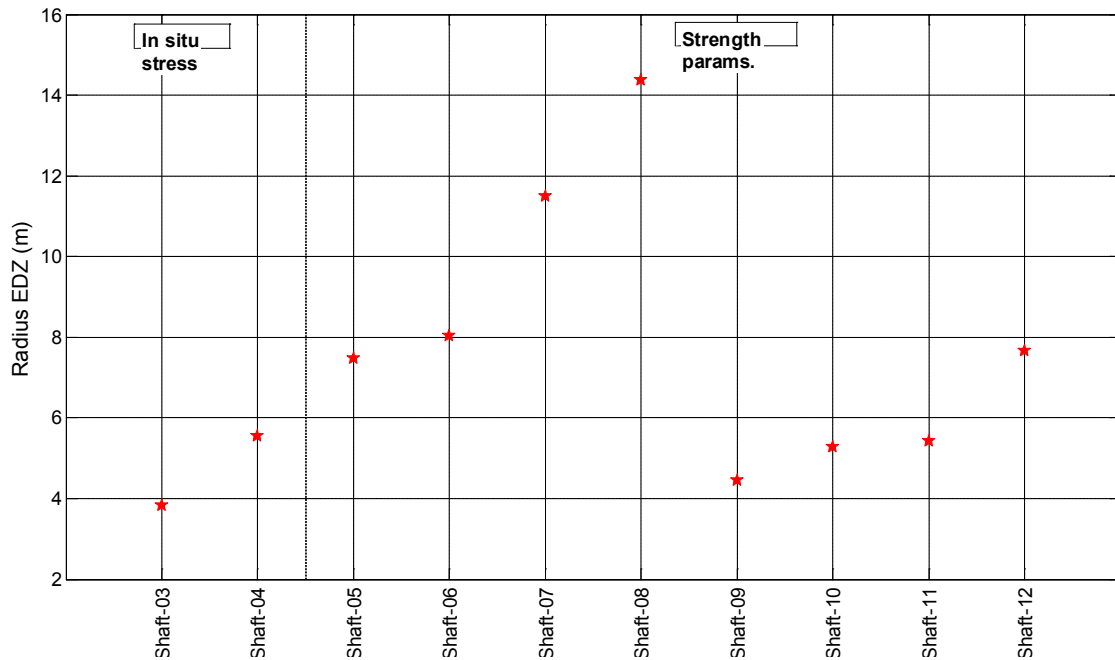


Fig. 4-19: Equivalent radius of the EDZ abstraction of Shaft models, defined as the radial distance at which fracture density drops to 100 fractures/m<sup>2</sup>. Textboxes and vertical dashed lines depict the different groups of simulations in Table 4.3. Simulations of EDZ under re-compaction conditions are presented separately in Chapter 4.6.

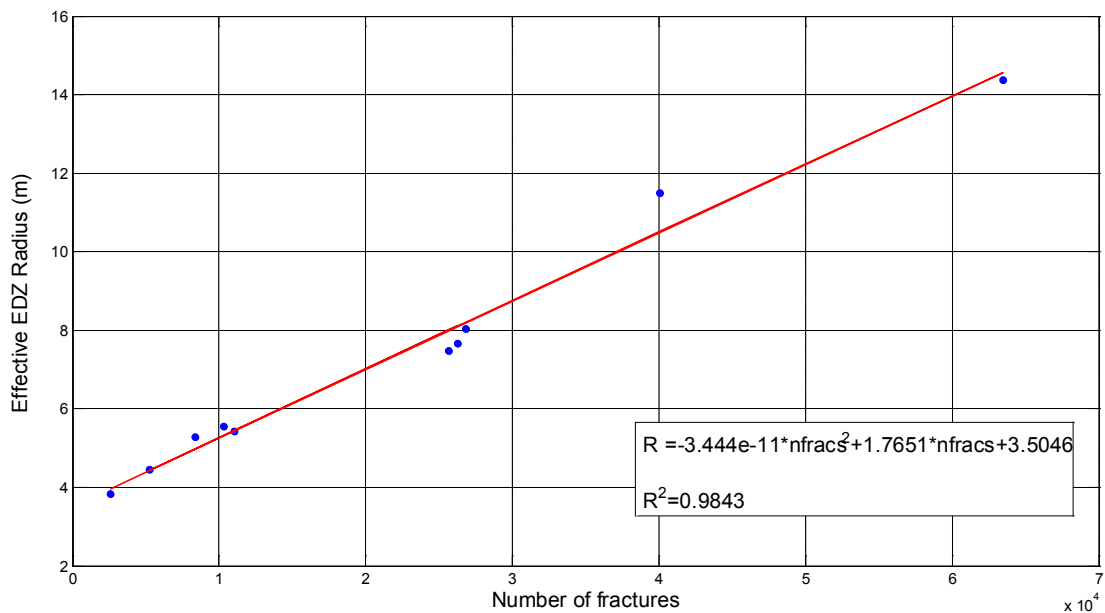


Fig. 4-20: Equivalent radius of the abstracted EDZ of shaft models vs. number of fractures defining the FEMDEM. In the inset, best fitting trend line and correlation coefficient.

Overall, the radius of the abstracted EDZ is between 3 and 12 m. This result is coherent to that in Geomechanica (2013). Figure 4-21 summarizes the total equivalent specific fluxes of the EDZs abstracted with the radii in Figure 4-19. FEMDEM parameters have minor impact on the absolute value of specific fluxes. However, the surface across which the specific flux circulates is strongly affected by small variations in in situ stresses and strength parameters. Local conditions and strength parameters have little impact on the late time specific fluxes. Note that the abstracted specific flux drops approximately 12 orders of magnitude, much more than in the HAA models. Finally, total porosity is not much sensitive to local conditions and strength parameters (Figure 4-22), an average value  $\sim 0.13$  (13%) regardless of the FEMDEM parameterization.

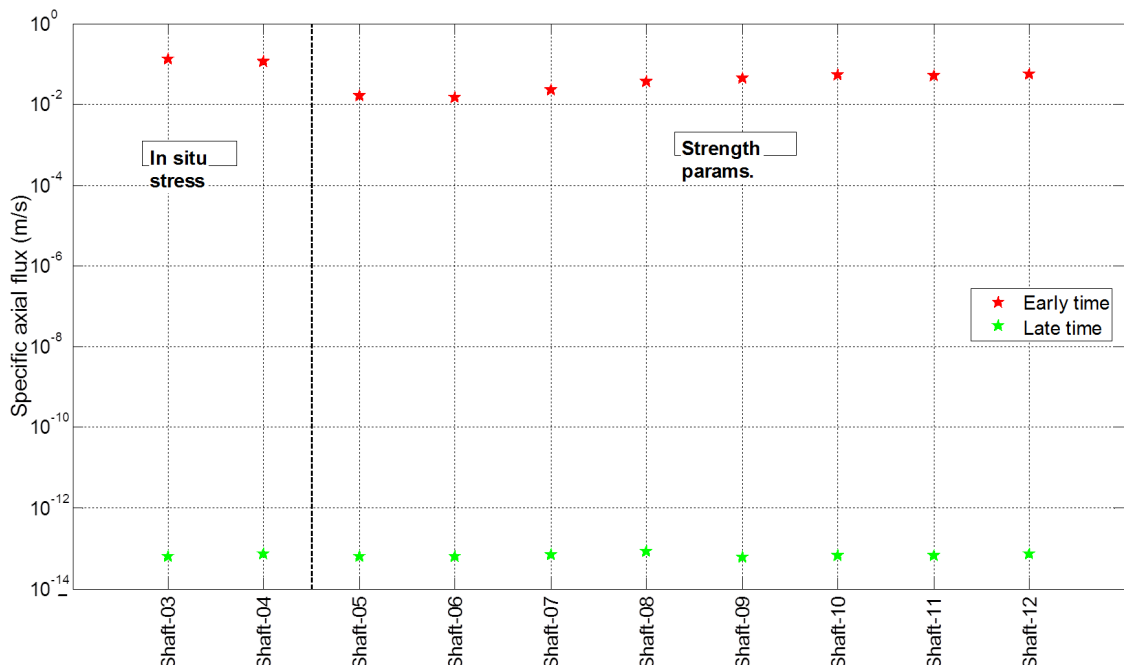


Fig. 4-21: Early and late time total equivalent specific fluxes of the abstracted Shaft models.

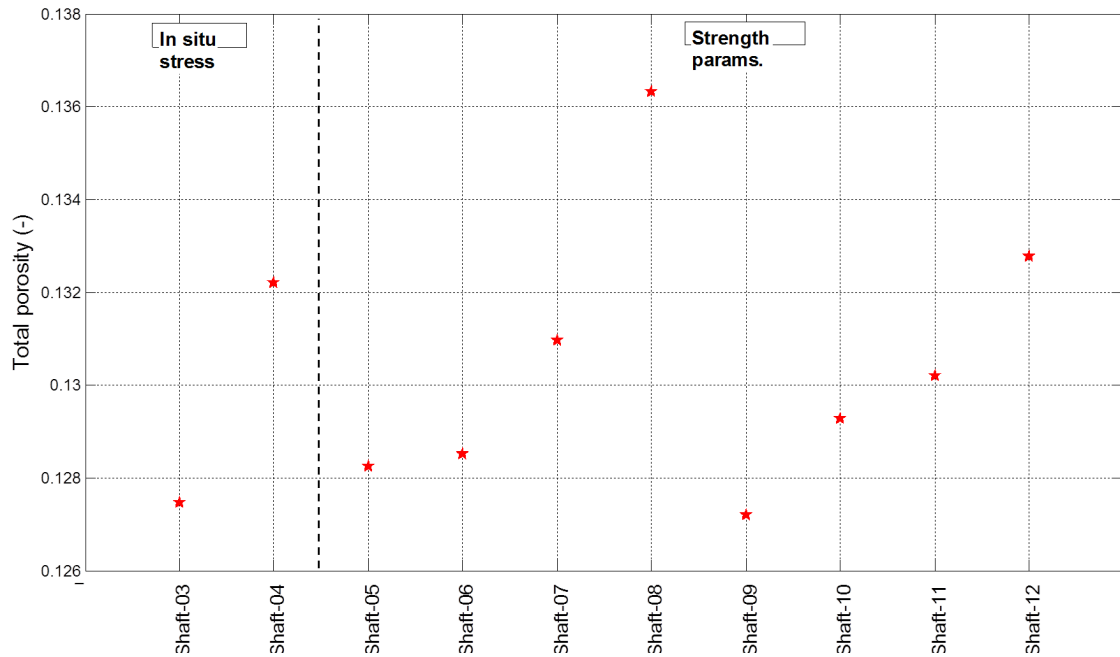


Fig. 4-22: Equivalent total porosity of the abstracted EDZ for Shaft models.

So far, we have analyzed all Shaft simulations altogether to shed light on the global behavior and to detect some trends of the sensitivity to local conditions of in situ stresses and strength parameters. Next section is devoted to the analysis of the sensitivities of the near field behavior to variations in a specific parameter. Chapter 4.6 will summarize the results of EDZs under re-compaction conditions.

### 4.3.2 Sensitivity analysis

This section reports on the sensitivity analysis of Shaft models to in situ stress conditions and strength parameters. To that end, we compare first Shaft models 03 and 04, which differ only on the stress conditions. Secondly, we compare Shaft models sharing stress conditions and vary only the stress parameters. Two groups of simulations are considered, i.e., 03, 07 and 11 ( $\sigma_v = 19.6$  MPa,  $\sigma_h = 15.7$  MPa with varying strength parameters) and 04, 08 and 12 ( $\sigma_v = 19.6$  MPa,  $\sigma_h = 25.5$  MPa with varying strength parameters).

The remainder of this section is organized accordingly. Each subsection contains similar figures depicting (i) the spatial distribution of total equivalent specific axial flux (equivalently, of hydraulic conductivity) at early and late times and (ii) the spatial distribution of equivalent total porosity at those times. A table summarizes the abstracted models of the EDZ, in terms of radius and equivalent parameters.

#### Sensitivity to in-situ stress conditions

We compare Shaft models 03 and 04, sharing all parameters but the stress state. Figures 4-23 and 4-24 report on fracture density and total axial fluxes respectively. As expected, an increase in total stress from 15.7 (Shaft-03) to 25.5 (Shaft-04) leads to a substantial decrease in fracture density and, correspondingly, in specific axial flux. The same conclusions can be observed in the abstractions of the EDZ (Figures 4-19 to 4-22).

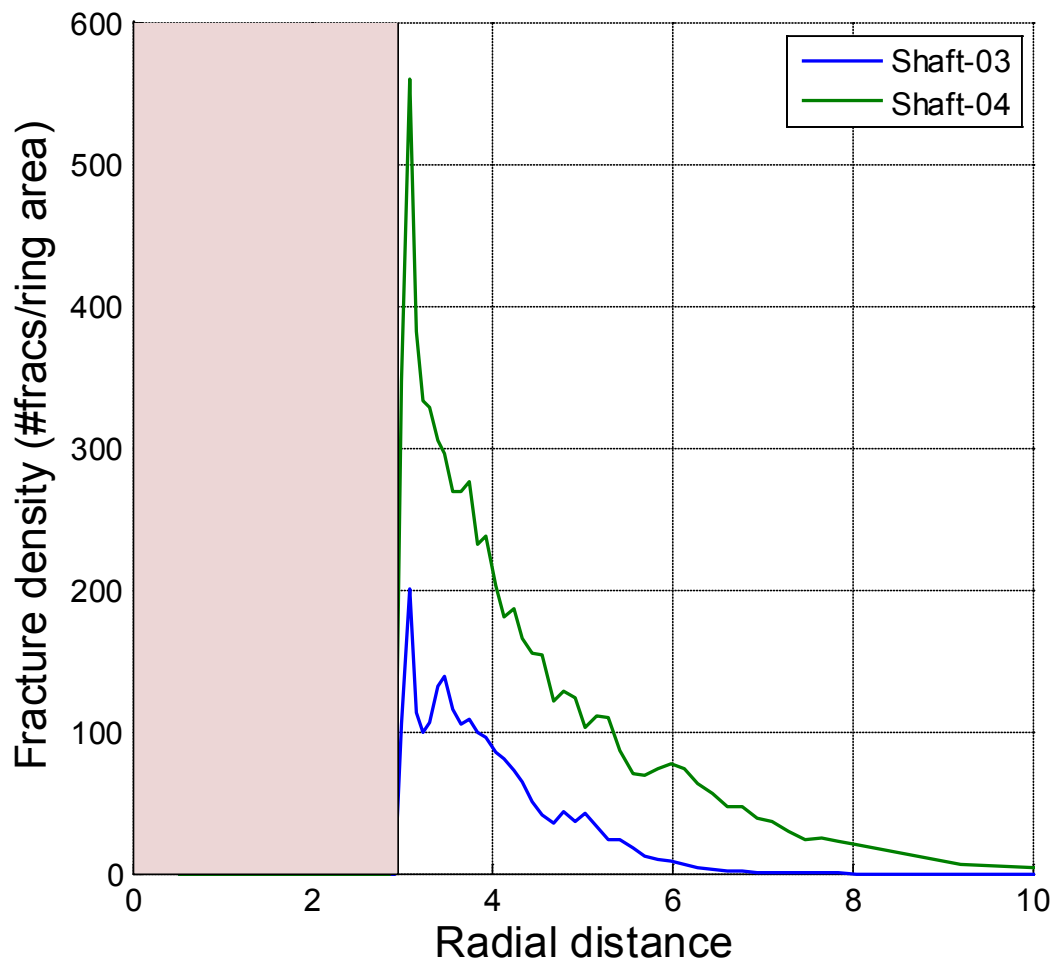


Fig. 4-23: Fracture density depending on in situ stress conditions. Shaft models.

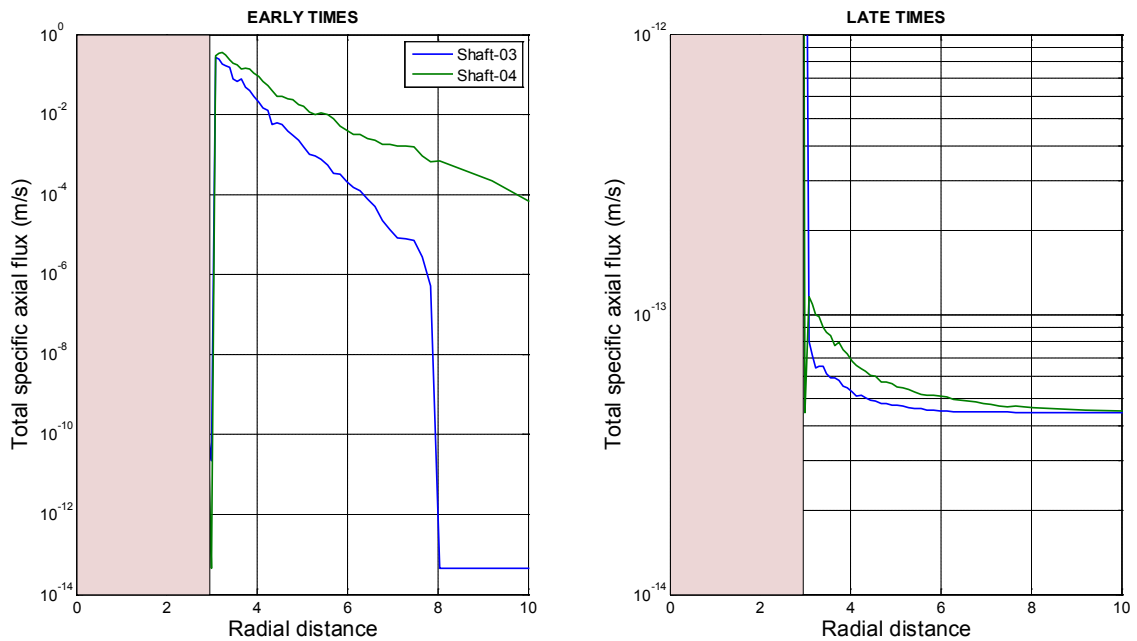


Fig. 4-24: Total axial fluxes at early (left) and late times (right) depending on in situ stress conditions. Shaft models.

### Sensitivity to strength parameters

Two groups of simulations are considered, i.e., 03, 07 and 11 ( $\sigma_v = 19.6$  MPa,  $\sigma_h = 15.7$  MPa) and 04, 08 and 12 ( $\sigma_v = 19.6$  MPa,  $\sigma_h = 25.5$  MPa). Strength parameters are OPAm<sub>ax</sub> (models 03 and 04), OPAm<sub>ax</sub>\*0.5 (models 07 and 08) and OPAm<sub>ax</sub>\*0.75 (models 11 and 12). As expected, increasing the strength parameters leads to smaller fracture densities (Figure 4-25) and, correspondingly, to smaller specific axial fluxes (Figure 4-26).

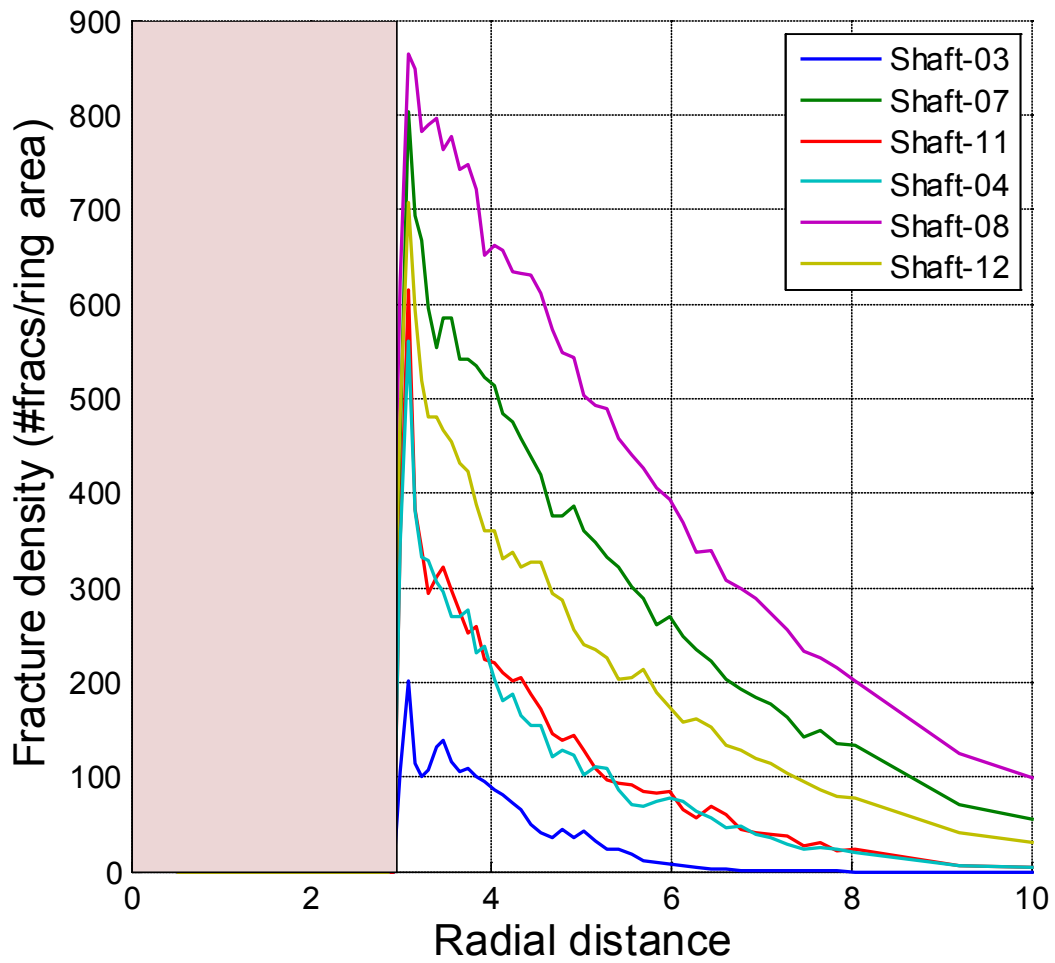


Fig. 4-25: Fracture density depending on strength parameters. Shaft models.

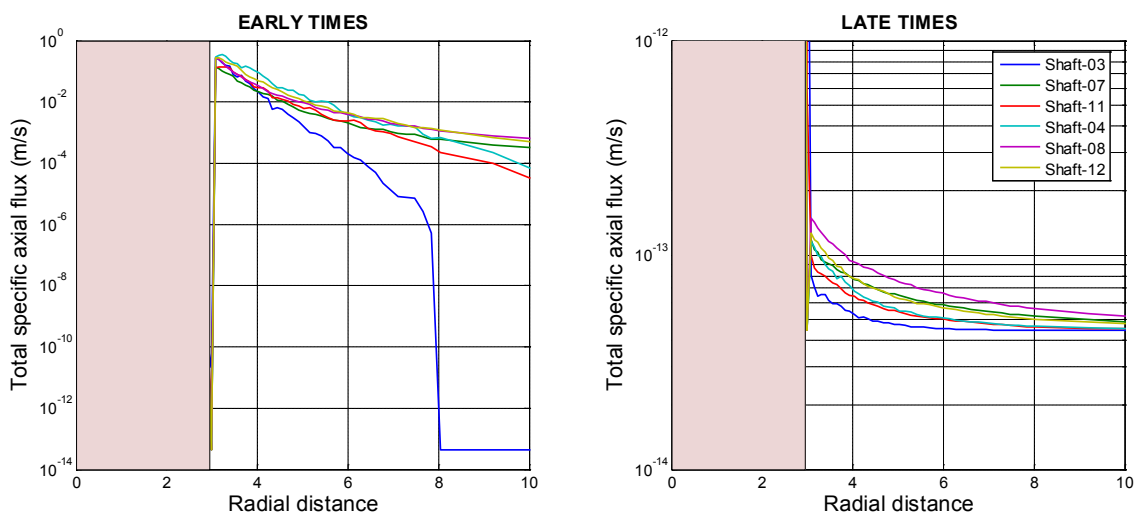


Fig. 4-26: Total axial fluxes at early (left) and late times (right) depending on strength parameters. Shaft models.

#### 4.4 EDZ under re-compaction conditions

A sequence of simulations was dedicated to the re-compaction of the EDZ of a backfilled seal section in response to the swelling pressure exerted by a bentonite buffer. Swelling pressures of 10 MPa were mimicked by the application of a radial stress on the tunnel circumference (Geomechanica 2013). The main effect of the reconsolidation process is a dramatic reduction of the initial fracture transmissivity. 8 and 4 simulations are carried out for the HAA and Shaft models that mimic different in situ stresses and strength parameters. The main conclusion reported by Geomechanica (2013) is that the application of a reconsolidation pressure, together with the long-term degradation of the shotcrete stiffness causes a partial reversal of displacements in the excavation walls. This phenomenon is reflected in the total void area of the EDZ, which experiences a total reduction ranging between 50 and 95% (HAA vs Shaft models). Although the application of the reconsolidation pressure changes the stress redistribution in the rock mass, it does not contribute to further rock mass fracturing.

##### 4.4.1 HAA-Rec models

Table 4-5 summarizes the averages of the geometric and hydraulic parameters defining the input FEMDEMs. A comparison between Table 4-2 and Table 4-5 reveals the dramatic reduction in the initial fracture transmissivity. Initial fracture transmissivities are reduced by more than one order of magnitude under reconsolidation and shotcrete degradation conditions.

Tab. 4-5: Geometric and hydraulic properties defining the input HAA FEMDEM simulations. Columns 3 to 7 are average values. FEMDEM parameters are reported in Table 4-1.

Model	Number of fractures	Aperture (mm)	Length (mm)	Inclination (rad)	Area (mm <sup>2</sup> )	log <sub>10</sub> T (m <sup>2</sup> /s)
HAA-Rec1	51050	0.41	34.38	0.00	1.02	-5.39
HAA-Rec2	43513	0.36	34.06	0.02	1.10	-5.66
HAA-Rec3	43616	0.41	34.08	-0.01	0.91	-5.38
HAA-Rec4	56205	0.49	35.54	-0.02	1.27	-5.036
HAA-Rec5	18991	0.38	31.41	-0.01	1.38	-5.76
HAA-Rec6	66264	0.37	36.9	0.00	0.97	-5.47
HAA-Rec7	44003	0.31	34.1	0.01	0.95	-6.01
HAA-Rec8	20270	0.32	31.5	0.00	1.12	-6.07

Figure 4-27 displays the spatial distribution of fracture density (i.e., number of fractures per unit area). This score is useful for the definition of the extension of the EDZ. The number of fractures at short radial distances, i.e., close to the liner, depends greatly on stress conditions and strength parameters under which the FEMDEM was generated. However, a characteristic common to all FEMDEMs is that fracture density drops dramatically to almost negligible values after a radial distance  $\sim 4.5$  m (radial distances are always measured with respect to the center of the gallery). The total extension of the EDZ (i.e., zero fracture density) is almost the same for all FEMDEMs,  $\sim 6$  m. This average extension is 2 m smaller than that of the HAA models due to the smaller initial transmissivity under reconsolidation conditions, even though the number of fractures is similar in both models.

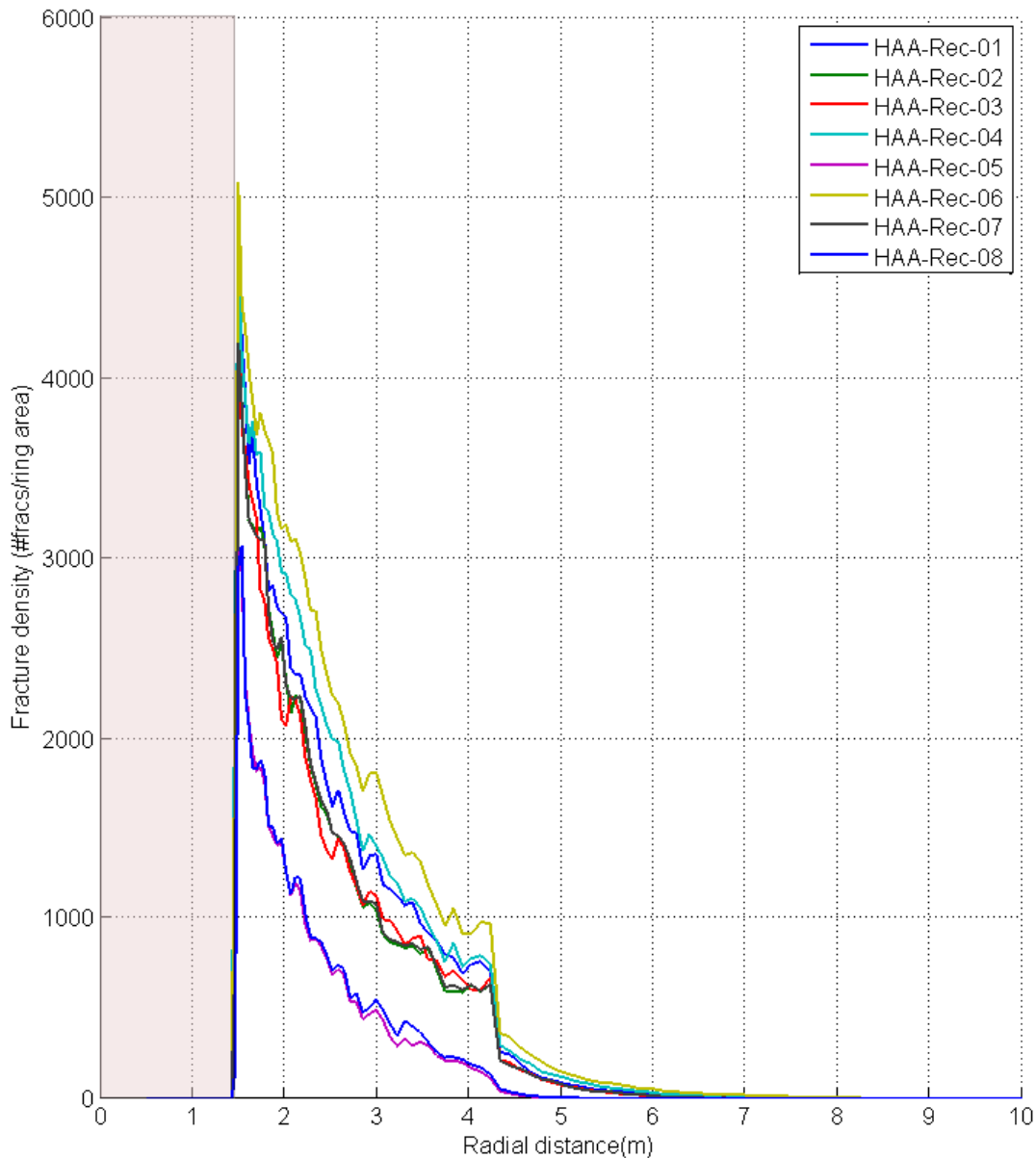


Fig. 4-27: Spatial distribution of equivalent fracture density (number of fractures on a ring of elements standardized by the ring area) of HAA-Rec models. The inset depicts the buffer zone.

The same conclusions can be observed in Figures 4-28 and 4-29, which summarize calculated total specific axial fluxes (equivalently, axial hydraulic conductivities) and fracture porosity respectively. Regardless of in situ stress conditions and strength parameters, we observe:

- At early times (Figure 4-28a), specific fluxes are very high ( $10^{-2}$  to  $10^{-1}$  m/s) due to the still high transmissivity of the system (in average  $2.5 \cdot 10^{-6}$  m<sup>2</sup>/s; Table 4-5).
- At late times (Figure 4-28b), the equivalent transmissivity of the system drops dramatically to an irreducible value  $5.7 \cdot 10^{-16}$  m<sup>2</sup>/s (assumed value). This causes the specific flux to drop more than 13 orders of magnitude. It is worth to remark that the estimations presented here overestimate fluxes because fracture density is overestimated by a factor 10. As such, actual fluxes parallel to the gallery are expected to be even smaller than the ones calculated here.

- Overall, the spread of the specific fluxes is less than 1 order of magnitude at late times. Thus, specific flux is not much sensitive to in situ stress and strength parameters.
- All simulations yield an EDZ extension of  $\sim 6$  m (radial distance to the center of the gallery). Thus, the total extension of the EDZ is not sensitive to local conditions. It is worth to mention that the effective extension of the EDZ, through which the main contribution of the axial flux circulates, strongly depends on local conditions. This is observed in the spread of specific fluxes at radial distances between 1.5 and 4 meters.
- Initial fracture porosity (Figure 4-29a) is 0.07 (or 7%), almost 50% of the initial porosity in the absence of reconsolidation (12%). Fracture porosity drops to negligible values of  $\sim 10^{-6}$  when all fractures are closed. It is worth to mention that, although fracture aperture is set to a constant irreducible value, porosity at late times is not constant, as it also depends on fracture length (Equation 3-3).

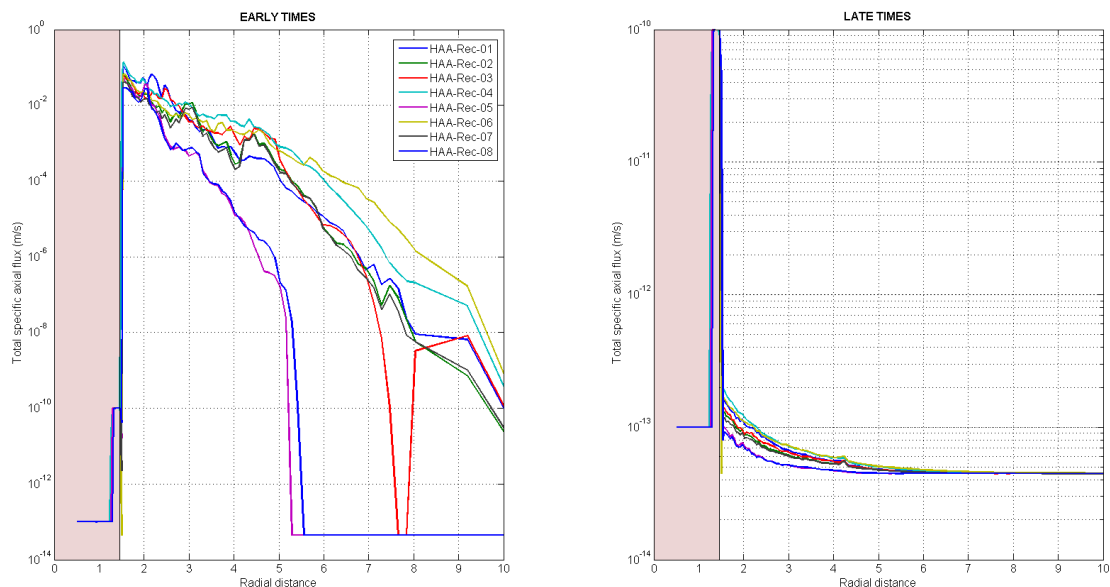


Fig. 4-28: Spatial distribution of total equivalent specific axial fluxes of HAA-Rec models. The pink inset depicts the buffer zone. On the left, early time behavior, after excavation and emplacement. On the right, late time behavior, after full resaturation of the system (i.e., assuming that all fractures are closed).

Figure 4-30 displays matrix porosity at early and late times. As observed, matrix porosity is piece-wise constant (deterministic values are summarized in Table 3-2) at early times and increases at the area encompassed by the EDZ due to the swelling of the clayey minerals. Note that the distribution of total porosity is that of matrix porosity at late times (Figure 4-30b), because it is assumed that all fractures are closed.

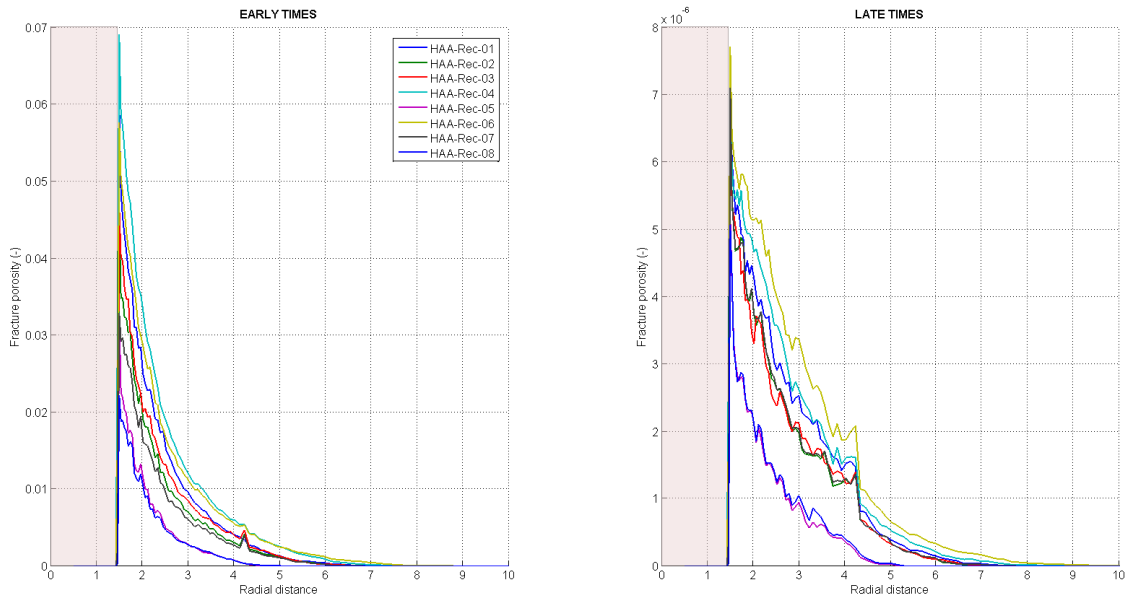


Fig. 4-29: Spatial distribution of fracture porosity of HAA-Rec models. The inset depicts the buffer zone. On the left, early time behavior, after excavation and emplacement. On the right, late time behavior, after full resaturation of the system (i.e., when all fractures are closed).

Figures 4-31 to 4-33 report on the abstractions of the EDZ (see Chapter 3.4.5). Figure 4-31 depicts an equivalent EDZ radius at which fracture density is approximately 10 fractures/m<sup>2</sup>. The abstracted EDZ equivalent radius is 3-4.5 meters depending on situ stress conditions. This result is coherent with that of Geomechanica (2013). Figure 4-32 summarizes the total equivalent specific axial fluxes of the EDZs abstracted with the radii in Figure 4-31. As observed, local conditions and strength parameters have some impact on the early time fluxes. The same conclusion arises from Figure 4-33, reporting on total equivalent porosity. However, local conditions and strength parameters have little impact on the late time specific fluxes. Note that the abstracted specific flux drops approximately 10 orders of magnitude in all cases. Finally, total porosity is not at all sensitive to local conditions and strength parameters (Figure 4-33).

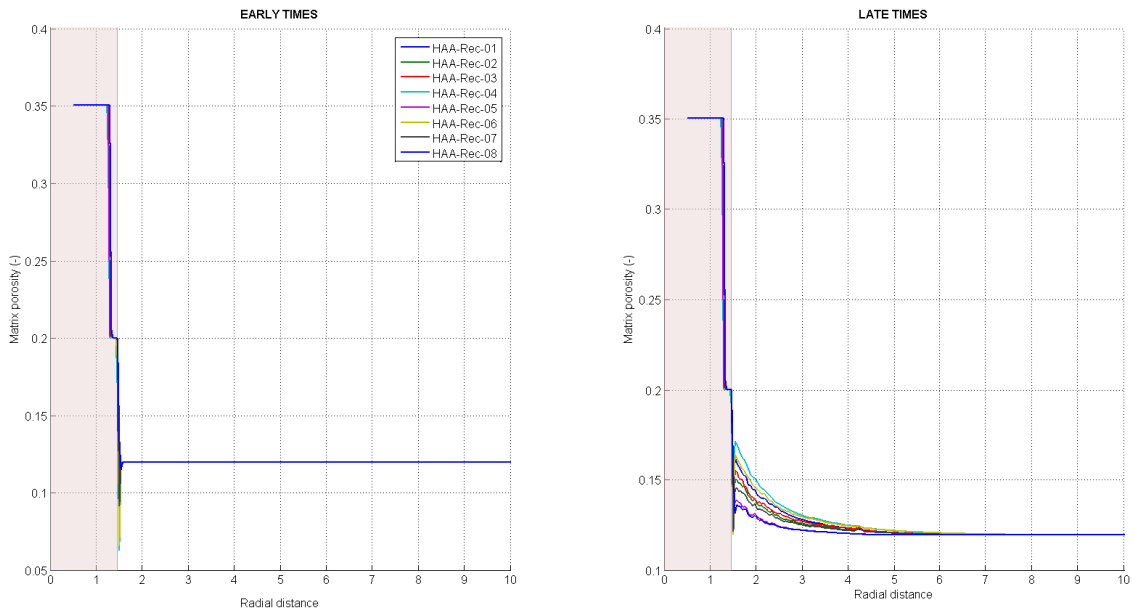


Fig. 4-30: Spatial distribution of matrix porosity of HAA-Rec models. The inset depicts the buffer zone. On the left, early time behavior, after excavation and emplacement. On the right, late time behavior, after full resaturation of the system (i.e., assuming that all fractures are closed). Note that matrix porosity represents total porosity at late times.

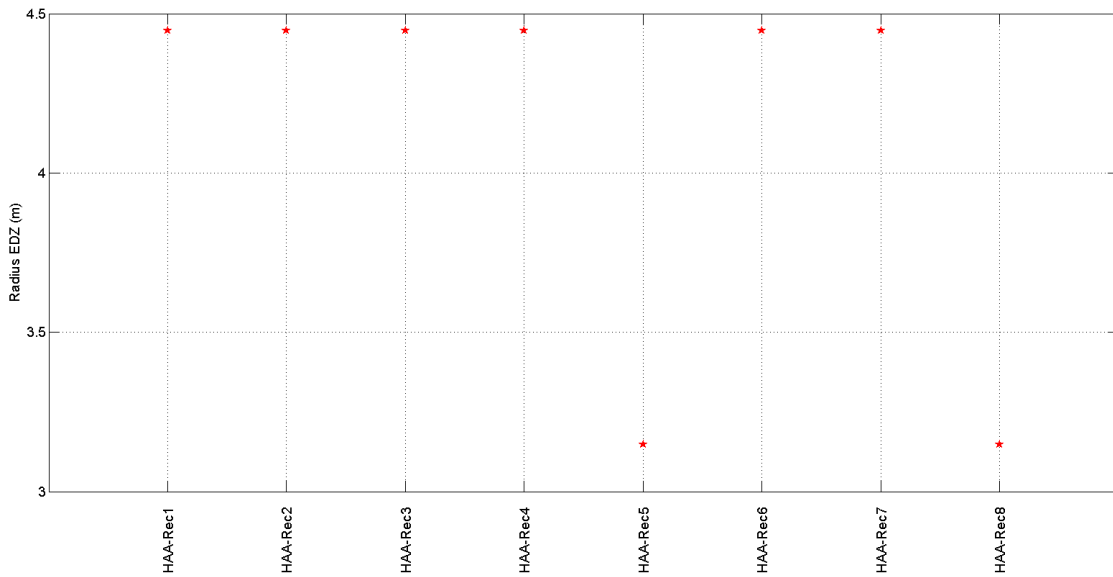


Fig. 4-31: Equivalent radius of the EDZ abstraction of HAA-Rec models, defined as the radial distance at which fracture density drops to 10 fractures/m<sup>2</sup>.

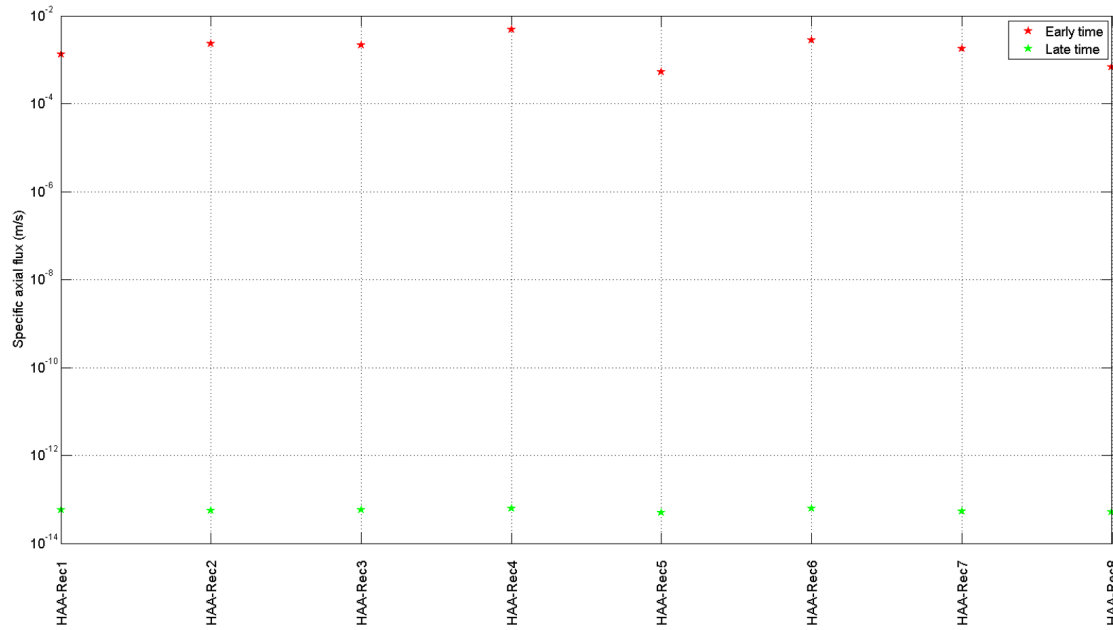


Fig. 4-32: Early and late time total equivalent specific fluxes of the abstracted HAA-Rec models.

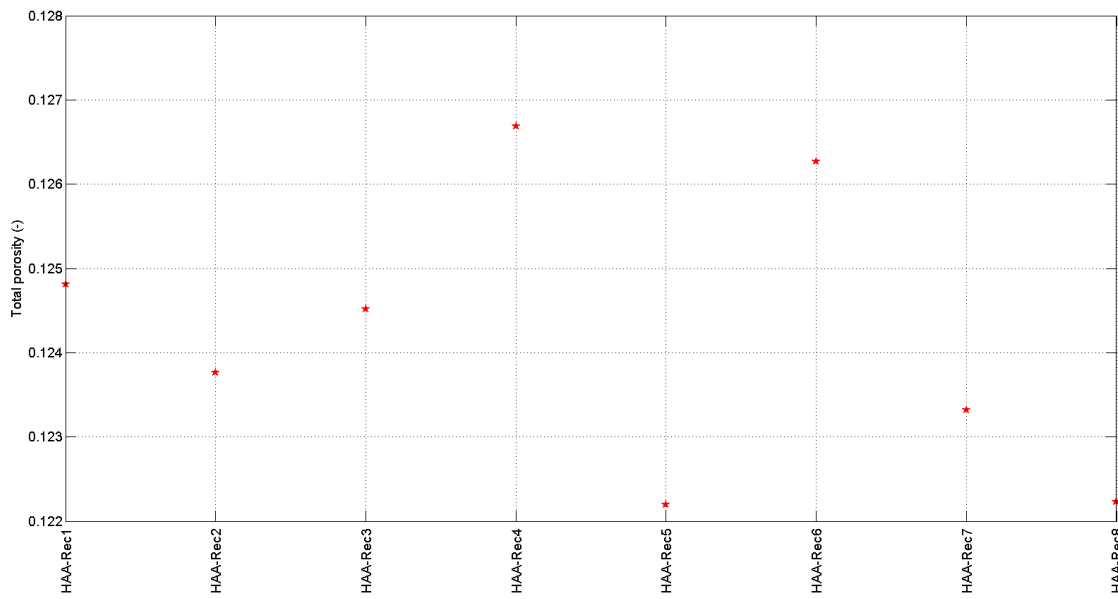


Fig. 4-33: Total equivalent porosity of the abstracted HAA-Rec models.

#### 4.4.2 Shaft\_Rec models

Table 4-6 summarizes the averages of the geometric and hydraulic parameters defining the input FEMDEMs. As observed in the HAA-Rec models, initial fracture transmissivity is reduced by more than one order of magnitude (Table 4-4 and Table 4-6).

Tab. 4-6: Geometric and hydraulic properties defining the input HAA FEMDEM simulations. Columns 3 to 7 are average values. FEMDEM parameters are reported in Table 4-3.

Model	Number of fractures	Aperture (mm)	Length (mm)	Inclination (rad)	Area (mm <sup>2</sup> )	log <sub>10</sub> T (m <sup>2</sup> /s)
Shaft-Rec2	2694	0.70	89.3	-3.46	5.17	-5.21
Shaft-Rec3	10568	0.81	89.4	0.19	4.78	-4.41
Shaft-Rec4	5440	0.46	89.8	0.92	3.06	-5.48
Shaft-Rec5	8544	0.45	89.7	1.1	2.95	-5.52

Figure 4-34 displays the spatial distribution of fracture density (i.e., number of fractures per unit area). This score is useful for the definition of the extension of the EDZ. The number of fractures at short radial distances, i.e., close to the liner, depends greatly on stress conditions and strength parameters under which the FEMDEM was generated. However, a characteristic common to all FEMDEMs is that fracture density drops dramatically to almost negligible values after a radial distance  $\sim 8$  m. The total extension of the EDZ (i.e., zero fracture density) is almost the same for all FEMDEMs,  $\sim 9$  m. This average extension is 2 m smaller than that of the Shaft models due to the smaller initial transmissivity under reconsolidation conditions, even though the number of fractures is similar in both models.

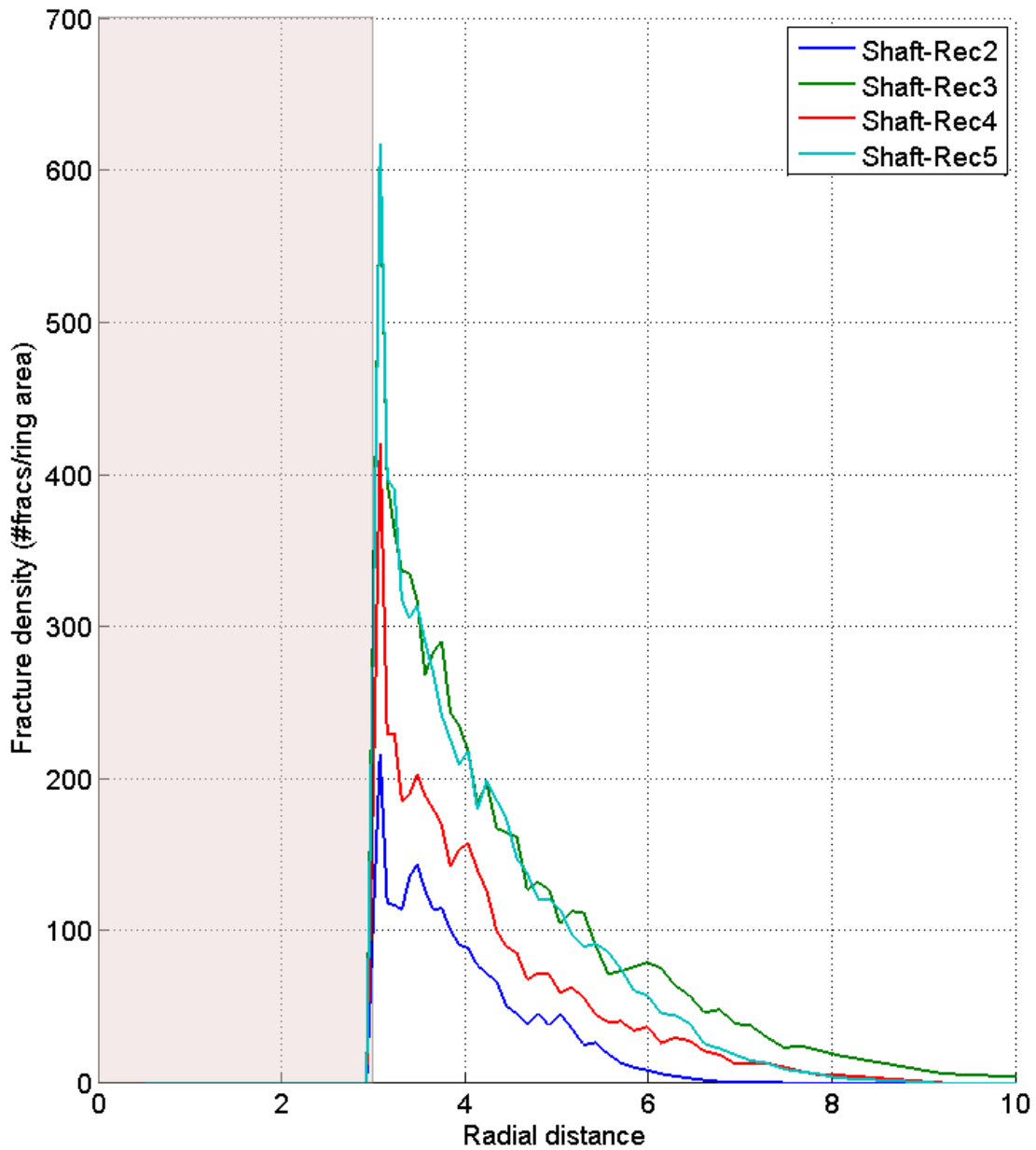


Fig. 4-34: Spatial distribution of equivalent fracture density (number of fractures on a ring of elements standardized by the ring area) of Shaft-Rec models. The inset depicts the buffer zone.

The same conclusions can be observed in Figures 4-35 and 4-36, which summarize calculated total specific axial fluxes (equivalently, axial hydraulic conductivities) and fracture porosity respectively. Regardless of in situ stress conditions and strength parameters, we observe:

- At early times (Figure 4-35a), specific fluxes are very high ( $10^{-2}$  to  $10^{-1}$  m/s) due to the still high transmissivity of the system (in average  $6.3 \cdot 10^{-6}$  m<sup>2</sup>/s; Table 4-5).

- At late times (Figure 4-35b), the equivalent transmissivity of the system drops dramatically to an irreducible value  $5.7 \cdot 10^{-16} \text{ m}^2/\text{s}$  (assumed value). This causes the specific flux to drop more than 13 orders of magnitude. It is worth to remark that the estimations presented here overestimate fluxes because fracture density is overestimated by a factor 10. As such, actual fluxes parallel to the gallery are expected to be even smaller than the ones calculated here.
- Overall, the spread of the specific fluxes is minimum at late times. Thus, specific flux is not at all sensitive to in situ stress and strength parameters.
- All simulations yield an EDZ extension of  $\sim 9 \text{ m}$  (radial distance to the center of the gallery). Thus, the total extension of the EDZ is not sensitive to local conditions. It is worth to mention that the effective extension of the EDZ, through which the main contribution of the axial flux circulates, strongly depends on local conditions. This is observed in the spread of specific fluxes at radial distances between 3 and 4 meters.
- Initial fracture porosity (Figure 4-36a) is 0.02 (or 2%), 50% of the initial porosity in the absence of reconsolidation (5%). Fracture porosity drops to negligible values of  $\sim 10^{-6}$  when all fractures are closed. It is worth to mention that, although fracture aperture is set to a constant irreducible value, porosity at late times is not constant, as it also depends on fracture length (Equation 3-3).

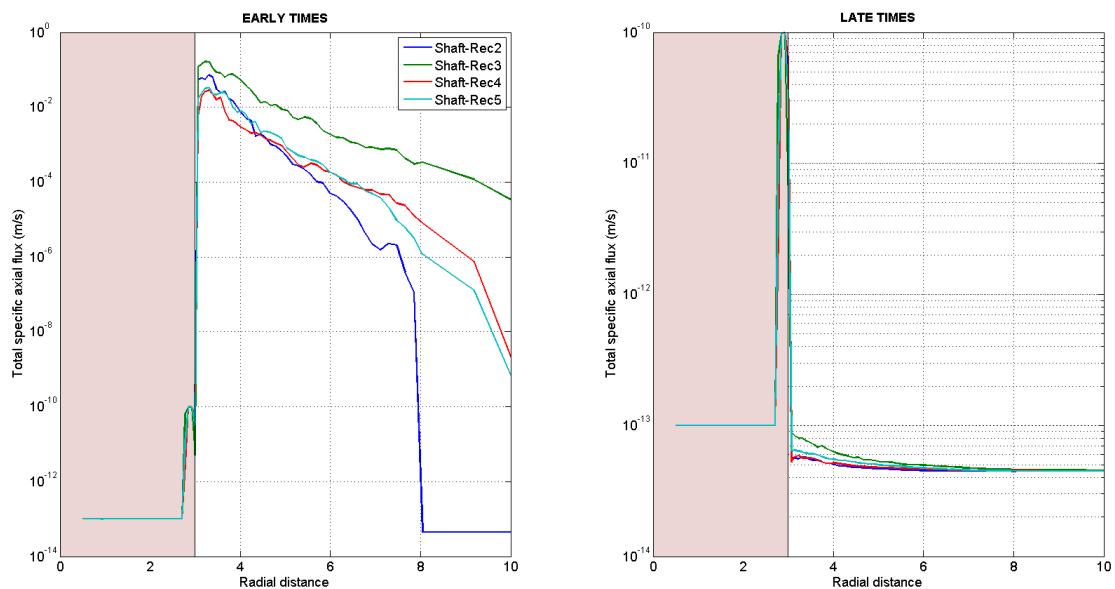


Fig. 4-35: Spatial distribution of total equivalent specific axial fluxes of Shaft-Rec models. The pink inset depicts the buffer zone. On the left, early time behavior, after excavation and emplacement. On the right, late time behavior, after full resaturation of the system (i.e., assuming that all fractures are closed).

Figure 4-37 displays matrix porosity at early and late times. As observed, matrix porosity is piece-wise constant (deterministic values are summarized in Table 3-2) at early times and increases at the area encompassed by the EDZ due to the swelling of the clayey minerals. Note that the distribution of total porosity is that of matrix porosity at late times (Figure 4-37b), because it is assumed that all fractures are closed.

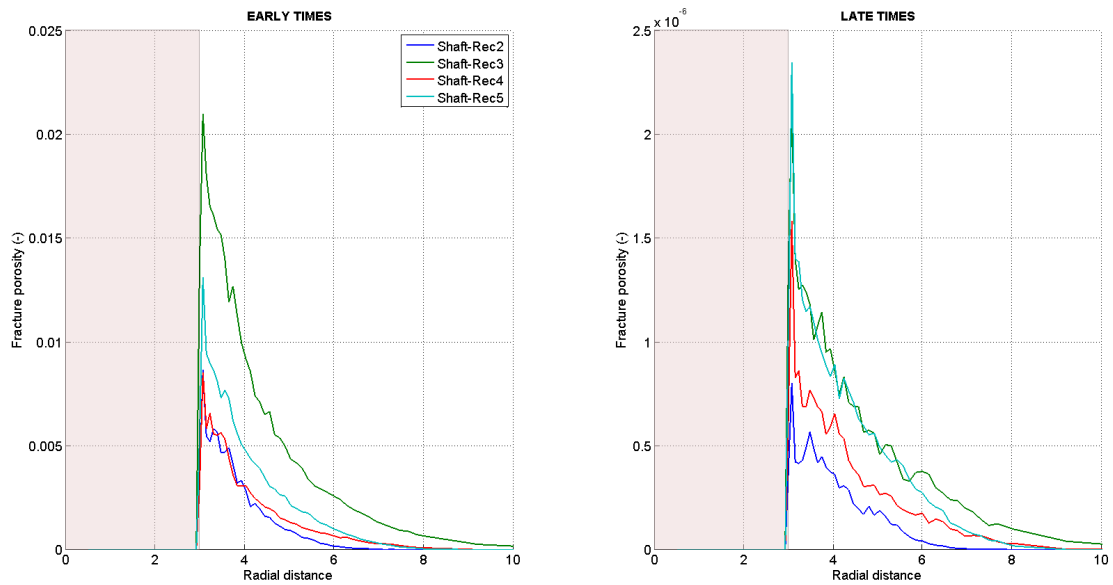


Fig. 4-36: Spatial distribution of fracture porosity of Shaft-Rec models. The inset depicts the buffer zone. On the left, early time behavior, after excavation and emplacement. On the right, late time behavior, after full resaturation of the system (i.e., when all fractures are closed).

Figures 4-38 to 4-40 report on the abstractions of the EDZ (see Chapter 3.4.5). Figure 4-38 depicts an equivalent EDZ radius at which fracture density is approximately 100 fractures/m<sup>2</sup>. The abstracted EDZ equivalent radius is 3-3.5 meters depending on situ stress conditions. This result is coherent with that of Geomechanica (2013). Figure 4-39 summarizes the total equivalent specific axial fluxes of the EDZs abstracted with the radii in Figure 4-38. As observed, local conditions and strength parameters have some impact on the early time fluxes. The same conclusion arises from Figure 4-40, reporting on total equivalent porosity. However, local conditions and strength parameters have little impact on the late time specific fluxes. Note that the abstracted specific flux drops approximately 12 orders of magnitude in all cases. Finally, total porosity is not at all sensitive to local conditions and strength parameters (Figure 4-33).

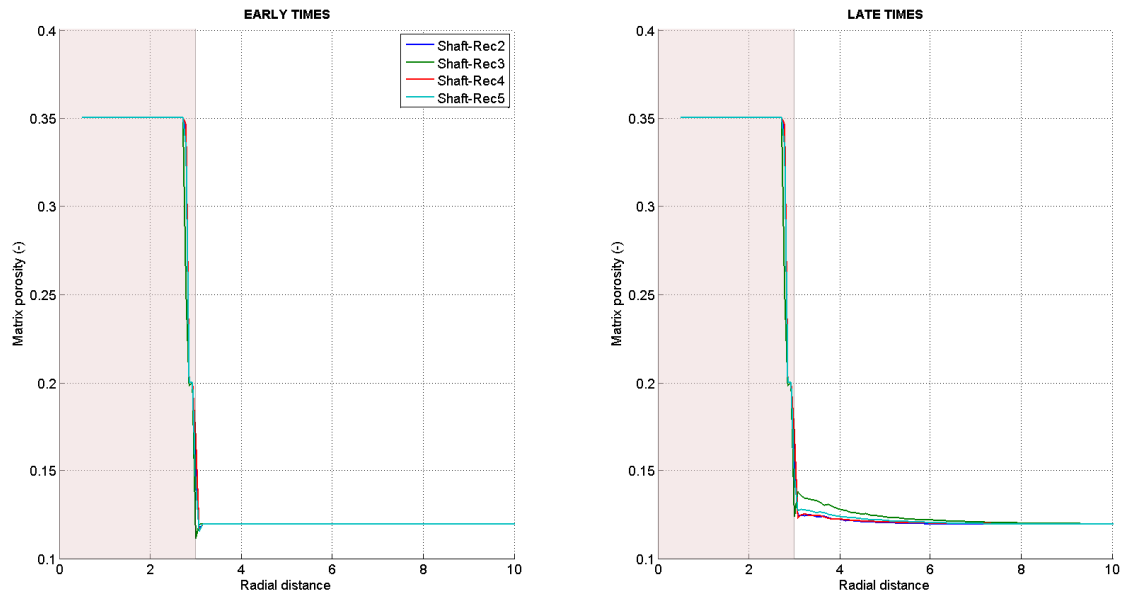


Fig. 4-37: Spatial distribution of matrix porosity of Shaft-Rec models. The inset depicts the buffer zone. On the left, early time behavior, after excavation and emplacement. On the right, late time behavior, after full resaturation of the system (i.e., assuming that all fractures are closed). Note that matrix porosity represents total porosity at late times.

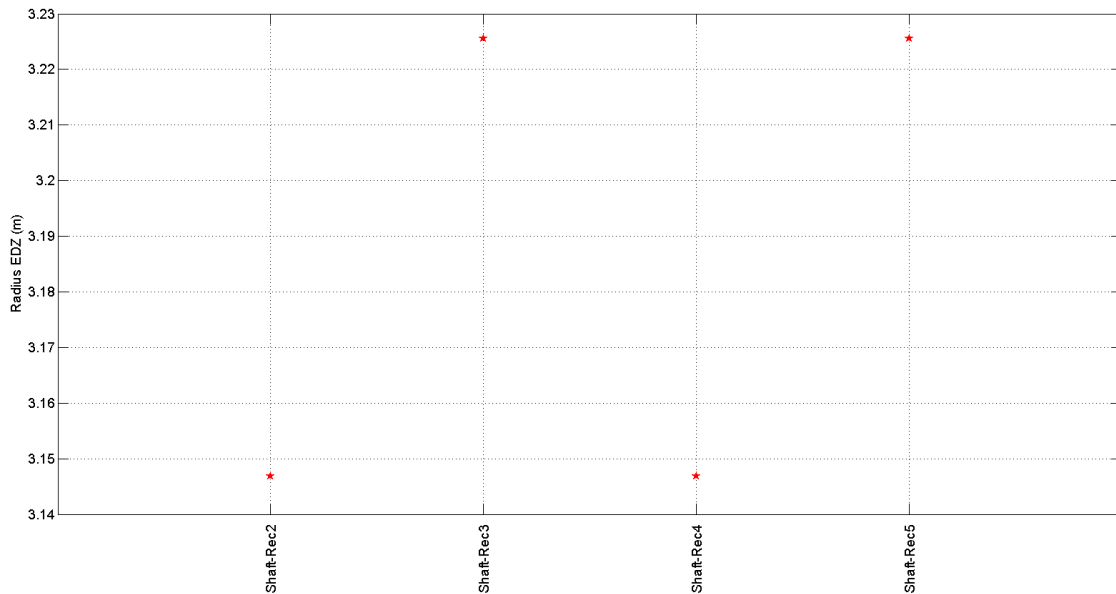


Fig. 4-38: Equivalent radius of the EDZ abstraction of Shaft-Rec models, defined as the radial distance at which fracture density drops to 10 fractures/m<sup>2</sup>.

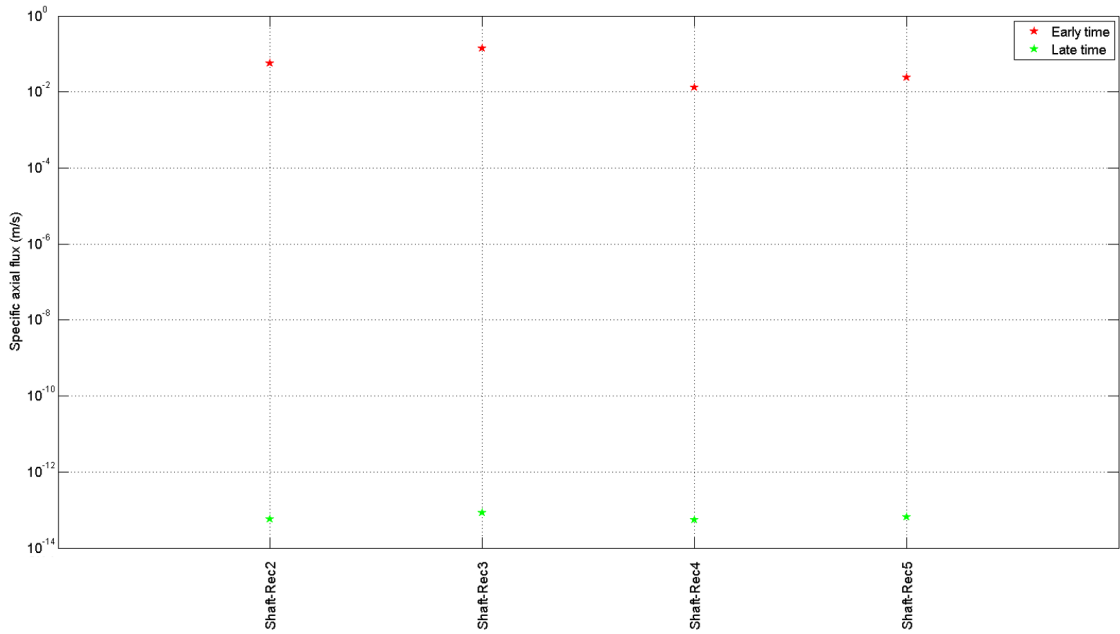


Fig. 4-39: Early and late time total equivalent specific fluxes of the abstracted Shaft-Rec models.

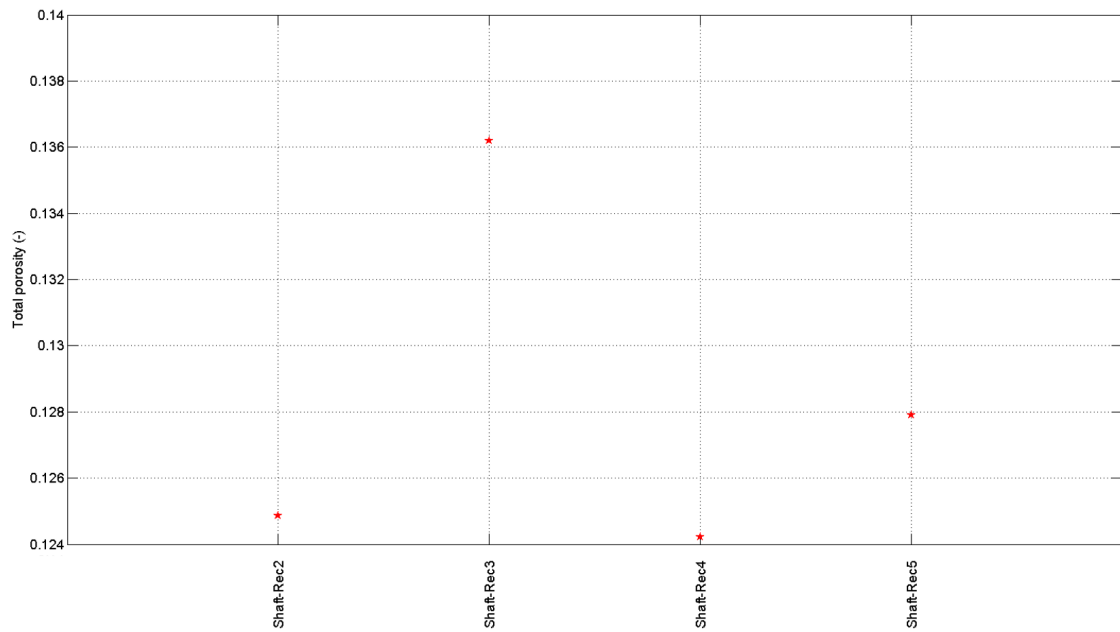


Fig. 4-40: Total equivalent porosity of the abstracted Shaft-Rec models.

#### 4.5 Transient behavior under resaturation conditions

Chapter 3.4.4 reports on the behavior of model HAA-01 under resaturation conditions. This section contains analog figures but using models HAA-02 and HAA-03. The results and conclusions are the same as those summarized in Chapter 3.4.4. Only results using Barton’s parameter  $\alpha = -0.4$  are presented. Figure 4-41 displays the number of fractures closed as a

function of time. As observed, all fractures are closed at late times. Despite the geometries of the EDZs of models HAA-01 to 03 are very different, the behavior in terms of rate of mechanical closure is quite similar because it mainly depends on the number of fractures. First, a steep slope ( $t > 0.1$  a) is observed. This corresponds to the mechanical closure of the fractures at the periphery of the EDZ. The resaturation steadily closes fractures closer to the gallery until all of them are closed ( $t \sim 5000$  a). The times at which the first inflexion point ( $\sim 0.1$  a) or the steady state ( $\sim 5000$  a) are observed depends to a great extent on the  $\alpha$  parameter, as discussed in Chapter 3.4.4.

Figure 4-42 reports on the spatial distribution of equivalent specific axial fluxes at different resaturation times. In this case, the spatial distributions of fluxes present a strong variability because they mainly depend on the geometry of the EDZ.

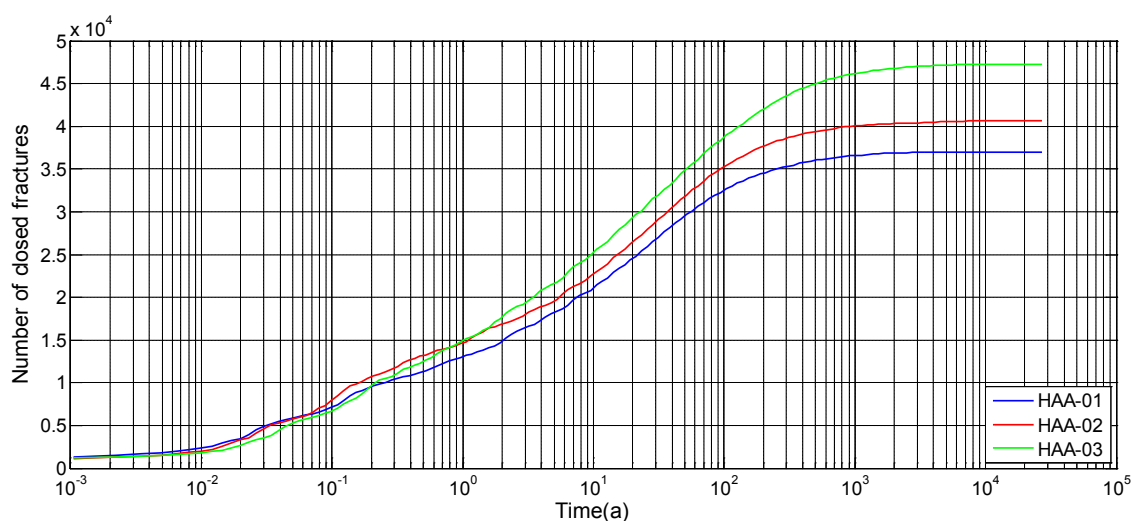


Fig. 4-41: Number of closed fractures vs. resaturation time. HAA-01 to 03 models

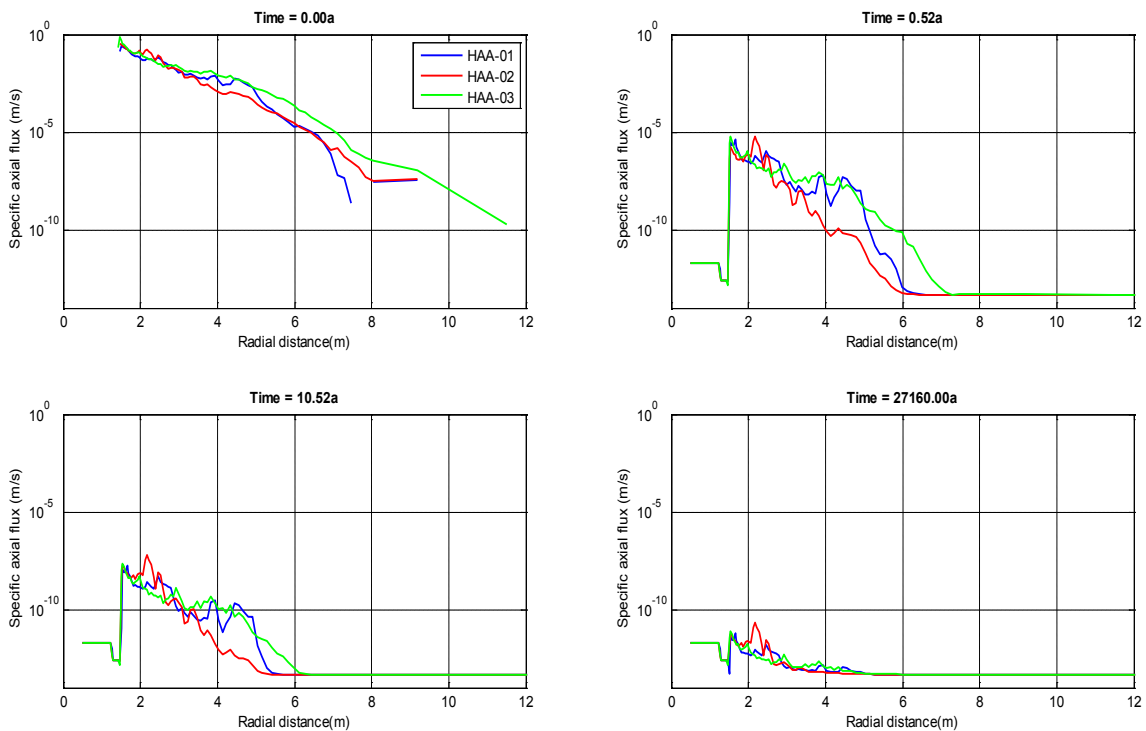


Fig. 4-42: Spatial distribution of equivalent specific axial fluxes at selected times. HAA-01 to 03 models.

#### 4.6 Evaluation of the results of the sensitivity analyses

Two sets of repository configurations have been considered, namely "HAA-models" for the SF/HLW emplacement tunnel and a circular opening for the vertical shaft. Reported results include:

- Summary statistics of the geometric properties of the FEMDEM simulations representing the EDZ.
- Plots of the FEMDEM and of its relevant geometric and hydraulic properties.
- Plots of the upscaled properties over a finite element mesh, namely total, fracture and matrix hydraulic conductivity and porosity, total hydraulic conductivity. All calculations presented here are carried out twice, i.e., at early times after excavation and emplacement and at late times after full resaturation of the system (assuming that all fractures are closed).
- The spatial distribution of equivalent parameters, i.e., hydraulic conductivity (or specific flux), porosity and fracture density.
- Abstracted models of the EDZ based on fracture density.
- The temporal evolution of the system under resaturation conditions.
- Sensitivity of the aforementioned scores to in situ stress conditions and strength parameters.

This section describes a methodology for an overall evaluation of the sensitivity study to provide guidance for the elaboration of abstracted EDZ representation in conventional SA tools. To this end, the late time profiles of effective porosity  $\phi_{EDZ}(r)$  and effective hydraulic conductivity  $K_{EDZ}(r)$  are subjected to further analyses. Firstly, averaged profiles  $\langle \phi_{EDZ}(r) \rangle$  and  $\langle K_{EDZ}(r) \rangle$  are derived for all SF/HLW runs and Shaft runs. Note that the arithmetic mean is adopted for the porosity profiles, whereas the geometric mean is used to estimate the averaged conductivity profiles.

In a second step, the average values of void volume  $\langle V_{EDZ} \rangle$  and total axial flux  $\langle Q_{EDZ} \rangle$  along the EDZ are calculated by integration:

$$\begin{aligned} \langle V_{edz} \rangle &= \int_{r_0}^{\infty} (\langle \phi_{EDZ}(r) \rangle - \phi_{matrix}) \cdot r \cdot dr \\ \langle Q_{edz} \rangle &= \int_{r_0}^{\infty} (\langle K_{EDZ}(r) \rangle - K_{matrix}) \cdot r \cdot dr \end{aligned} \quad (4-1)$$

were  $r_0$  represents the radius of the unlined tunnel. Eventually, the average void volume  $\langle V_{EDZ} \rangle$  and the corresponding total axial flux  $\langle Q_{EDZ} \rangle$  are used to define homogenized properties of the abstracted EDZ in terms of a relationship between the equivalent porosity / hydraulic conductivity  $\phi_{EDZ,equiv} / K_{EDZ,equiv}$  and the associated equivalent EDZ radius  $r_{equiv}$ :

$$\begin{aligned} \phi_{EDZ,equiv} &= \phi_{matrix} + \frac{\langle V_{edz} \rangle}{(r_{equiv}^2 - r_0^2) \cdot \pi} \\ K_{EDZ,equiv} &= K_{matrix} + \frac{\langle Q_{edz} \rangle}{(r_{equiv}^2 - r_0^2) \cdot \pi} \end{aligned} \quad (4-2)$$

The homogenized EDZ properties are reported in the following paragraphs for the HAA models and the Shaft models. Furthermore a summary of the key findings deduced from the sensitivity analyses is given.

#### 4.6.1 HAA-models (SF/HLW emplacement tunnel)

A total of 24 sensitivity runs of the HAA-model were analyzed. The compilation of all radial profiles of effective porosity and hydraulic conductivity at late times (i.e., after recovery of static formation pressure) reveals a quite moderate variability (Fig. 4-43), even though the extent and shape of the EDZ fracture patterns differed considerably (Geomechanica 2013). Close to the tunnel wall, the porosities are ranging between 0.14 and 0.22. The corresponding hydraulic conductivities are increased by 0.5 to 1 order of magnitude with respect to the intact rock matrix. At a distance of 2 tunnel radii (at 6 m), the rock properties are indistinguishable from the intact rock matrix.

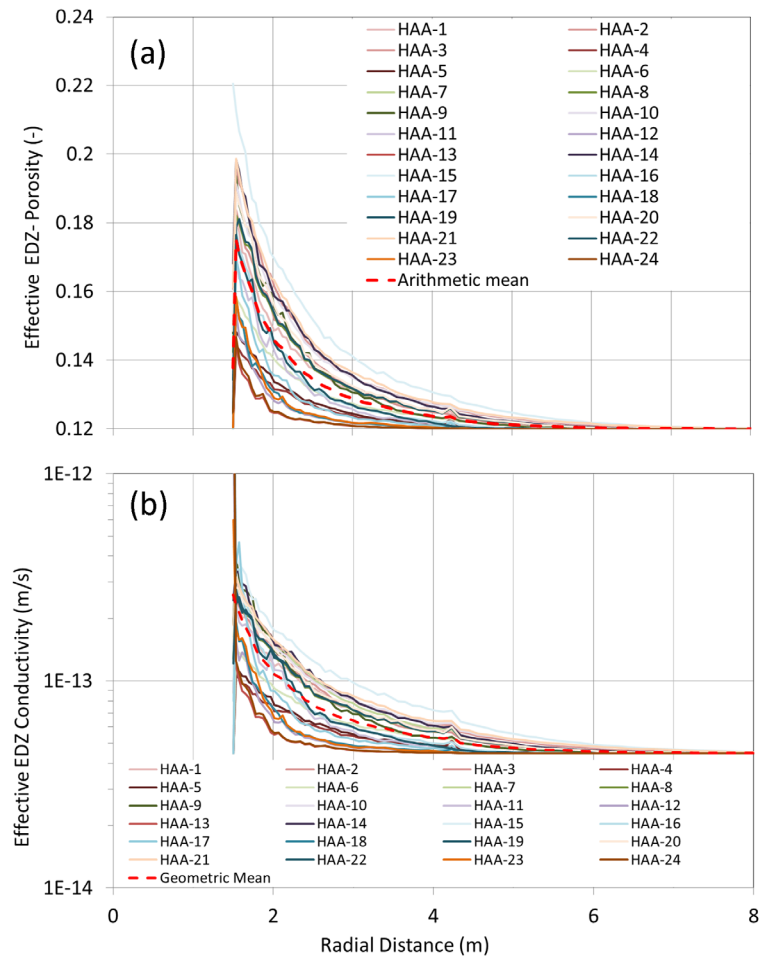


Fig. 4-43: Radial profiles of (a) effective porosity  $\phi_{EDZ,HAA-i}(r)$  and (b) effective hydraulic conductivity  $K_{EDZ,HAA-i}(r)$  of the 24 HAA simulations after recovery of static formation pressure (late times).

Average profiles  $\langle \phi_{EDZ}(r) \rangle$  (arithmetic mean) and  $\langle K_{EDZ}(r) \rangle$  (geometric mean) were derived from the effective porosity and conductivity profiles. These are depicted by dashed lines in Figure 4-43. The moderate spread of the individual profiles around the average profiles suggests that the average profiles can be regarded as representative ensemble means.

The averaged profiles were used for calculating the average void volume  $\langle V_{EDZ} \rangle$  and total axial flux  $\langle Q_{EDZ} \rangle$  according to Equation 4-1. In the final step the homogenized EDZ properties were derived according to Equation 4-2. Figure 4-44 displays the corresponding relationship between the equivalent EDZ radius  $r_{equiv}$  and the equivalent porosity  $\phi_{EDZ,equiv}$ , respectively hydraulic conductivity  $K_{EDZ,equiv}$ .

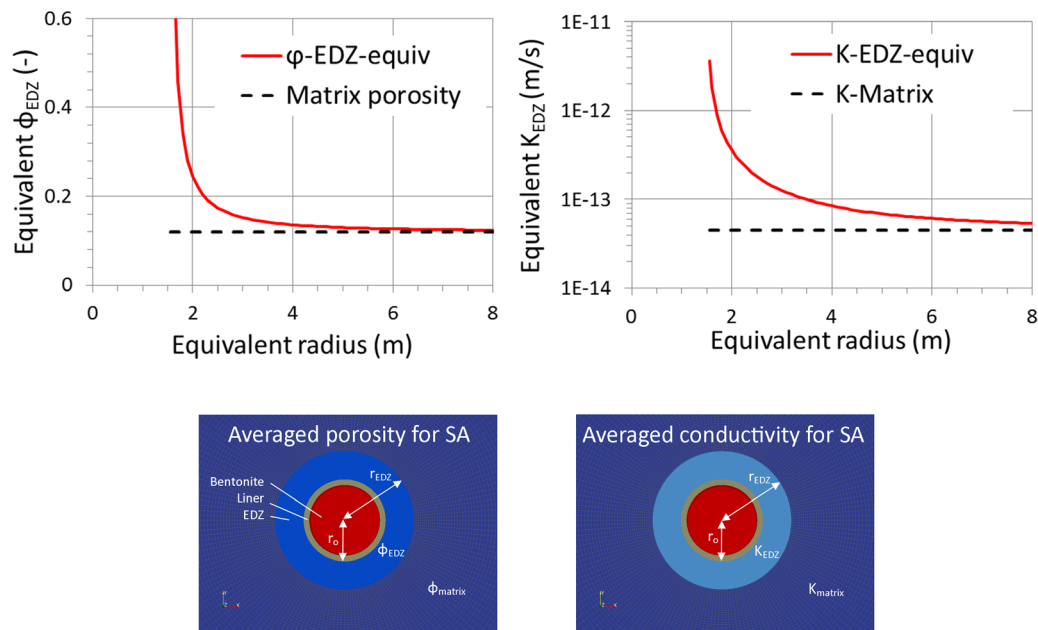


Fig. 4-44: Relationship between equivalent EDZ radius and homogenized porosity (upper left) and hydraulic conductivity (upper right), representative for of the HAA tunnel configuration.

In summary, the main findings with regard to the EDZ around the SF/HLW emplacement tunnel (HAA-models) are:

- Regardless of in situ stresses and other parameters, fracture density drops dramatically to negligible values at a radial distance of approximately 4 m (measured from the centre of the gallery). The total extension of the EDZ (i.e., where fracture density is zero) slightly depends on local conditions and strength parameters. A maximum extension of 6 to 8 m has been found, common to all HAA models. Conversely, the development and geometry of the EDZ is very sensitive to in situ stress conditions and strength parameters.
- Regardless of in situ stresses and other parameters, it has been observed that specific fluxes are initially very high (of the order of  $10^{-2}$  to  $10^0$  m/s) and drop dramatically due to fracture closure and swelling of the clayey minerals forming the matrix at late times (approximately 13 orders of magnitude). Overall, the spread of specific fluxes at the first meters of the EDZ depends on local stresses and strength parameters. It is worth to mention that the specific fluxes calculated here are overestimated because fracture density of the FEMDEMs is overestimated by a factor  $\sim 10$ .
- Initial fracture porosity is very high (app. 0.12 or 12%) due to the large aperture and length of the fracture patches defining the FEMDEM. This value drops to  $\sim 10^{-6}$  after resaturation of the system.
- Matrix porosity within the extension of the EDZ slightly increases due to swelling of the clayey minerals.
- Sensitivity to in-situ stresses: fracture density increases with horizontal stress, leading to increased fluxes.
- Sensitivity to core softening ratio: fracture density decreases as the stiffness of the core increases. This leads to reduced specific fluxes.

- Sensitivity to strength parameters: fracture density decreases with increasing strength parameters. This leads to reduced specific fluxes.
- Fracture density and specific flux are not very much sensitive to the elastic modulus of support.
- The presence of pre-existent faults favours the generation and development of drilling induced fractures, what leads to higher fracture densities and specific fluxes.

#### 4.6.2 Shaft models

A total of 9 sensitivity runs of the shaft model were analyzed. The compilation of all radial profiles of effective porosity and hydraulic conductivity at late times (i.e., after recovery of static formation pressure) reveals even lower variability than the HAA model (Fig. 4-45). Close to the shaft wall, the porosities range between 0.13 and 0.16. The corresponding hydraulic conductivities are increased less than 1 order of magnitude with respect to the intact rock matrix. At a distance of 2 tunnel radii (at 12 m), the rock properties are indistinguishable from the intact rock matrix.

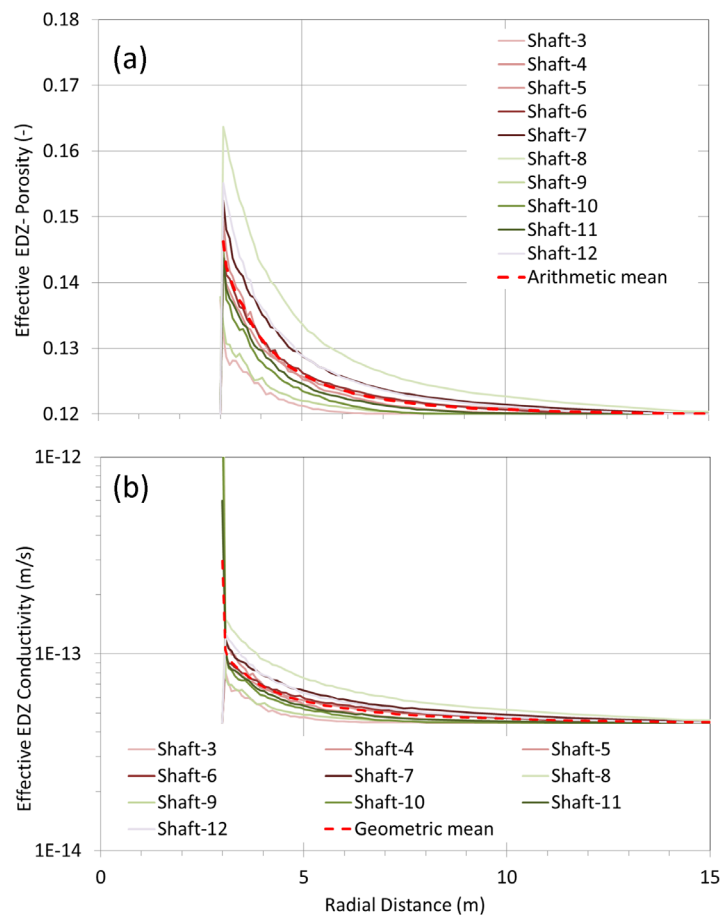


Fig. 4-45: Radial profiles of effective porosity  $\phi_{EDZ,Shaft-i}(r)$  and effective hydraulic conductivity  $K_{EDZ,Shaft-i}(r)$  of 9 shaft simulations models after recovery of static formation pressure (late times).

Average profiles  $\langle \phi_{EDZ}(r) \rangle$  (arithmetic mean) and  $\langle K_{EDZ}(r) \rangle$  (geometric mean) were derived from the effective porosity and conductivity profiles. As for the HAA models, the moderate spread of the individual profiles around the average profiles suggests, that the average profiles can be regarded as representative ensemble means. The averaged profiles were used for calculating the average void volume  $\langle V_{EDZ} \rangle$  and total axial flux  $\langle Q_{EDZ} \rangle$  along the vertical Shaft according to Equation 4-1. In the final step the homogenized EDZ properties were derived according to Equation 4-2. Figure 4-46 displays the corresponding relationship between the equivalent EDZ radius  $r_{equiv}$  and the equivalent porosity  $\phi_{EDZ,equiv}$ , respectively hydraulic conductivity  $K_{EDZ,equiv}$ .

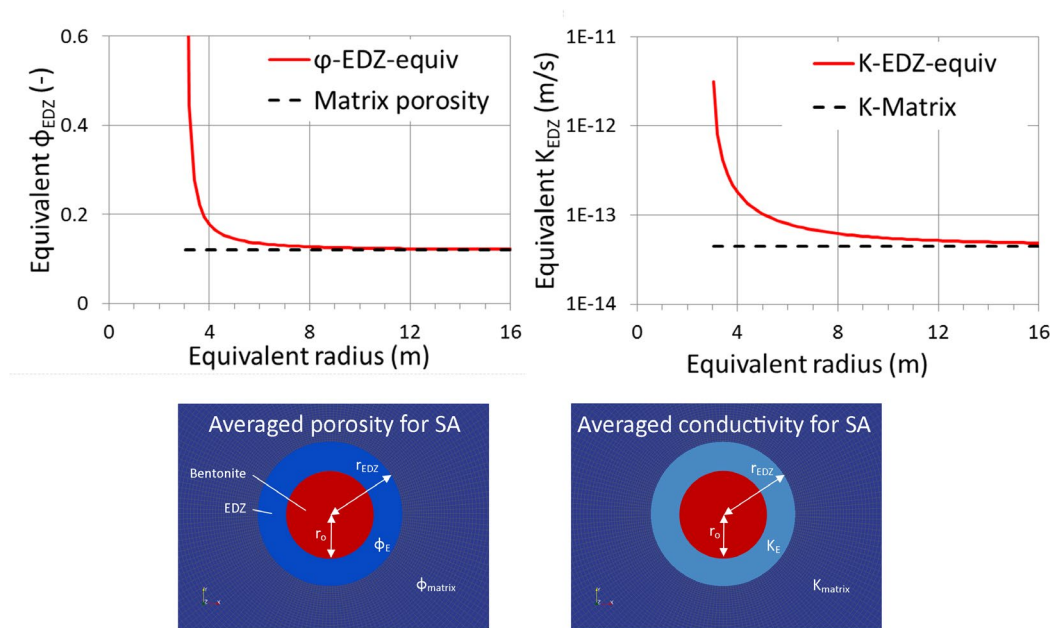


Fig. 4-46: Relationship between equivalent EDZ radius and homogenized porosity (upper left) and hydraulic conductivity (upper right), representative for of the Shaft configuration.

The main conclusions with regard to the shaft models are:

- The number of fractures at short radial distances, i.e., close to the liner, depends greatly on stress conditions and strength parameters under which the FEM was generated. The observed variability is greater than that of the HAA models due to the change in the stress regime (purely horizontal to purely vertical).
- A characteristic common to all Shaft FEMDEMs is that fracture density drops dramatically to almost negligible values after a radial distance  $\sim 10$  m (with respect to the center of the gallery). The total extension of the EDZ (i.e., zero fracture density) is almost the same for all FEMDEMs,  $\sim 12$  m. As a conclusion, the development and geometry (see corresponding FEMDEM figures in Appendix 1) of the EDZ greatly depends on in situ stress conditions and strength parameters. Conversely, the extension of the EDZ for the Shaft models is not sensitive to local conditions.
- Regardless of in situ stress conditions and strength parameters, we observe that:
- Fluxes are very high at early times ( $10^{-1}$  to  $10^0$  m/s) due to the high transmissivity of the system. A similar result was also observed in the HAA models.

- Specific flux drops more than 13 orders of magnitude at late times.
- Overall, the spread of the specific fluxes is less than 1 order of magnitude at late times. Thus, specific flux is somewhat sensitive to in situ stress and strength parameters, but less sensitive than HAA models.
- All simulations yield an EDZ extension of 10 to 12 m with respect to the center of the gallery. Thus, the total extension of the EDZ is not very sensitive to local conditions. It is worth to mention that the effective extension of the EDZ, through which the main contribution of the flux circulates, strongly depends on local conditions. This is observed in the wide spread of specific fluxes at radial distances between 3 and 7 meters.
- Initial fracture porosity is relatively low, with values between 0.01 and 0.05 (1-5%). These values are substantially smaller than those of initial fracture porosity of the HAA models (~ 12%).
- Overall, the radius of the abstracted EDZ is between 3 and 12 m. This result is coherent to that in Geomechanica (2013). Local conditions and strength parameters have minor impact on the absolute value of specific fluxes. However, the surface across which the specific flux circulates is strongly affected by small variations in in situ stresses and strength parameters. Local conditions and strength parameters have little impact on the late time specific fluxes. Equivalent total porosity is not much sensitive to local conditions and strength parameters.
- An increase in total stress leads to a substantial decrease in fracture density and, correspondingly, in specific axial flux.
- Increasing the strength parameters leads to smaller fracture densities and, correspondingly, to smaller specific axial fluxes.

#### 4.7 Envisaged extensions of the approach

The study presented here has been carried under simplifications of geometry (i.e., the model is 2D and the geometry of the gallery is circular). However, the suggested modeling and abstraction strategies are general and can be applied to different geometries and dimensions without much extra-programming (simply the computational effort will increase). Therefore, this work represents a step forward in the modeling and abstraction of the Excavation Damaged Zone associated with the emplacement of a nuclear waste repository. Some recommendations for future studies are outlined below:

- The temporal behavior of the system under resaturation is still not known with accuracy. The modifications made to Barton's model presented here need to be properly investigated. Specially, the parameter  $\alpha$  controlling the rate of fracture closure needs to be bracketed. To that end, the interpretation of lab experiments reproducing the resaturation of the system is suggested.
- Monte Carlo analysis of the uncertainties caused by the unknown geometry of the EDZ: the existing models can be considered as "mean" geometries of the EDZ under different local conditions. These "mean" geometries can be updated by a Monte Carlo procedure to yield many realizations of the EDZ under the same field conditions. These realizations would report on the uncertainty of axial fluxes caused by an accurate knowledge of the geometry of the EDZ.

The existing 2D vertical sections can be used to condition the geometry of a 3D model of the gallery. To that end, multiple equally likely realizations obtained by multiple point geostatistics will allow to calculate the axial fluxes in a less simplified manner.

## 5 Summary and conclusions

### Development of a hydro-mechanical modelling framework for EDZ abstraction

The EDZ around the backfilled underground structures of a geological repository represents a possible release path for radionuclides as well as a possible escape route for corrosion and degradation gases which needs to be addressed adequately in safety assessments. However, the hydro-mechanical phenomena and processes, associated with the creation of the EDZ during construction and the evolution thereof during operational times and after backfilling of the underground structures are of great complexity, preventing a detailed representation of the EDZ in conventional SA modelling tools. Instead, simplified EDZ models are required, able to mimic the safety relevant functional features of the EDZ.

In this study a versatile workflow has been elaborated, capable of representing the key features of the EDZ in an abstracted manner according to the needs in safety assessment:

- Realistic representations of the EDZ in terms of fracture mode, shape and extent are simulated with a fracture mechanics model.
- The derived discrete fracture network model is converted into a hybrid hydraulic model, which displays both the features of a hydraulic fracture network and a continuum model of the non-fractured rock matrix.
- A heuristic hydro-mechanical process model is adopted to simulate the well-established EDZ phenomena such as fracture self-sealing and swelling of the non-fractured rock matrix. The implementation of the hydro-mechanical processes is based on classical constitutive frameworks of elasto-plasticity.
- The evolution of hydraulic conductance of the EDZ is calculated as a function of pore pressure recovery. Simplified representations of the EDZ properties are given in terms of effective radius, effective hydraulic conductivity and effective porosity.

The newly developed workflow has been subjected to comprehensive evaluations and consistency checks, in particular by comparing the simulation results with existing empirical evidence and with experimental results from large scale in-situ tests. The main findings are highlighted here:

- Comparison of the simulated fracture patterns with fracture statistics from Mont Terri and other underground rock laboratories suggests a good overall agreement of the shape and extent of the EDZ (see Figs. 2-3 & 2-4). However, the FEMDEM simulations seem to overestimate the fracture intensity to some extent (typically less than half and order of magnitude). Improved calibration procedures for rock strength are suggested to overcome those deficiencies.
- The empirical porosity-permeability relationship (Kozeny-Carman) and the fracture closure law (Barton's model) adopted in the heuristic modelling approach have been confirmed by experimental evidence from laboratory and in-situ tests (Figs. 2-10 & 2-12).

- The temporal evolution of effective hydraulic conductance of the EDZ matches the available empirical evidence very well. Thus, the predicted high fracture transmissivities immediately after tunnel excavation have been observed in many underground structures (see Fig. 2-5). Furthermore, the decrease of fracture transmissivity with time as reported in the context of the Mont Terri investigation programme (see Fig. 2-13), is largely consistent with the modelling results. Last, but not least, an excellent qualitative agreement is seen between the simulated temporal evolution of effective hydraulic EDZ conductivity (Fig. 3-21) and the so-called "sealing index" which has been measured as part of the Mont Terri / HG-A project (Fig. 2-16).

### **Homogenized hydraulic EDZ parameters for SA**

Evaluations of the hydraulic properties of the EDZ were conducted for a wide range of repository settings, covering sensitivity analyses with regard to repository depth, stress state, rock strength, tunnel shape and design of the lining. The overall assessment of the simulations indicates a marked change in hydraulic conductance of the EDZ after repository closure, which is controlled by the evolution of pore pressure in the vicinity of the backfilled underground structures. During the early times, the EDZ conductance is dominated by the high transmissivity of the fractures. When comparing the different simulation cases, significant variability is seen in the equivalent fracture density (Figure 4-2) and, as a consequence, in the calculated specific flux (Fig 4-3, left), indicating that the hydraulic conductance of the EDZ is very sensitive to its shape and lateral extent. The early time with dominating fracture flow is restricted to a period between 10 and 100 years (Fig. 3-21). In the course of the pore pressure recovery the fractures close progressively and the non-fractured rock matrix swells by water uptake, leading to an increase of porosity and hydraulic conductivity. After around 1000 years, it is to be expected that the bulk of the fractures is tight and the hydraulic conductance is dominated by the rock matrix (late times). The late time conductance of the EDZ is the essentially required parameter in the context of longterm safety assessment and will be discussed in the following paragraphs.

During late times the hydraulic conductance of the EDZ has decreased by many orders of magnitude. When comparing the different simulation cases, the variability of specific flux (Fig 4-3, right) is very modest with a spread of less than an order of magnitude. Furthermore, the radial extent of the EDZ in the late times is very similar for all cases, ranging between 2 and 6 m for the HAA models. A minor effect is yet seen, indicating a slight dependence of EDZ conductance on the initial extent of the EDZ, as seen in the comparison of the cases HAA-03 and HAA-04 in Fig. 4-10 (impact of core softening ratio).

Evaluations of the late time conductance of the EDZ were carried out for the SF/HLW tunnels and for the shaft. In this context homogenized porosity and conductivity values and the corresponding EDZ radius were provided as simplified EDZ representations for safety assessment applications (Figs. 4-44 and 4-46). Key conclusions are summarized here:

- At late times (i.e. after recovery of static formation pressure) the EDZ around the backfilled underground structures of a deep geological repository in the Opalinus Clay is restricted to a radial zone with a thickness of less than 2 diameters.
- Significant enhancement of hydraulic conductivity is observed only in a zone with a thickness of less than half of a tunnel diameter. The corresponding enhancement of effective hydraulic conductivity in this zone is less than 1 order of magnitude with respect to the intact rock matrix. Furthermore, the corresponding increase of porosity in this zone is less than 20% of the porosity of the intact rock matrix.

## 6 References

- Alheid H.J., Aranyosy J.F., Blümling P., Hoteit N., Van Geet M. (2007): EDZ development and evolution – State of the art. NF-PRO. Contract Number F16W-CT-2003-02389
- ANDRA (2005): Dossier 2005 Argile. Synthesis: Evaluation of the Feasibility of a Geological Repository in an Argillaceous Formation, Meuse/Haute Marne Site. Paris, France.
- Armand, G., T. Doe, M. Piédevache and G. Chavane (2004): Permeability measurements in the excavation damaged zone in the Opalinus Clay at Mont Terri Rock Laboratory, Switzerland. Proceedings 57th Canadian Geotechnique Conference. Paper G15-453.
- Baechler, S., Lavanchy, J.M., Armand, G. & Cruchaudet, M. (2011): Characterisation of the hydraulic properties within the EDZ around drifts at level -490 m of the Meuse/Haute-Marne URL: a methodology for consistent interpretation of hydraulic tests. *Journal of Physics and Chemistry of the Earth*, 36, 1922-1931, doi:10.1016/j.pce.2011.10.005.
- Bandis, S.C., Lumsden, A.C. & Barton, N.R. (1983): Fundamentals of rock joint deformation. *Int. J. Rock Mech. Min. Sci. & Geomech. Abstr.* Vol. 20, No. 6.
- Beauheim (2013): Hydraulic conductivity and head distributions in the host rock formations of the proposed siting regions. Nagra Arbeitsbericht NAB 13-13. Nagra, Wettingen, Switzerland.
- Blümling, P., F. Bernier, P. Lebon and C.D. Martin (2007): The excavation damaged zone in clay formations time-dependent behaviour and influence on performance assessment. *Physics and Chemistry of the Earth* 32(8-14), 588-599.
- Bock, H., Dehandschutter, B., Martin, C.D., Mazurek, M., de Haller, A., Skoczylas, F., Davy, C. (2010): Self-sealing of fractures in argillaceous formations in the context of geological disposal of radioactive waste. OECD, NEA No. 6184.
- Bossart, P., P.M. Meier, A. Moeri, T. Trick and J.C. Mayor (2002): Geological and hydraulic Characterization of the excavation disturbed zone in the Opalinus Clay of the Mont Terri Rock Laboratory. *Engineering Geology* 66, 19-38.
- Bossart, P. and M. Thury (Eds) (2008): Mont Terri Rock Laboratory Project, Programme 1996 to 2007 and Results, Rep. Swiss. Geological Survey 3, Wabern, Switzerland.
- Carman P.C. (1937): Fluid flow through granular beds. *Transactions, Institution of Chemical Engineers*, London, 15: 150-166, 1937.
- Carman P.C. (1956): *Flow of gases through porous media*. Butterworths, London, 1956.
- De Marsily, G. (1986): *Quantitative hydrogeology*. Academic Press, New York.
- Ferrari, A., Favero, V., Manca, D., Laloui, L. (2013): Geotechnical characterization of core samples from the geothermal well Schlattigen SLA-1. Nagra Arbeitsbericht NAB 12-50, Nagra, Wettingen, Schweiz.
- Gautschi, A. (2001): Hydrogeology of a fractured shale (Opalinus Clay): Implications for the deep disposal of radioactive wastes. *Hydrogeol. J.* 9, 97-107.

- Geomechanica (2013): Extent and shape of the EDZ around underground structures of a geological repository for radioactive waste – A sensitivity study for the candidate host rocks in the proposed siting regions in Northern Switzerland. Nagra Arb. Ber. NAB 13-78, Nagra, Wettingen, Schweiz.
- Hawkins, I.R., Swift, B.T., Hoch, A.R., J. Wendling (2011): Comparing flows to a tunnel for single porosity, double porosity and discrete fracture representations of the EDZ. Elsevier, Physics and Chemistry of the Earth 36, pp. 1990-2002.
- Horseman, S.T., Higgo J.J.W., Alexander J., Harrington J.F. (1996): Water, Gas, and Solute Movement through Argillaceous Media. NEA Working Group on Measurement and Physical Understanding of Groundwater Flow Through Argillaceous Media. Report CC-96/1.
- Jackson C.P., A.R. Hoch and S. Todman (2000): Self-consistency of a heterogeneous continuum porous medium representation of a fractured medium. Water Resour. Res., 36(1), 189.
- Kozeny J. (1927): "Über kapillare Leitung des Wassers im Boden." Sitzungsber Akad. Wiss., Wien, 136(2a): 271-306, 1927.
- Lanyon G W. (2011): Excavation Damaged Zones Assessment. NWMO Technical Report DGR-TR-2011-21.
- Lanyon, G.W., Senger, R. (2011): A Structured Approach to the Derivation of Effective Properties for Combined Water and Gas Flow in the EDZ, Transp. porous media, 1–18.
- Marschall, P., M. Distinguin, H. Shao, P. Bossart, C. Enachescu, and T. Trick (2006): Creation and evolution of damage zones around a microtunnel in a claystone formation of the Swiss Jura mountains, in SPE International Symposium of Formation Damage Control, SPE.
- Marschall, P., Lanyon, B., Gaus, I., Rüedi, J. (2013): FORGE D4-16: Gas transport processes at Mont Terri Test Site (EDZ and host rock)-Field results and conceptual understanding of self sealing processes. [www.FORGEproject.org](http://www.FORGEproject.org).
- Martin, C.D. (1997): Seventeenth Canadian Geotechnical Colloquium: The effect of cohesion loss and stress path on brittle rock strength. Canadian Geotechnical Journal 34(5), 698-725.
- Martin, C.D., Lanyon, G.W. (2003): EDZ in clay shale: Mont Terri. Mont Terri Techn. Rep. 2001, 1. With contributions from P. Bossart and P. Blümling.
- Matray, J., S. Savoye and J. Cabrera (2007): Desaturation and structures relationships around drifts excavated in the well-compacted Tournemire's argillite and their impact on the hydraulic head profiles. Engineering Geology 90, 1-16
- Nagra (2002): Projekt Opalinuston – Synthese der geowissenschaftlichen Untersuchungsergebnisse. Entsorgungsnachweis für abgebrannte Brennelemente, verglaste hochaktive sowie langlebige mittelaktive Abfälle. Nagra Technical Report NTB 02-03, Wettingen, Switzerland.

- Nagra (2004): Effects of post-disposal gas generation in a repository for spent fuel, high-level waste and long-lived intermediate level waste sited in Opalinus Clay. Nagra Technical Report NTB 04-06, Nagra, Wettingen, Switzerland.
- Nagra (2010): Beurteilung der geologischen Unterlagen für die provisorischen Sicherheitsanalysen in SGT Etappe 2. Nagra Technischer Bericht NTB 10-01. Nagra, Wettingen, Switzerland; 2010.
- Romero, E., Gómez, R. (2013): Water and air permeability tests on deep core samples from Schlattingen SLA-1 borehole. Nagra Arb. Ber. NAB 13-51. Nagra, Wettingen, Switzerland.
- Senger, R., Papafotiou, A., Marschall, P. (2013): Gas related property distributions in the proposed host rock formations of the candidate siting regions in Northern Switzerland and in the Helvetic Zone. Nagra Arb. Ber. NAB 13-83. Nagra, Wettingen, Switzerland.
- Shao, H., Schuster, K., Sönke, J., Bräuer, V. (2008): EDZ development in indurated clay formations—In situ borehole measurements and coupled HM modelling. *Physics and Chemistry of the Earth* 33, 388-395.
- Swiss Federal Office of Energy (SFOE). Sectoral Plan for Deep Geological Repositories, Conceptual Part. Swiss Federal Office of Energy, Bern, Switzerland, 2008.
- Thury, M. & Bossart, P. (1999): Mont Terri rock laboratory. Results of the hydrogeological, geochemical and geotechnical experiments performed in 1996 and 1997. Geological Report No. 23, Swiss National Hydrological and Geological Survey, Bern, 191 p.
- Tsang, C.F., F. Bernier and C. Davies (2005): Geohydromechanical processes in the Excavation Damaged Zone in crystalline rock, rock salt, and indurated and plastic clays—in the context of radioactive waste disposal. *International Journal of Rock Mechanics and Mining Sciences* 42(1), 109-125.
- Wileveau, Y. and Bernier, F. (2008): Similarities in the hydromechanical response of Callovo-Oxfordian clay and Boom Clay during gallery excavation. *Physics and Chemistry of the Earth* 33, 343-349.
- Witherspoon P.A., Wang J.S.Y., Iwai K., Gale J.E. (1980): Validity of cubic law for fluid-flow in a deformable rock fracture. *Water Resour. Res.* 16:1016-1024.
- Yang, Y.L., Aplin, A.C. (2010): A permeability – porosity relationship for mudstones. *Marine and Petroleum Geology* 27(8): 1692-1697.
- Yong S. (2007): A three-dimensional analysis of excavation-induced perturbations in the Opalinus Clay at the Mont Terri Rock Laboratory, PhD thesis, ETH Zurich, 180 pp.
- Yong S., Kaiser P.K., Loew S. (2010): Influence of tectonic shears on tunnel-induced fracturing. *International Journal of Rock Mechanics and Mining Sciences*, 47: 984-907.



## A Description of output files in the digital appendix

A folder name "Digital\_Appendix" is appended to this manuscript. It contains two main sub-folders named "HAA models" and "Shaft models". Each of these contains a number of sub-folders corresponding to the simulations listed in Tables 4-2 and 4-3. For a given simulation, e.g., HAA-01, the sub-folder contains the following files:

- HAA-01\_FEMDEM.vtk: a vtk standard file containing the following properties of the FEMDEM (recommended visualization option in Paraview as "Wireframe"):
  - break\_mode: 1 tensile, 2 shearing, 3 torsion
  - length: fracture length in mm
  - inclination: fracture inclination in °
  - area: fracture area in mm<sup>2</sup>
  - aper\_ini: initial fracture aperture in mm
  - aper\_irred: constant irreducible aperture =  $8.9 \cdot 10^{-5}$  mm
  - log10(Tf\_ini): log10 of initial fracture transmissivity (in m<sup>2</sup>/s)
  - log10(Tf\_irred): log10 of irreducible fracture transmissivity (in m<sup>2</sup>/s)
  - frac\_id: identifier of fracture (as in Geomechanica files).
- HAA-01\_GridProps.vtk: a vtk standard file containing the gridded properties of the FEMDEM (recommended visualization option in Paraview as "Surface"):
  - Kf\_ini: initial hydraulic conductivity of fractures in m/s. In the following value -666 means that the element is not intersected by fractures, i.e., the value does not apply. A filter is recommended for visualization purposes in such case.
  - Kf\_end: late time hydraulic conductivity of fractures in m/s.
  - km\_ini: initial hydraulic conductivity of matrix in m/s.
  - km\_end: late time hydraulic conductivity of fractures in m/s.
  - Conductance\_ini: initial total hydraulic conductivity in m/s.
  - Conductance\_end: late time total hydraulic conductivity in m/s.
  - phif\_ini: initial fracture porosity.
  - phif\_end: late time fracture porosity.
  - phim\_ini: initial matrix porosity.
  - phim\_end: late time matrix porosity.
  - TotalPorosity: total porosity. Note that it does not vary in time.
  - NCounts: number of fractures intersecting each element.
  - P21: sum of lengths of fractures intersecting an element divided by element area.
  - Fractdens: number of fractures per unit area of the element.
  - cell\_code: element flag indicating the type of material (see Table 3-2).

- Abstraction\_EDZ\_ini.txt and Abstraction\_EDZ\_end.txt: text files containing the EDZ abstraction at early times after excavation and emplacement and at late times after full resaturation of the system. Each file contains (1) the equivalent radius of the EDZ, (2) the equivalent hydraulic conductivity and (3) the equivalent porosity.
- Equiv\_K\_Phi\_q.xlsx: An Excel table containing the integrated equivalent values. Columns are:
  - radius : equivalent radius of the rings in m
  - qaxial\_tot : equivalent total axial flux in m/s at early times
  - qaxial\_tot\_irred : equivalent total axial flux in m/s at late times
  - phitot : total porosity
  - fracedens : fracture density (number of fractures per unit area of the ring)
  - qaxial\_f : equivalent total axial flux at fracture only in m/s at early times
  - qaxial\_f\_irred : equivalent total axial flux at fracture only in m/s at late times
  - phif : equivalent fracture porosity at early times
  - phif\_irred : equivalent fracture porosity at late times
  - phim\_ini : equivalent matrix porosity at early times
  - phim\_latetime : equivalent matrix porosity at late times

An additional subfolder called "Resaturation" contains the temporal evolution of grid properties and pressure. All files are vtk and the animations can be easily rendered by Paraview. Types of files are:

- DFN\_timestep.vtk: a sequence of vtk files (recommended representation in Paraview as "Wireframe") containing the following scalar fields:
  - aper: fracture aperture in mm
  - log10T: log10 fracture transmissivity in m<sup>2</sup>/s
  - frac\_close: boolean variable (1 = fracture closed)
- GridProps\_timestep.vtk: gridded properties at current time step. The structure of the file is similar to that described above (file HAA-01\_GridProps.vtk)
- Pressure\_timestep.vtk: pressure at mesh nodes in MPa.

## B Two-phase scoping calculations on de- and resaturation of EDZ and buffer

### B-1 Problem description

An open gallery exhibits atmospheric pressure conditions during and early after excavation. Hence, the EDZ undergoes a desaturation process, in which fractures are partly filled with air and water leaks to the open gallery. After repository closure, the canisters and the buffer (bentonite) are installed and resaturation of fractures and buffer begins. Initially the pore space of the buffer is also partially saturated (so are the fractures forming the EDZ). Therefore, the buffer also fills up with water coming from the host rock. Not until the buffer is completely saturated pressure recovery takes place. In order to quantify the duration of this initial resaturation phase scoping two-phase flow simulations have been carried out utilizing the software TOUGH2.

### B-2 Conceptual model

The calculations are carried out for the EDZ model case HAA-14. The spatial distribution of initial axial hydraulic conductivity, as derived from fracture data, is displayed in Fig. A3.1. Regarding two-phase flow parameters the *van Genuchten* model is applied with typical values for Opalinus clay and (Nagra) bentonite. Within the EDZ, capillary pressures are scaled according the *Leverett* approach.

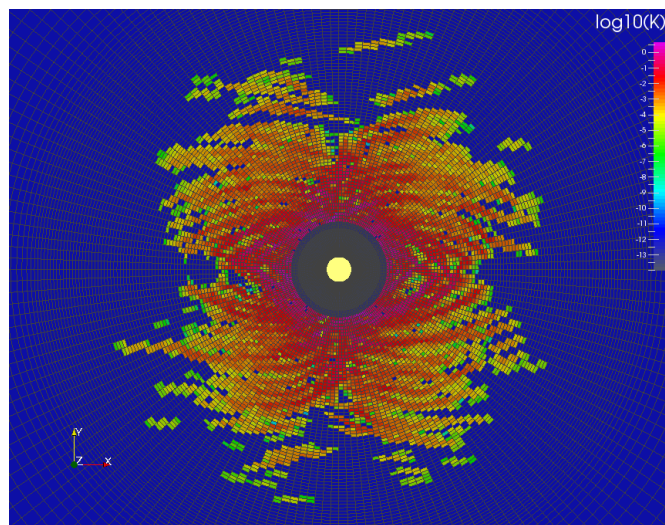


Fig. A3.1: Distribution of initial hydraulic conductivity.

### B-3 Desaturation of fractures

Initially, the open tunnel has atmospheric conditions so that air invades the pore space of the EDZ fractures. This phase is modelled by imposing atmospheric single phase (gas) conditions along the tunnel wall. Fig. A3.2 illustrates the temporal evolution of gas saturation. This process takes place during a few days only. The pressure drop from static to atmospheric pressure in all the fractures is even one order of magnitude faster (not shown).

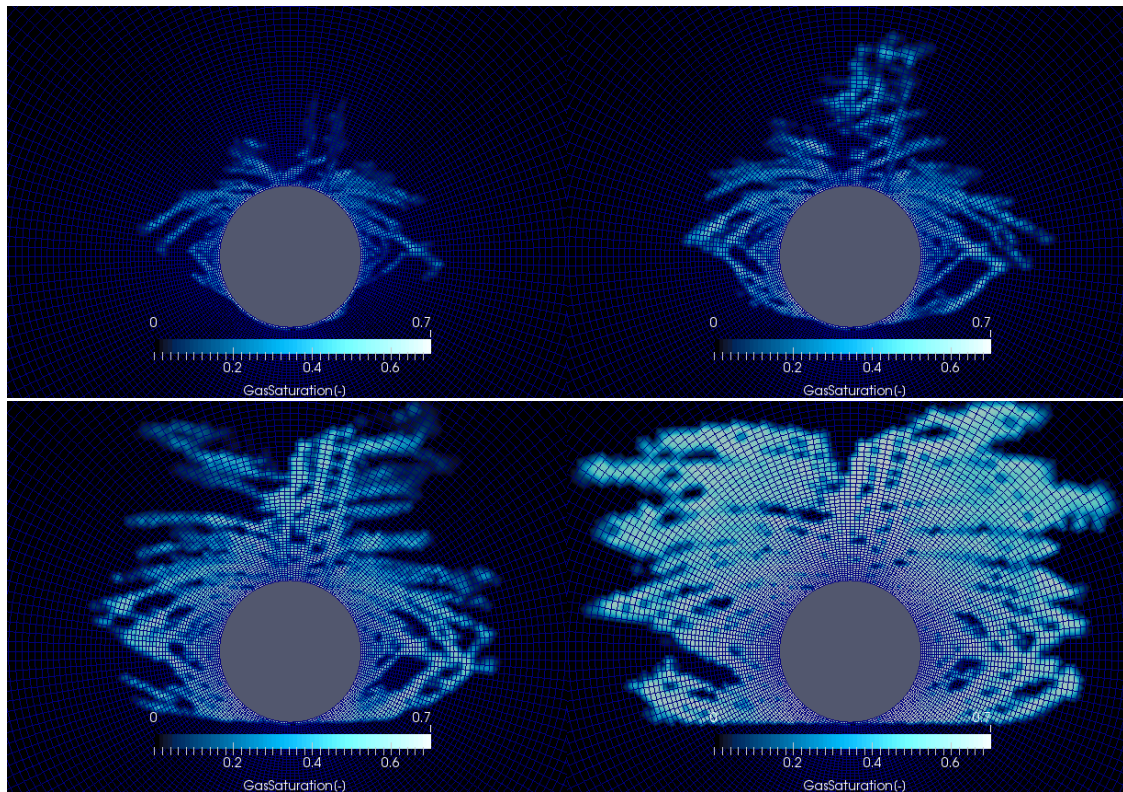


Fig. A3.2: Temporal evolution of fracture desaturation.

#### **B-4 Resaturation and pressure recovery**

Resaturation is simulated by considering the bentonite as an unsaturated zone with hydraulic properties given in Section 3 of the main study. The initial water saturation is assumed to be 45% in this case (although it can be lower in practice). Fig. A3.3 displays the temporal evolution of pressure within the bentonite. In this simulation the pore space is completely filled up after 20 years, so that pressure build-up to static condition begins. Complete recovery has not been reached after the simulation time of 10'000 years with the parameters used in this calculation. This is not the case when mechanical closure of fractures is also taken into account.

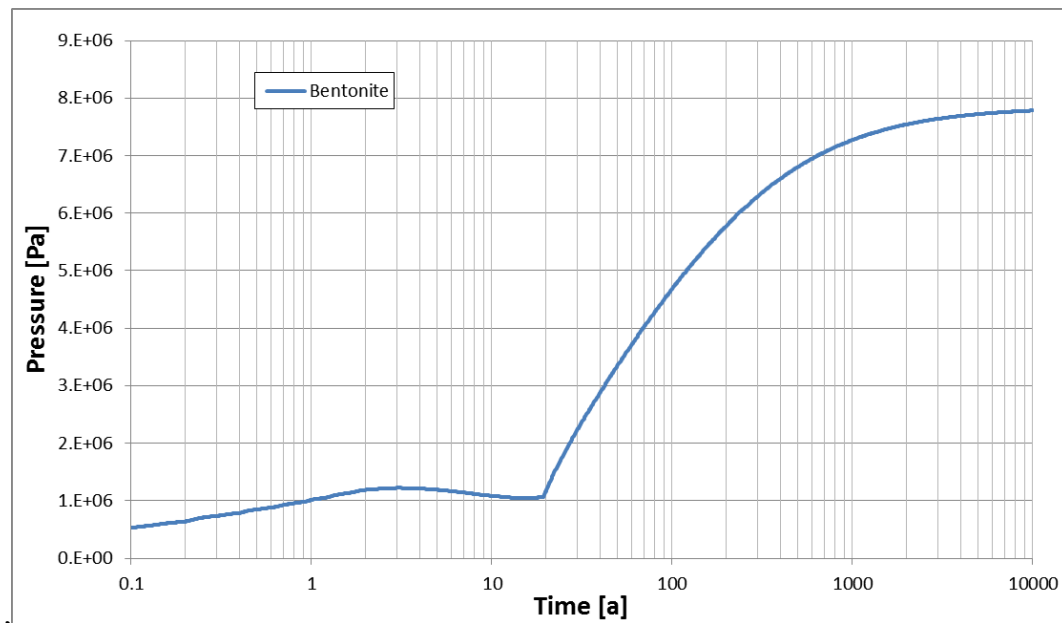


Fig. A3.3: Temporal evolution of pressure in the bentonite during resaturation.

## B-5 Conclusion

The scoping two-phase calculations confirm the assumptions made in the main study:

- Pressure drop after excavation to atmospheric pressure occurs almost immediately in all fractures of the EDZ. Thus, long term recovery simulations can safely start from atmospheric pressure conditions.
- The filling of the bentonite pore space is very fast, only 20 years in the present case, and depends on the initial saturation degree. Compared to the times that pressures needs to fully recover static conditions, a resaturation time of some 20 years is negligible. Thus, long term recovery simulations can safely start from fully saturated conditions in the whole domain.